学位論文

# Study on current distribution in $YBa_2Cu_3O_{7-x}$ superconducting wire for NMR magnet design

（NMR 用マグネット設計の指針となるイットリウム系超電導線材内の電流分布に関する研究）

宮副　照久

# Preface

$YBa_2Cu_3O_{7-x}$ superconducting wires, which are called coated conductors, have high superconducting critical current density ($J_c$) under high field and high tolerance against high mechanical stress. The properties enable coated conductors to be a promising candidate of a construction material of high-field superconducting magnets. On the other hand, coated conductors with high aspect ratios are magnetized by magnetic flux penetrating perpendicularly to the tape surface. Then screening currents flow in the coated conductors. The screening current influences magnetic field generated by a magnet consisting of coated conductors in three following ways: reduction of magnetic flux density at center position, spatial homogeneity of magnetic field and temporal stability of magnetic field. The influence should be taken into design of magnets for Nuclear Magnetic Resonance (NMR) spectrometers. This thesis focuses on current distributions consisting of screening and transport currents flowing in coated conductors under magnetic field.

I first measured magnetic field distributions generated by screening and transport currents flowing in a single short coated conductor in liquid helium under external magnetic field. A superconducting magnet applied the magnetic field. Screening-current-induced field (SCF) increases at the external magnetic field from 0 T to a penetration field, where magnetic flux penetrates over the width of the coated conductor. Over the penetration field, the SCF decreases according to magnetic field dependence of $J_c$. The magnetic field distributions give current distributions of screening and transport currents via inverse problems. The measurement using a single coated conductor reveals that a ratio of a transport current relative to superconducting critical current determines a current distribution in a short coated conductor under external magnetic field higher than penetration field.

As numbers of superimposed coated conductors increase, intensities of SCF increase. Numbers of rows in which coated conductors were arranged varies distributions of SCF. Based on the current distributions of a single coated conductor, I estimated the magnetic field distributions by screening and transport currents flowing in multiple short coated conductors and then compared them with the experimental results. In addition, temporal variations of SCF for the multiple coated conductors were observed at a few kinds of temperatures. The variations were proportional to the logarithm of time.

Based on the current distributions in a single coated conductor under magnetic field, magnetic field distributions generated by pancake YBCO coils were estimated. Then, methods for reducing the SCF were suggested

Chapter 1 describes the background and purpose of this thesis. Experimental equipments used in the following measurements are illustrated in chapter 2. Chapter 3 uses a current-flowing model to discuss a method for estimating the current distribution from magnetic field distribution. Chapter 4 provides distributions of current density, which are solved using the model in chapter 3 in a single CC in which a transport current and an external

magnetic field are applied. Chapter 5 expands the current distribution solved in Chapter 4 to magnetic field distribution induced by multiple CCs. Chapter 6 discusses temporal variations of a magnetic field induced by screening currents in CCs and then moves on to temporal variations of the screening currents. Chapter 7 deals with magnetic field distribution generated by coils, by taking into consideration Chapter 5 and Chapter 6. Chapter 8 lists methods for calculating the magnetic field generated by a YBCO pancake coil and the operating conditions of this coil.

# Acknowledgements

This work was carried out between October 2008 and September 2011 at Ohsaki laboratory, Department of Advanced Energy, Graduate School of Frontier Sciences, the University of Tokyo and partially at Tsukuba Magnet Laboratory, National Institute for Materials Science (NIMS). I spent very exciting and fruitful time in both laboratories.

I would first like to thank my supervisor, **Prof. Hiroyuki Ohsaki**. Thanks to his support, encouragement, and guidance, I learned a lot of things which are not limited to research topics.

I would like to thank,

**Prof. Tsukasa Kiyoshi**, (Group Leader, Magnet Development Group, Superconducting Wires Unit, NIMS);

for giving me an opportunity to make measurements under ultra-high magnetic field, many advices and discussions from broad view points.

**Assoc. Prof. Masaki Sekino**;

for having the time to discuss many research topics as well as this work and making life in Ohsaki lob. more exciting and interesting.

**Prof. Yuuichi Ogawa, Prof. Yasushi Ono, Assoc. Prof. Kazuyuki Demachi,** and **Assoc. Junpei Baba**;

for many scientific suggestions and discussions for this thesis.

**Prof. Hitoshi Wada**;

for leading to very interesting topics, studies of constructing superconducting magnets, and giving me a global view which is not limited to research.

**Mr. Dongmin Kim, Mr. Yutaka Terao, Mr. Loic Queval,** and **Mr. Quddes Mohammad Rashidul**;

for discussing a lot of scientific, economical and social topics in depth. The discussions at the international level gave me global views about various issues.

**All my colleagues in Ohsaki laboratories**;

for enjoyable research life.

**My family, father, mother, brother** and **sister**;

for many encouragements, supports and, their continuous love.

Dearest **my wife, Fumiko, and my son, Youji**;

for invaluable help, great encouragement, and everything.

September 2011

# Table of Contents

# List of Figures

**Chapter 1 Introduction**

**Chapter 2 Experimental Setups**



**Chapter 3 Determination of Method for Estimating Current Distribution**

**Chapter 5 Magnetic Field Distribution Generated by Multiple Coated Conductors**

**Chapter 6 Temporal Variations of Magnetic Field Generated by Screening Current**



**Chapter 7 Magnetic Field Distribution Generated by YBCO Pancake Coil**

**Appendix**

# List of Tables

# Chapter 1

# Introduction

This is the introductory chapter to this thesis, describing the advantages and challenges of $YBa_2Cu_3BaO_{7-x}$ magnets from the view points of materials and applications.

## 1.1 Superconductors for Magnets

Thus far, researchers have discovered numerous superconductors. However, only a few types of superconductors can be used as materials in superconducting magnets. Therefore, this thesis focuses on superconductors for magnets.

### 1.1.1 Discovery of superconductors for magnets

The discovery of superconductivity by Kammerlingh Onnes in 1911 paved the way for high-field applications. He succeeded in liquefying helium and discovered that the resistance of pure mercury abruptly drops to zero below 4.15 K [1]. This temperature is called the critical temperature ($T_c$). In 1933, Meissner and Ochsenfeld discovered the absence of magnetic flux within a superconductor [2]. Superconductors have two additional critical points besides the critical temperature $T_c$, critical magnetic field $H_c$ and critical current density $J_c$. Figure 1-1 shows the critical surface of a typical superconductor. Since Kammerlingh Onnes' discovery of superconductivity, many superconductors have been discovered. However, it has been difficult to transform the superconductors discovered in the last few decades into superconducting magnets because of their low $H_c$ values. Type-II superconductors, first discovered in 1930 [3], enable researchers to create superconducting magnets. There are two kinds of superconductors with different characteristics: Type- I" superconductors have no magnetic flux. However, Type-II superconductors have a quantizing magnetic flux in more than a magnetic field, which is called the lower critical magnetic field ($H_{c1}$). Type-II superconductors are transformed into normal conductors below an upper critical magnetic field ($H_{c2}$). All the superconductors for magnets are Type-II superconductors.

Many superconducting alloys and compounds, especially those which concentrate on A15 compounds such as $Nb_3Sn$, $Nb_3Al$, and $Nb_3Ge$, were discovered between 1954 and 1986 [4], and many high temperature superconductors have been explored with a discovery of a high-$T_c$ cuprate superconductor by J. G. Bednorz and K. A. Müller in 1986 [5]. In 1987, Chu *et al.* discovered that $YBa_2Cu_3O_{7-x}$ (YBCO) becomes a superconductor below 93 K [6]. Akimitsu *et al.* reported that $MgB_2$ has a $T_c$ of 39 K [7], which was the highest temperature attained in intermetallic superconductors. In addition, explorations of new material systems by Hosono *et al*. in 2006 have led to the discovery of an iron-based superconductor [8].

### 1.1.2 Practical and promising superconducting wires

Table 1-1 lists the critical temperatures and upper critical magnetic fields of both practical and promising superconductors [9]. $MgB_2$ and high-temperature superconductor (HTS) have anisotropic superconducting properties. Kilometer-class superconducting wires are required to make superconducting magnets. Almost all practical superconducting magnets are made from only two superconducting wires, Nb-Ti and $Nb_3Sn$ wires. Superconducting wires should be electrically and thermally stable, and so, the superconductors are generally embedded in a normal conducting matrix. To attain this stability, the superconducting wires have to be multifilamentary ones with diameters less than about 50 μm that then need to be twisted. Figure 1-2 shows a typical cross-section of a bronze-processed $Nb_3Sn$ superconducting wire externally stabilized by a 3.50 × 1.75-mm copper matrix [10]. There are wiring processes suitable for each superconductor. Accordingly, magnet-grade superconductors have high $T_c$, $H_{c2}$, $J_c$ and specialized wiring processes.

Figure 1-3 shows critical engineering current densities ($J_e$) of short superconducting wires as functions of applied magnetic fields at 4.2 K, which is the boiling temperature of liquid helium [11]. $J_e$ is obtained by dividing the critical current ($I_c$) by the overall cross-section of the superconducting wire. YBCO and Bi-2223 wires have tape-like shapes. A magnetic field is applied both perpendicular and parallel to the tape surfaces. Under a magnetic field parallel to the tape surface, $J_e$ is higher than when a magnetic field is perpendicular to the tape surface. Superconducting magnets generating a magnetic field over 25 T cannot be constructed using only Nb-Ti and $Nb_3Sn$ superconducting wires because of their $H_{c2}$ values. Conventional superconducting magnets have difficulty operating at temperatures above 4.2 K. In order to construct magnets generating magnetic fields over 25 T and/or operating over 4.2 K, HTS magnets should be developed.

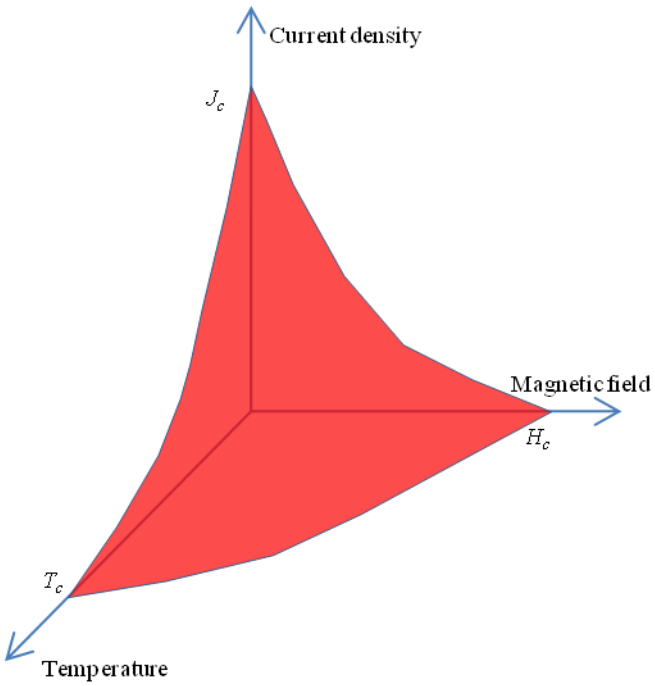


*Figure 1-1: Critical surface of superconductors*

*Table 1-1: Critical temperatures and upper critical magnetic fields of magnet-grade superconductors* [9]

| Superconductor | $T_c$ (K) | $\mu_0 H_{c2}$ at 0 K (T) |
|---|---|---|
| *Low temperature superconductor (LTS)* | | |
| **Nb-Ti** | 9.3 | 13 |
| **$Nb_3Sn$** | 18 | 23 |
| **$Nb_3Al$** | 18.9 | 32 |
| **$MgB_2$** | 39 | 16 (*a*, *b*)<br>2.5 (*c*) |
| *High temperature superconductor (HTS)* | | |
| **$YBa_2Cu_3O_{7-x}$ (YBCO)** | 93 | 670 (*a*, *b*)<br>120 (*c*) |
| **$Bi_2Sr_2CaCu_2O_{8-x}$ (Bi-2212)** | 90 | 280 (*a*, *b*)<br>32 (*c*) |
| **$(Bi, Pb)_2Sr_2Ca_2Cu_3O_{10+x}$ (Bi-2223)** | 110 | |

*(a, b) and (c) refer to a coplanar magnetic field with the a, b crystallographic direction and an orientation along the c-axis, respectively.*

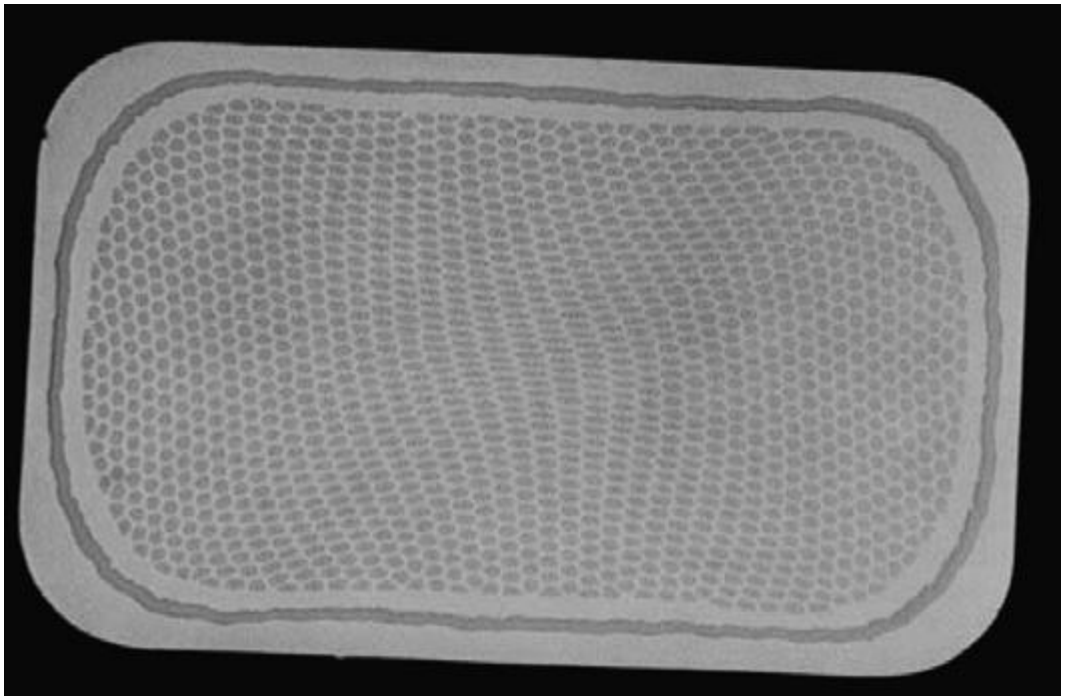

*Figure 1-2: A typical cross-section of a bronze-processed $Nb_3Sn$ superconducting wire externally stabilized by a 3.50 × 1.7- mm copper matrix* [10]

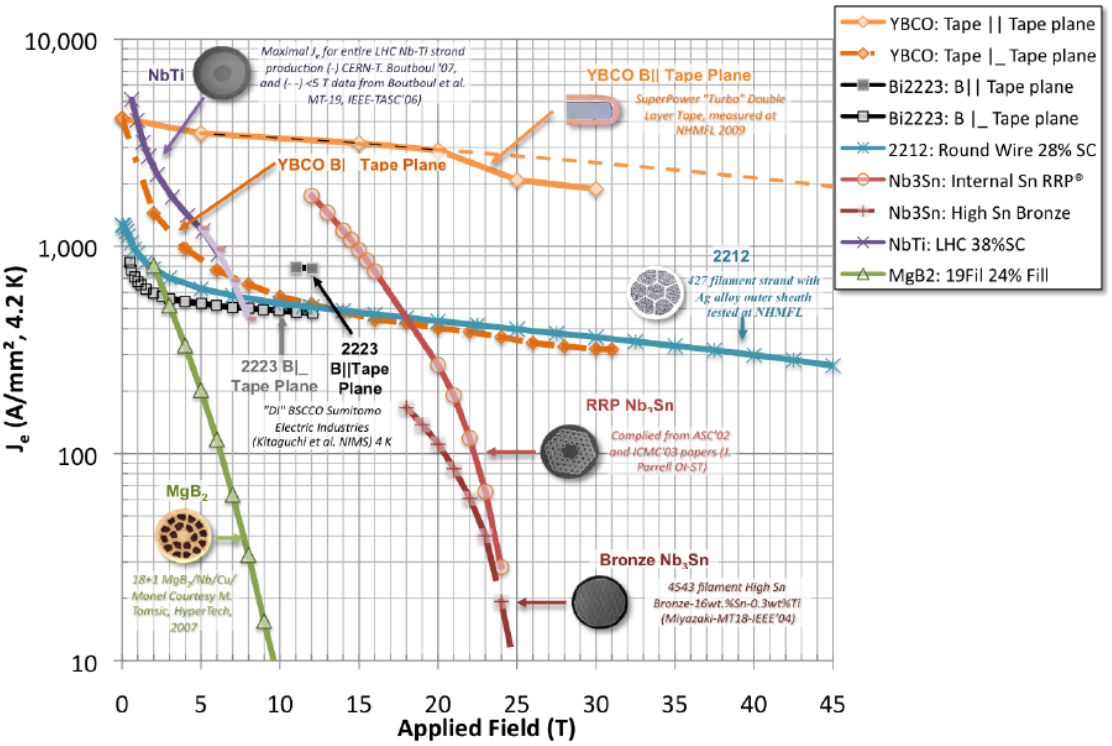


*Figure 1-3: Critical engineering current densities ($J_e$) of superconducting wires as functions of applied magnetic fields at 4.2 K* [11]

Superconducting properties $T_c$, $H_{c2}$, and $J_c$ are also influenced by strains applied to the superconductors. Theories and experimental results pertaining to the strain effects of low-temperature superconductors (LTS) are well summarized by Ekin [9]. A superconducting wire is a combined material. The wire is generally fabricated in atmosphere at several hundred degrees Celsius and is used at very low temperatures. Stresses are applied to superconductors in cryogens by the other composite materials because of differences in thermal contractions. Figure 1-4 shows the $I_c$ of a $Nb_3Sn$ wire as a function of axial strain for different magnetic fields applied perpendicular to the current direction [12]. As the applied strain increases, the critical current first increases, reaches a maximum at a strain of 0.32%, and then decreases. The strain is caused by differences in thermal contractions in an axial direction. The critical current as a function of axial strain is different depending on each magnetic field.

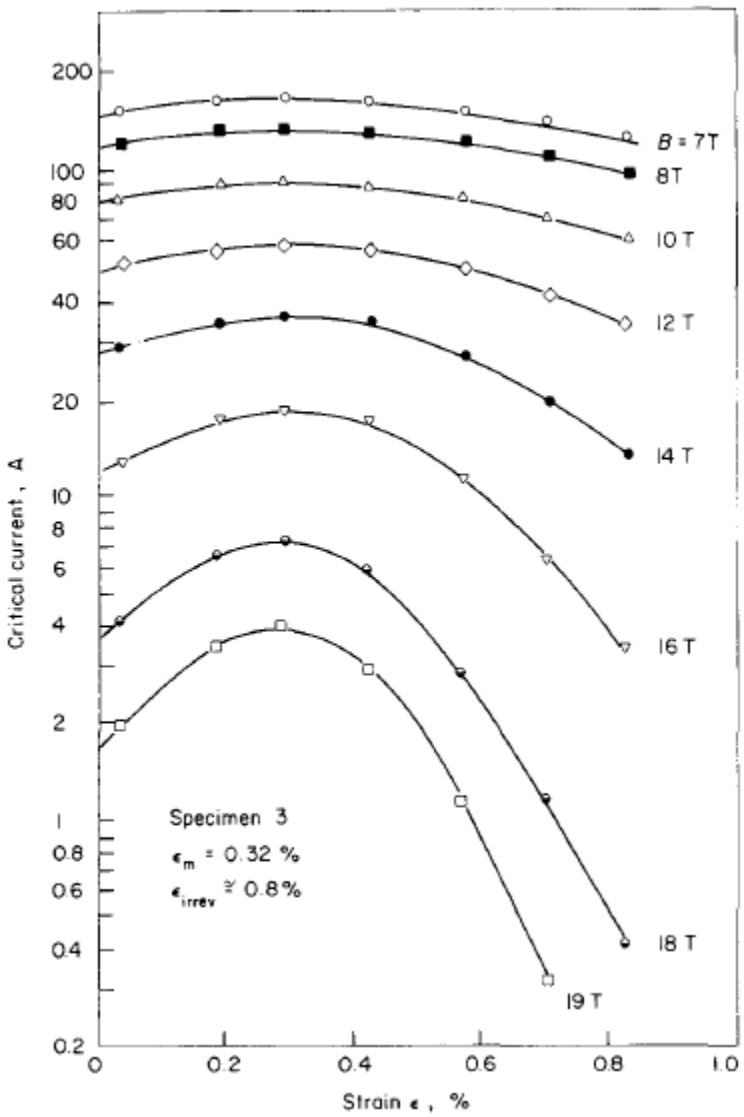


*Figure 1-4: Critical current of a $Nb_3Sn$ wire as a function of axial strain for different magnetic fields applied perpendicular to the current direction* [12]

## 1.2 YBCO Superconducting Wires

Kilometer-class YBCO superconducting wires with high $I_c$ at 77 K have been developed. In particular, the development proceeded at a rapid rate through national projects in Japan [13, 14] and the United States of America. As a result, YBCO superconducting wires are expected to be promising materials for electric power cable [15], fault current limiters [16], superconducting magnetic energy storage systems (SMES) [17], transformers [18], motors [19], generators [20] and magnets.

When designing a YBCO magnet, it is very important to consider the electromagnetic properties of YBCO superconducting wires. High mechanical stress is applied to superconducting wires used in superconducting magnets, and there are three kinds of mechanical stresses: hoop stress, bending stress, and stress caused by differences in the thermal contraction between composite materials as they cool down.

### 1.2.1 Developments of kilometer-class YBCO superconducting wires

Developments of $REBa_2Cu_3O_{7-x}$ (REBCO: rare earth barium cuprate), such as YBCO superconducting wires enable the production of wires in long lengths with high $J_c$ at 77 K, as well as under high magnetic fields at 4.2 K [21, 22]. SuperPower Inc. developed a kilometer-long YBCO superconducting wire with an $I_c$ over 200 A/cm-width at 77.3 K under self field [21]. Fujikura Ltd. developed a $GdBa_2Cu_3O_{7-x}$ wire with an $I_c$ over 609 A/cm-width at 77.3 K over a length of 615 m with [22]. Figure 1-5 shows the crystalline structure of YBCO. The structure indicates that REBCO has anisotropic superconducting properties. Unlike Bi-2212 and Bi-2223 wires, REBCOs must be biaxially oriented in order to connect electrically between crystal grains [23]. Figure 1-6 shows a typical structure of a REBCO superconducting wire. A thin oxide buffer layer to promote biaxial orientations of REBCO superconductors is deposited on a metal or alloy substrate.Then, REBCO superconductors are deposited on the buffer layer. A silver overlayer prevents the superconducting layer from deteriorating. Because of their fabrication process, REBCO superconducting wires are referred to as “coated conductors (CCs)”. There are a substantial number of processes involved in the fabrication of REBCO superconducting wires. The fabrication process differs from company to company, but REBCO superconducting wires typically have common shapes with a width of several millimeters and a thickness of hundreds of micrometers. The basic processes of fabricating CCs are well summarized by Goyal [24].

In this paper, we present two methods for fabricating long REBCO CCs with high $I_c$ developed by Fujikura Ltd. and SuperPower Inc.. Both methods employ ion-beam assisted deposition (IBAD) for orienting MgO biaxially as buffer layers [22, 25]. The IBAD method was developed by Fujikura Ltd. in Japan [26]. The deposition processes of superconducting layers are different. Fujikura Ltd. has been developing a pulsed-laser-deposition (PLD) as a method for depositing a REBCO superconducting layer [22]. SuperPower Inc. has been developing a metal-organic chemical vapor deposition (MOCVD) method [21, 25], which is a major thin film fabrication technique in the semiconductor-based micro electronics industry [27].

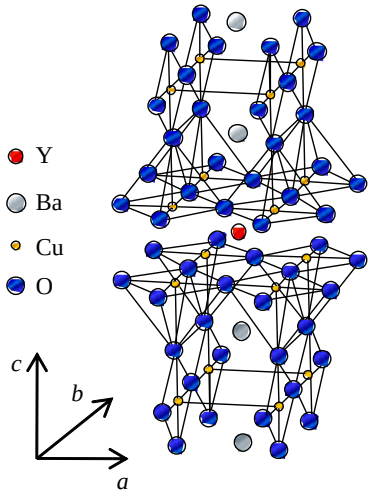


*Figure 1-5: Crystal structure of $YBa_2Cu_3O_{7-x}$*

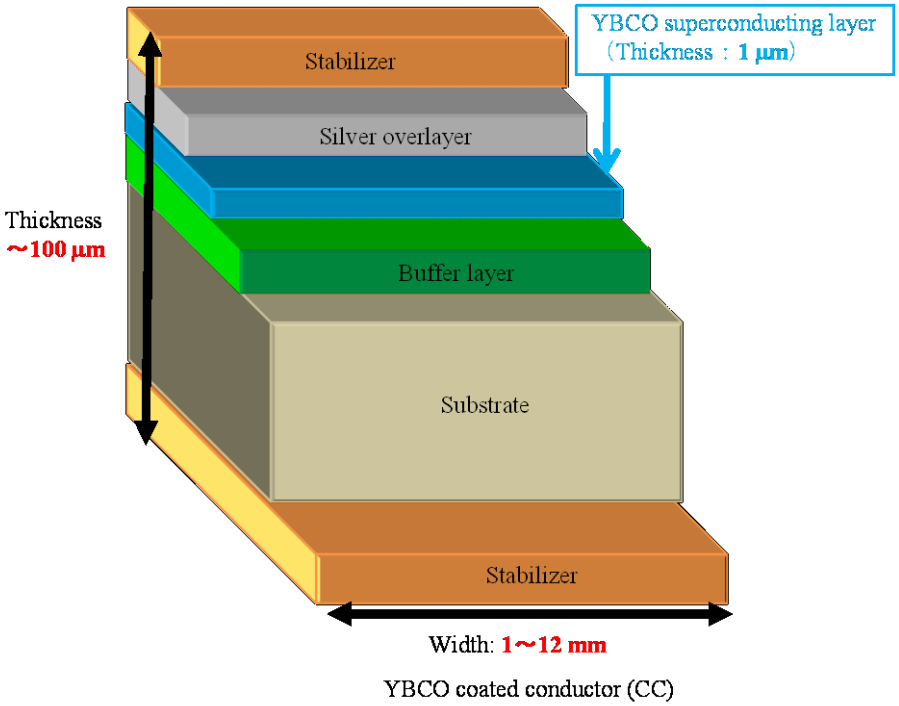


*Figure 1-6: Typical structure of a YBCO coated conductor*

### 1.2.2 Angular dependence of $J_c$ for YBCO coated conductors

Uglietti *et al.* compared differences in sensitivities to the orientation of the magnetic fields applied to both a commercial a Bi-2223 wire and a YBCO CC [28]. Figure 1-7 shows the $I_c$ for each type of wire normalized at a maximum of $I_c$ ($I_{cmax}$) as a function of the angle between the magnetic field and the sample faces of the Bi-2223 wire and the YBCO CC. The differences in sensitivities were measured under a magnetic field with a magnetic flux density of 12 T at 4.2 K. A magnetic field with an angle of zero degree corresponds to the field parallel to the sample surface. Compared to the case in the Bi-2223 wire, in the YBCO CC $I_c$ was more sensitive to the orientation of the magnetic field. Otsuka et al. made the angular dependence of the YBCO CC fit with the following equation [29]:

$$\frac{I_c}{I_{c\max}} = \frac{\theta_0^p}{\theta^q + \theta_0^p}(1-s)+s \qquad (1.2.1)$$

Here, $\theta_0$ is an angle at $I_{cmax}$, $p$, $q$ and $s$ are fitting parameters.

Normal conductors in a superconductor which are called pins, restrain the motion of magnetic flux lines inside the superconductor. Matsushita discusses flux pinning mechanisms and properties and the electromagnetic phenomena in [30]. Artificial pins are effective for reducing the angular dependences of $I_c$. Many studies demonstrate that epitaxial $BaZrO_3$ (BZO) and $BaSnO_3$ nanocolumns parallel to the $c$ axis and the nanoparticles are effective for pinning in REBCO CCs near 77 K [31-33]. Since the $J_e$ performance of REBCO CCs is not adequate for high-field magnet applications, the CCs are needed to cool the superconductors to lower temperatures. Xu *et al.* reported that angular dependences of the $I_c$ of REBCO CCs with BZO nanocolums parallel to the $c$ axis at 4.2 K were different from those near 77 K [34, 35]. In contrast with 77 K, at 4.2 K the BZO nanocolumns do not produce any enhancement of $I_c(\theta)$ near angles where magnetic fields are applied parallel to the $c$ axis. However, they are effective for enhancing $I_c$ values under high magnetic fields parallel to the *ab*-plane of the CC, even at 4.2 K.

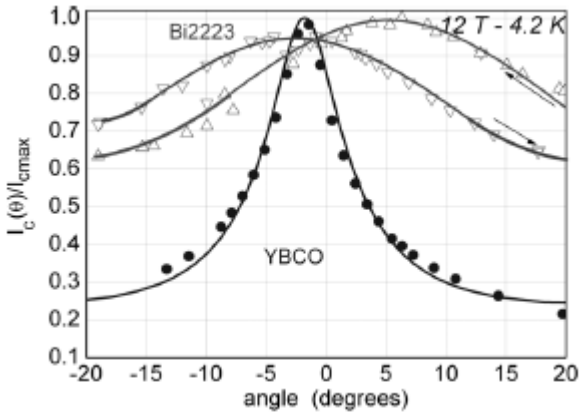


*Figure 1-7: $I_c$ normalized at $I_{cmax}$ as a function of the angle between the magnetic field and the sample faces of the Bi-2223 wire and the YBCO CC* [28].

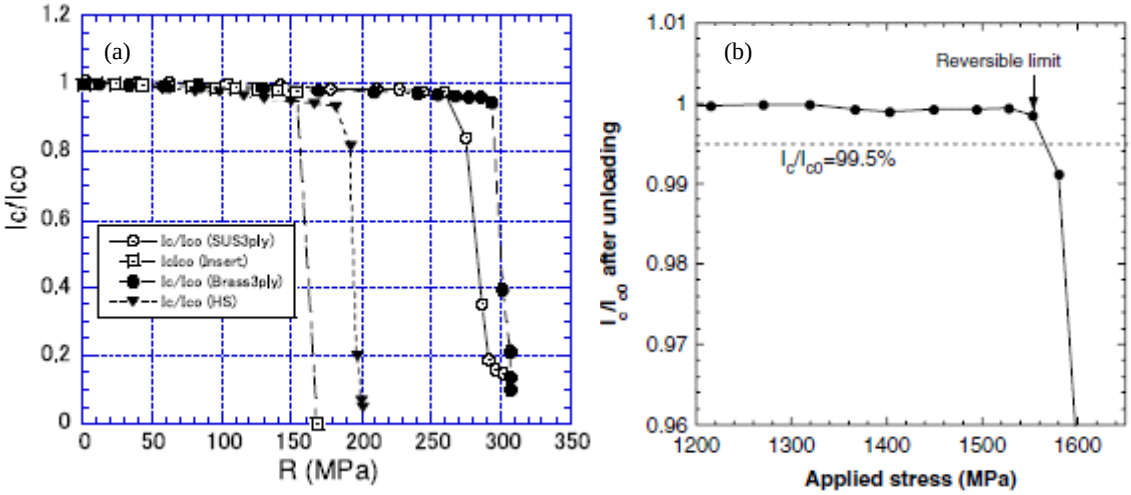


*Figure 1-8: Degradations of $I_c$ by stress applied to (a)Bi-2223 wires* [38] *and (b) YBCO CC* [40]

### 1.2.3 Mechanical strength of YBCO coated conductors

The mechanical strength of REBCO CCs is much higher than that of Bi-2212 and Bi-2223 wires [36-40] due to the substrates used with the REBCO CCs [37]. Both Fujikura Ltd. and SuperPower employed Hastelloy C-276 as the substrate materials [22, 25]. On the other hand, commercial Bi-2223 wires are strengthened by laminations of stainless steel tapes. Figure 1-9 shows strain dependences of $I_c$ normalized by $I_c$ at zero stress for Bi-2223 wires [38] and a YBCO CC [40]. Osamura *et al.* compared the strain dependences of Bi-2223 wires strengthened by laminations of brass or stainless tapes with those without the laminations [38]. Damage-tolerant of the reinforced Bi-2223 wire is below 300 MPa. The tolerant strength of the CC is over 1000 MPa [40]. High stress applies to superconducting wires in high-field and compact magnets. In terms of mechanical tolerance, a YBCO CC is desirable as a material for use in high-field and compact magnets.

## 1.3 High-field NMR Magnet

A phenomenon of nuclear magnetic resonance (NMR) was first measured by Rabi *et al.* [41]. Today, an NMR spectrometer has become a powerful device for analyses of molecular structures and biochemistry. Superconducting magnets generate higher magnetic fields than conventional magnets, and are therefore required for use in NMR spectrometers and magnetic resonance imaging (MRI) devices so as to produce better resolution.

### 1.3.1 Brief principle of NMR

Details of NMR theory are discussed elsewhere [42]. Here, we only describe the brief principles of NMR required to develop superconducting magnets. Figure 1-9 is a schematic of how an NMR spectrometer works. Atomic nuclei have a magnetic dipole moment proportional to the angular momentum. The proportional constant is known as the gyromagnetic ratio, $\gamma$. The presence of a direct current (DC) magnetic field with a magnetic flux density of $B$ splits the energy levels of nuclear spins. The difference in energy levels is $\Delta E$:

$$\Delta E = \gamma \hbar B \tag{1.3.1}$$

where $\hbar = h/2\pi$ and $h$ is the Planck constant. A radio frequency pulse with an energy of $\Delta E$ perpendicular to the DC field causes nuclear spins in all the states to precess. The resonant frequency is called the Larmor frequency, $\omega_0$, and it is given by

$$\omega_0 = \gamma B \tag{1.3.2}$$

Absorption and relaxation of the energy of the nuclear spins at the resonant frequency are detected as NMR signals.

The gyromagnetic ratio of protons is $\gamma = 2.675 \times 10^8 \mathrm{rad/s \cdot T}$. Generally, the magnetic field intensity of a NMR magnet is expressed as the resonant frequency of protons. A frequency of 42.5759 MHz corresponds to a magnetic flux density of 1 T.

### 1.3.2 NMR magnet

High-resolution NMR magnets are required in order to generate magnetic fields within spatial variation of 100 Hz (2.35 μT) and temporal variations of 10 Hz/h (0.235 μT/h) inside a columnar sample space with a diameter of 10 mm and a height of 20 mm [43]. A typical view of an NMR magnet is illustrated in Figure 1-10. The NMR magnet consists of main superconducting coils, correction superconducting coils, and shim superconducting and normal conducting coils. This thesis focuses on main superconducting coils.

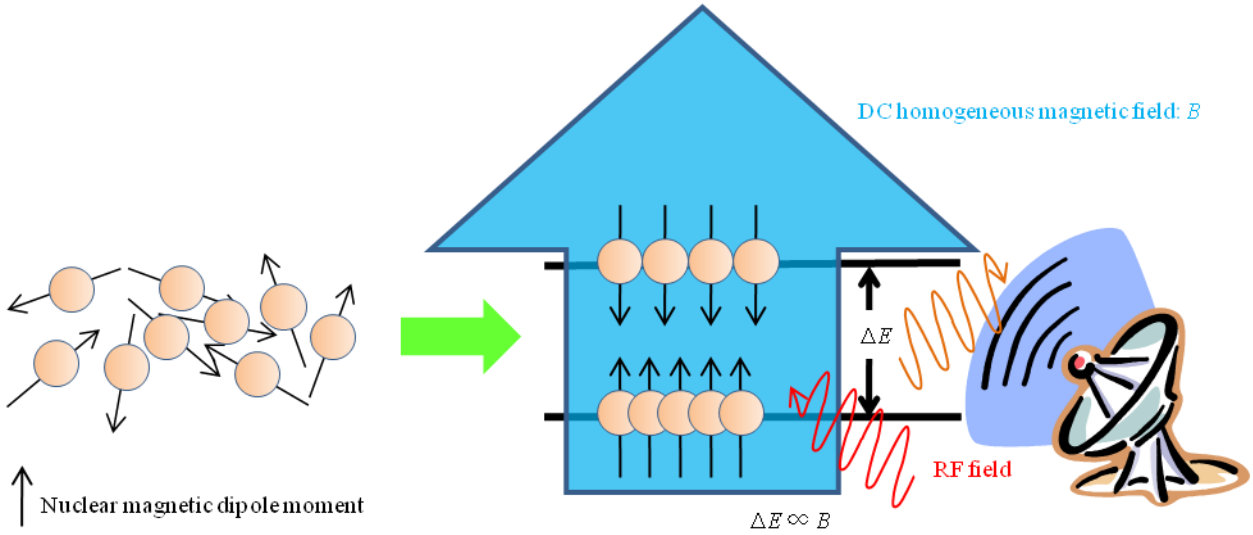


*Figure 1-9: A schematic of how an NMR spectrometer works.*

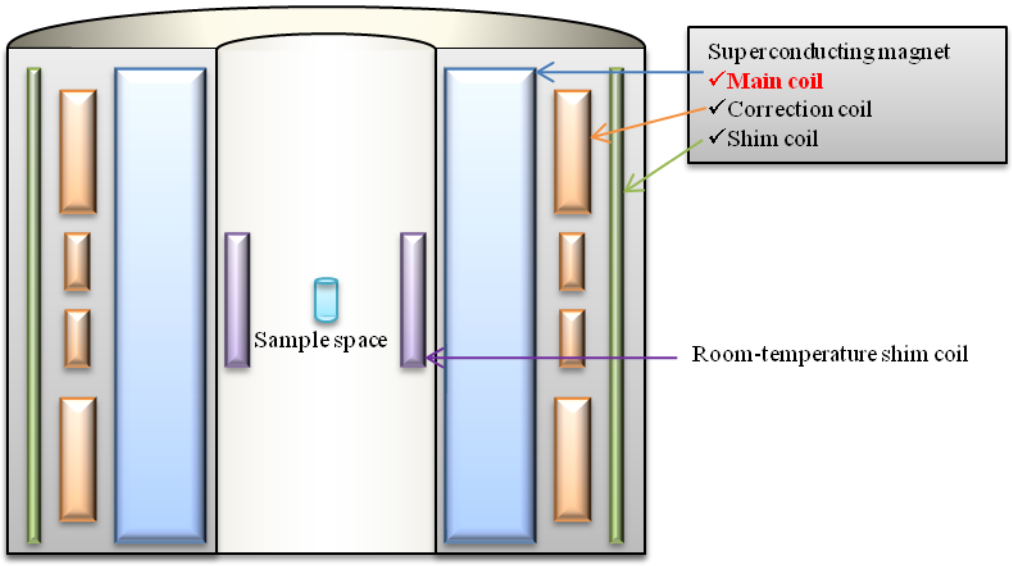


*Figure 1-10: A schematic of an NMR magnet.*

### 1.3.3 Development of high-field LTS NMR magnet

The increase in magnetic field that a NMR magnet generates results in the enhancement of nuclide identification and the reduction in measurement duration. LTS NMR magnets operate in a persistent current mode to realize high stability of the magnetic field.

Since the turn of this century, developments in high-field LTS NMR magnets have targeted 1 GHz (23.5 T) NMR. In 2001 and 2004, Tsukuba Magnet Laboratory (TML) at the National Institute for Materials Science (NIMS) developed a 920 MHz and 930 MHz NMR, respectively [44, 45]. High-field LTS NMR magnets were constructed from NbTi coils and $Nb_3Sn$ coils incorporated in the NbTi coils [46]. Wires for NMR magnets were also developed [47]. Figure 1-11 provides an overview of and the superconducting coils used in the 920 MHz NMR developed at TML. The 920 Mhz NMR magnet generated a magnetic field with homogeneity of 0.1 ppm and stability of 1.3 Hz/h. In 2009, Brucker BioSpin announced the launch of the 1 GHz LTS NMR magnet [48].

Hitachi Ltd. created an innovative 600 MHz NMR magnet in 2008 [49]. They developed a superconducting split magnet and a cross-shaped bore in order to apply a solenoidal antenna coil with higher sensitivity to the NMR system.

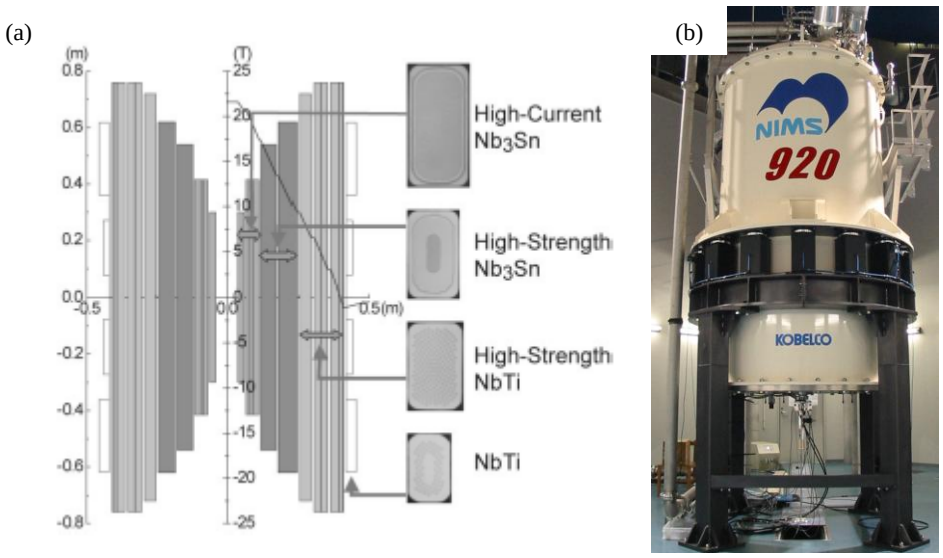


*Figure 1-11: Superconducting coils and an overview of a 920 MHz NMR developed at TML* [46]

### 1.3.4 Development of LTS/HTS NMR magnet

National High Field Magnet Laboratory (NHMFL), Francis Bitter Magnet Laboratory (FBML) at the Massachusetts Institute of Technology and TML, in collaboration with Rikagaku Kenkyujo (RIKEN) are developing above 1 GHz NMR magnets. NHMFL developed a 900 MHz NMR magnet with a wide room-temperature bore of 89 mm in 2000 [50, 51] using LTS coils, they are currently upgrading this magnet to a 1.3 GHz (30 T) NMR magnet using an HTS coil [52]. FBML started a 3-phase program for a 1.3 GHz NMR in 2000. The third phase of the program started in 2008. They consider that the 1.3 GHz NMR magnet will be realized by a combination of a 700 MHz LTS magnet and a 600 MHz HTS magnet. In the first stage of the third phase, they wound and tested Bi-2223 coils and YBCO coils as candidates for the 600 MHz NMR magnet [53]. TML started developing an HTS-NMR magnet system in 2006 [54]. A 1.03 GHz (24.2 T) NMR magnet system is being constructed by replacing the innermost $Nb_3Sn$ coil of the 920 MHz NMR magnet with a Bi-2223 coil at TML. The outer LTS coils generate 20.6 T and the Bi-2223 coil adds a field of 3.6 T. The critical current and mechanical issues for the Bi-2223 coil are discussed in [55]. In contrast with the 920 MHz NMR magnet operation, the 1.03 GHz NMR magnet operates in a driven mode using a highly stabilized power supply. In addition, a 1.3 GHz NMR magnet design using only YBCO superconducting coils is being considered in terms of mechanical hoop stress and critical current in [29].The design study for the 1.3 GHz NMR revealed that the NMR magnet that used only YBCO coils would be more compact than the 920 MHz NMR magnet.

## 1.4 YBCO NMR Magnet Technology Issues

Several reference books [56, 57] have provided detailed information on magnet technology issues in the design of typical superconducting magnets. When designing a superconducting magnet, it is necessary to give due consideration to operating temperature, operating current ($I_o$), mechanical stress, and generation magnetic field. Figure 1-12 shows a design concept of a superconducting magnet. This paper mainly presents the following issues when developing YBCO magnets:

- Operating current depending on stress, temperature and intensities and angles of magnetic field.
  $J_c$ of the YBCO CC depends on stress, and intensity and direction of magnetic fields as shown in Figure 1-3, Figure 1-7, and Figure 1-8. Otsuka *et al.* described the feasibility of a 1.3 GHz NMR magnet using only YBCO coils under the conditions of the highest hoop stress of 500 MPa [29]. The $I_o$ relative to $I_c$ reached maximum values near the top edges of the YBCO coils because of the angular dependences of $J_c$ of YBCO CCs.
- Joint between YBCO CCs
  Superconducting magnets requires a superconducting wire with a length of several kilometers. However, the YBCO CCs available are at most about 1 km [21]. It is necessary to develop techniques by which to join CCs in order to expand YBCO application devices. It is important to reduce joint resistance. Several studies have suggested joint techniques and compared the corresponding joint resistances. Here, two kinds of these joint techniques are mentioned as examples [58, 59]. In one technique, a lap joint is soldered between copper stabilizers of CCs [58]. Figure 1-13 shows the lap joint [60]. The shear stress tolerance of the lap joint was measured in [61]. Sugano *et al.* concluded that the interface between the YBCO layer and the buffer layer in a CC is weak against the shear stress. TML has also tested a YBCO coil with a joint [61]. The other

technique involves a diffusion joint of silver overlayers of CCs. The joint resistance for the diffusion joint is lower than that for the lap joint. The difference of the resistances is about 20 $n\Omega/cm^2$.

- Quench protection

  Quench is a phenomenon in which part of a superconducting magnet transitions to a normal conducting state, generates heat, and then all the parts of the superconducting magnet transitions to normal. Copper stabilizers attaching to CCs prevent quench in YBCO coils from occurring. Naitou *et al.* revealed that thermal conductivity along the length of YBCO CCs were determined by the amount of stabilizer [62]. On the other hand, Nakamura et al. reported that thermal diffusivity along the thickness of CCs was less than that of the composed materials [63]. These results indicate that a sudden transition to a normal conducting state inside a YBCO superconducting coil is easier to expand in the circumferential direction than in the radial direction of the coil. FBML studied protection of the YBCO coil used in the 600 MHz HTS insert and concluded that commercial CCs do not have adequate stabilizers for the magnet under operating conditions [53]. As a result, in the winding process of a YBCO coil, an additional stabilizer material is wound with a YBCO CC.

- Winding process

  The coil shape for NMR magnets should be determined by taking into consideration the design concept. Typical coils shapes for tape conductors are drawn in Figure 1-15. The left-hand side and right-hand side shapes are called a layer-wound coil and a double-pancake coil, respectively. Markiewica *et al.* analyzed winding strains of the layer-wound and the double-pancake coils, including joints of YBCO CCs [64].

  Superconducting coils are impregnated with epoxy resin to prevent them from moving. However, Takematsu *et al.* reported that impregnation with conventional epoxy resin peeled the YBCO superconducting layer from the buffer layer and degraded the superconducting properties of the YBCO coils [65]. Therefore, TOSHIBA developed a new resin for the impregnation of YBCO coils [66].

- Screening current

  Experiments and calculations [67-71] have indicated that HTS coils generate inhomogeneous and unstable fields due to the screening currents ($I_s$) flowing in the HTS wires, Bi-2223 wires and YBCO CCs having tape shape. The magnetic flux component perpendicular to the tape surface induces $I_s$, as shown in Figure 1-14. The intensity of the screening current density corresponds to that of the critical current density. $I_s$ decays proportionally to the logarithm of time due to flux creep [72], which is described in the section of 1.5.4.

  Hahn *et al.* reported that the screening current reduced the intensity of the magnetic field at the magnet center and affected the homogeneity and stability of the magnetic field in the 350 and 700 MHz NMR magnet test, in which Bi-2223 coils were used [67]. The method used to energize the 700 MHz magnet improved magnetic field homogeneity in the columnar spaces -lengths, 17 mm; diameter, 30 mm- from 633 ppm in the 350 MHz magnet to 172 ppm in the 700 MHz magnet. Yanagisawa *et al.* achieved a reduction in the temporal drift of the magnetic field due to flux creep in the Bi-2223 tape [69]. A current sweep reversal was the method used for the reduction, as follows: an electric current as small as 1% of the operating current is applied once and then the current decreases to the operating current.

  In contrast with conventional superconducting multifilamentary wires and tapes, the superconducting layer in a YBCO CC is mono-conductor. Uglietti *et al.* reported that the screening currents affect the magnetic field generated by a small-size YBCO coil as well [70, 71]. Figure 1-16 shows the magnetic flux density at

the center of the YBCO coil during charge and discharge [70]. The hysteresis is the results of the screening currents flowing in the YBCO CC.

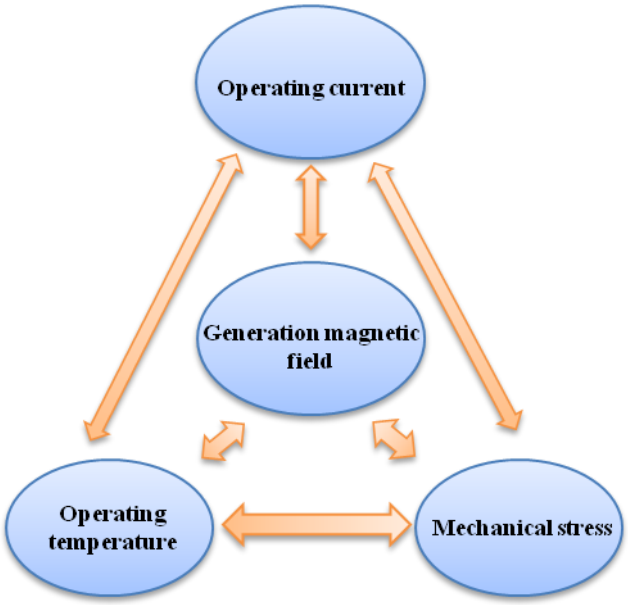


*Figure 1-12: Design concept of a superconducting magnet*

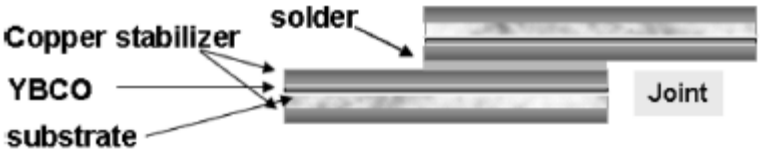


*Figure 1-13: A schematic view of a lap joint between CCs* [60]

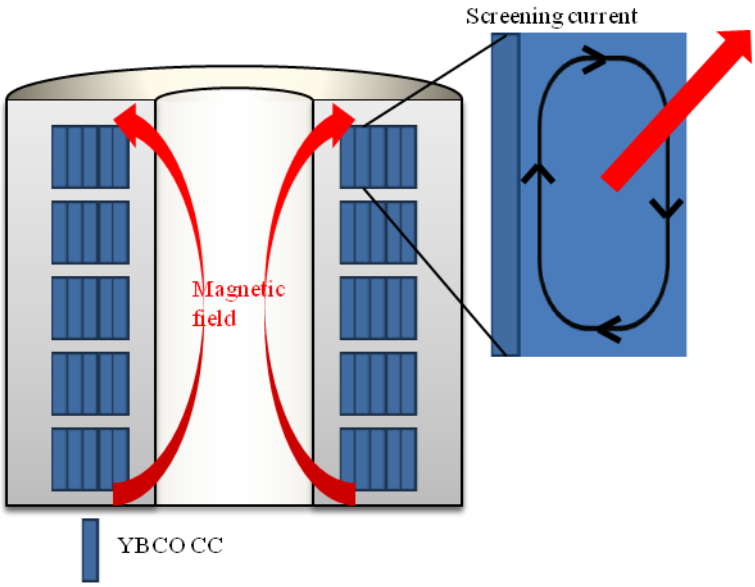


*Figure 1-14: Schematic diagram of screening current flowing in a YBCO CC used in a magnet*

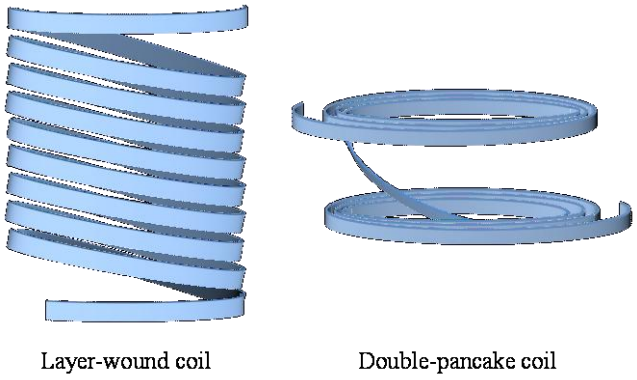


*Figure 1-15: Shapes to be considered for YBCO coils*

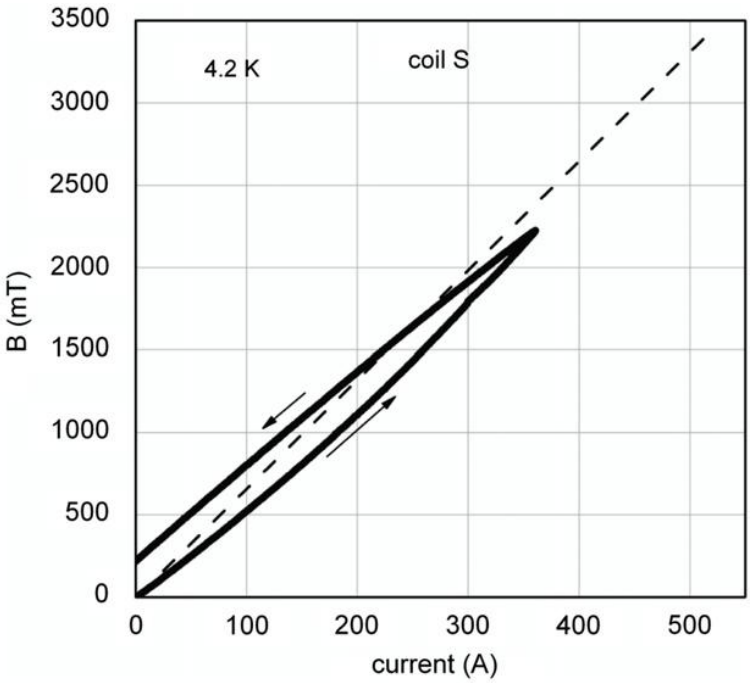


*Figure 1-16: Magnetic flux density at the center of the YBCO coil during charge and discharge* [70]

## 1.5 Current Distribution in a YBCO CC

As stated above, the screening currents flowing in the CCs affect the quality of the magnetic field generated by the YBCO coils. In order to decide on a precise electromagnetic design and accurate operating conditions of a YBCO magnet, it is very important to understand how the total currents flow, which consist of the screening and transport current. There are several nondestructive methods for evaluating current distribution in thin superconducting films, such as determining the magnetic field distribution [73-75], the magnetic-knife method [76, 77], and teraherz radiation mapping [78]. This thesis focuses on determining the magnetic field distribution using simple equipment for making measurements.

### 1.5.1 Method for measuring magnet field distribution

Magnetic field distribution is one of the factors used to determine current distribution in superconducting thin films. The following nondestructive methods for evaluating a current distribution in a YBCO CC through the measurement of the magnetic field distribution have been suggested: scanning Hall probe [73], scanning superconducting quantum interference device (SQUID) microscope [74], and magneto-optical (MO) imaging method [75]. The features of the various techniques for measuring magnetic field distribution are stated below.

- Scanning Hall probe

  The scanning Hall probe method is intended for measuring magnetic field distribution using a Hall sensor; it is more effective in a high-field and low-temperature environment than other methods. In addition, the equipment is easier to prepare. Therefore, the method is suitable to evaluate the total currents flowing in CCs under a magnetic field. The Hall effect, discovered by Edwin H. Hall in 1979 [79], is a phenomena in which a transverse voltage ($V_H$) appears in a conductor with an electric current under magnetic field perpendicular to the current, as shown in Figure 1-17. $V_H$ is given by:

  $$V_H = \frac{R_H I B_z}{d} \tag{1.5.1}$$

  where $R_H$, $I$, $B_z$, and $d$ are the Hall coefficient, current, component perpendicular to the current of magnetic flux density and thickness of the conductor, respectively. $R_H$ depends on the material of the conductor. The spatial resolution depends on the size of the active area of the Hall sensor.

  The scanning Hall probe method is used to evaluate $J_c$ distribution in the development of superconducting wires. THEVA developed a reel-to-reel system for measuring $I_c$ distribution along the lengths of CCs in liquid nitrogen at a speed of 10 mm/s [80]. Figure 1-18 shows a critical current distribution of a one-meter long CC. Higashikawa *et al.* studied a sped-up technique of the scanning Hall probe system for long CCs [81].

- Scanning SQUID microscope

  SQUID is a magnetometer with the highest resolution that can detect a magnetic flux density as low as $10^{-15}$ T. Josephson junction, suggested by Brian David Josephson in 1962 [82] is used in the SQUID system. Figure 1-19 shows a typical view of the SQUID system. Koyanagi *et al.* developed a scanning SQUID microscope that allowed measurements of magnetic flux density at positions 4 μm apart. Using SQUID, they were able to measure local current flow around artificial defects in YBCO films [83]. Nb-based superconductors are used in the low-$T_c$ SQUID system as a SQUID ring and the pickup coil. The low-$T_c$ SQUID system cannot be used in a high-field magnet due to the $H_{c2}$ of the superconductors.

- Magneto-optical imaging

  The Faraday effect, discovered by Michael Faraday in 1845, is used in MO imaging systems. Figure 1-20 shows a rotation of the plane of polarization due to the Faraday effect. The polarization vector of a linearly polarized light beam propagating over length $d$ parallel to magnetic field $H$ is rotated through angle $\beta$ in specific materials. $\beta$ is given by

  $$\beta = V(\omega, T) dH \tag{1.5.2}$$

  where $V(\omega, T)$ is a material-specific and temperature- and frequency-dependent constant, the so-called Verdet constant.

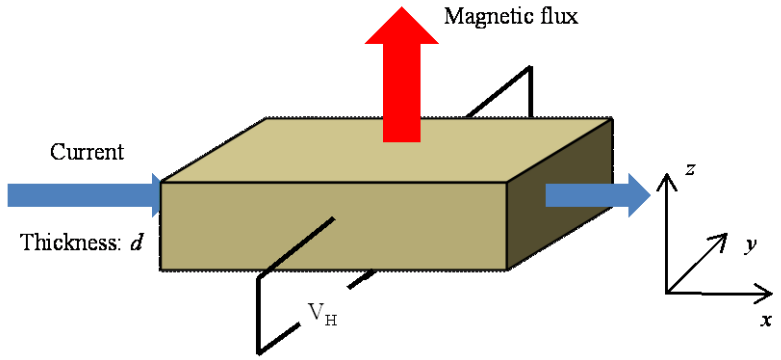


*Figure 1-17: A schematic view of the Hall effect*

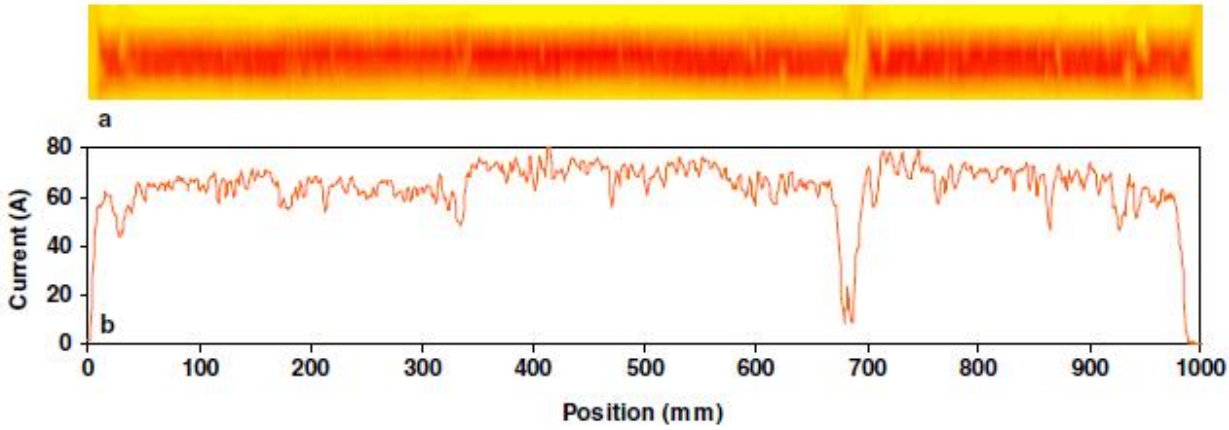


*Figure 1-18: Critical current distribution of a 1 m -long CC* [77]

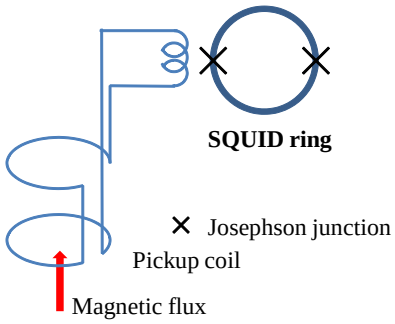


*Figure 1-19: A typical view of the SQUID system consisting of a SQUID ring and pickup coil*

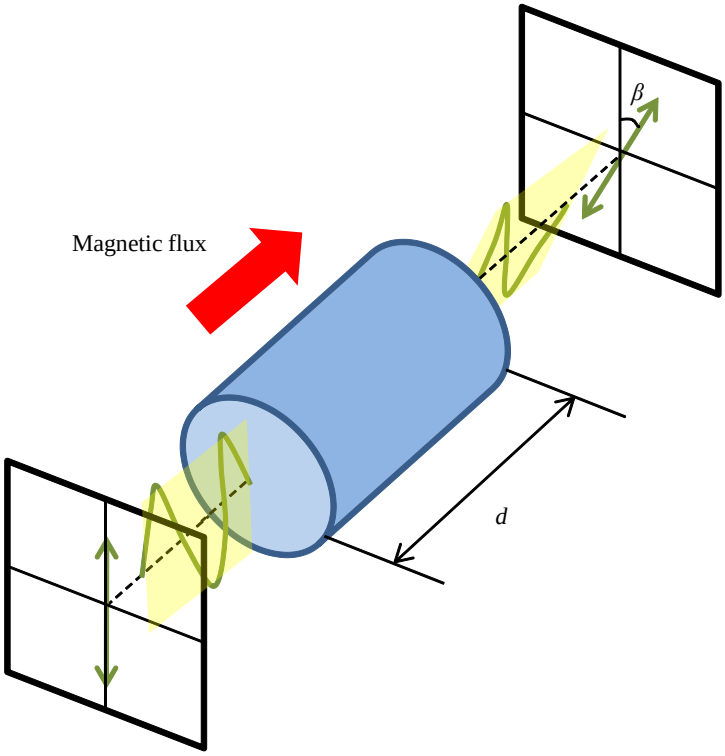


*Figure 1-20: Rotation of the plane of polarization due to the Faraday effect*

### 1.5.2 Critical state in a thin superconducting strip

There are many, -so-called critical state models-, that describe the intensity and distribution of current flowing in superconductors. The simplest critical state model is called the Bean model [84]. The Bean model is the most widely used to describe current flow in a superconductor. The model assumes that wherever current flows in a superconductor, it flows at a constant $J_c$. The internal magnetic flux density $\boldsymbol{B_{int}}$ is given by

$$\nabla \times \boldsymbol{B}_{\text{int}} = \mu \boldsymbol{J}_c \tag{1.5.3}$$

where $\mu$ is magnetic permeability. The Bio-Savart law provides the integral relation between current density $\boldsymbol{J}$ and magnetic flux density $\boldsymbol{B}$.

$$\boldsymbol{B}(\boldsymbol{r}) = \frac{\mu_0}{4\pi}\int dV' \frac{\boldsymbol{J}(\boldsymbol{r}')\times(\boldsymbol{r}-\boldsymbol{r}')}{|\boldsymbol{r}-\boldsymbol{r}'|^3} \tag{1.5.4}$$

Commercial YBCO CCs have high aspect ratios, widths of 2-12 mm, and a thickness of 0.1 mm. Here, the following theory is focused on thin superconducting films. Brandt *et al.* analytically calculated the current density, magnetic field, penetrated field, and magnetic moment for a thin Type-II superconducting strip carrying a one-way transport current under a magnetic field normal to the thin strip [85], as shown in Figure 1-21. These values were estimated from the Bio-Savart law using complex functions. The thickness of the superconducting strip is too small compared with the width 2$a$. Therefore, the current density distribution along the $z$-axis is negligible. When only a one-way current $I$ is applied, the distributions of sheet current density $J(x)$ and magnetic flux density $B_z(x)$ on the surface of the strip are given by

$$J(x) = \begin{cases} J_c & b < |x| < a \\ \dfrac{2J_c}{\pi}\arctan\left(\dfrac{a^2-b^2}{b^2-x^2}\right)^{1/2} & |x| < b \end{cases} \tag{1.5.5}$$

$$B_z(x)=\begin{cases}\dfrac{\mu x J_c}{\pi|x|}\arctan\mathrm{h}\left(\dfrac{x^2-b^2}{a^2-b^2}\right)^{1/2} & b<|x|<a\\ 0 & |x|<b\end{cases} \tag{1.5.6}$$

Magnetic flux is screened by a screening current corresponding to the critical current, penetrating from the edges of the strip and existing in regions $b<|x|<a$.

$$b=a\sqrt{1-\left(\frac{I}{I_c}\right)^2} \tag{1.5.7}$$

In addition, the sheet current density distribution and magnetic field distribution on the surface of the strip –in which only an external magnetic field with a magnetic flux density of $B_{ex}$ is applied- are given by

$$J(x)=\begin{cases}J_c\dfrac{x}{|x|} & q<|x|<a\\ \dfrac{2J_c}{\pi}\arctan\dfrac{px}{\left(q^2-x^2\right)^{1/2}} & |x|<q\end{cases} \tag{1.5.8}$$

$$B_z(x)=\begin{cases}\dfrac{\mu J_c}{\pi}\arctan\mathrm{h}\dfrac{\left(x^2-q^2\right)^{1/2}}{p|x|} & q<|x|<a\\ 0 & |x|<q\end{cases} \tag{1.5.9}$$

where $p$ and $q$ are given by

$$p=\tanh\left(\frac{\mu\pi B_{ex}}{J_c}\right) \tag{1.5.10}$$

$$q=\frac{a}{\cosh\left(\dfrac{\mu\pi B_{ex}}{J_c}\right)} \tag{1.5.11}$$

A symmetric screening current flows in the opposite direction along the $y$-axis in the superconducting strip under external magnetic field. (1.5.5), (1.5.6), (1.5.8), and (1.5.9) describe distributions from a virgin state, in which no current and magnetic field are applied to the superconducting strip. The current and magnetic field distributions depend on the history of the current and external magnetic field applied to the superconducting strip. Brandt *et al.* also expressed current and field profiles as linear superpositions. For example, sheet current density and distributions were expressed in the situation in which the current is deceased monotonically from $I_0$ to $I$ under no external magnetic field, as follows.

$$J(x,I,J_c)=J(x,I_0,J_c)-J(x,I_0-I,2J_c) \tag{1.5.12}$$

$$B(x,I,J_c)=B(x,I_0,J_c)-B(x,I_0-I,2J_c) \tag{1.5.13}$$

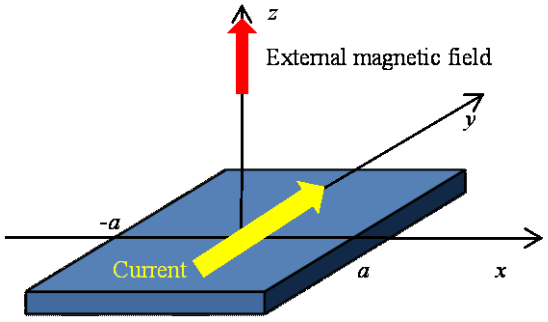


*Figure 1-21 Geometry of superconducting strip carrying transport current under magnetic field normal to the thin strip*

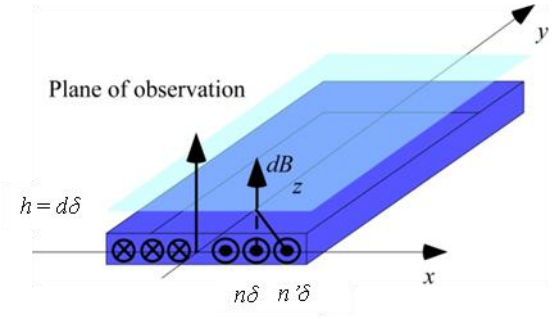


*Figure 1-22: Geometry of the discretized coordinates*

### 1.5.3 Estimation of current distribution in thin films from magnetic field distribution

Many studies have been conducted on actual current distributions in superconducting thin films estimated from magnetic field distributions. The solutions are divisible into two groups according to models of one-dimensional and two-dimensional currents. Macroscopic and microscopic current distributions have been discussed using one-dimensional [84-87] and two-dimensional current distribution models [83, 88-90], respectively. It is easy to measure magnetic flux density ($B_z$ in Figure 1-21) perpendicular to the surface of superconducting thin films. Therefore, the magnetic field distributions along the $z$ axis in a plane parallel ($x$-$y$ plane) to the superconducting thin films are generally measured.

- One-dimensional current distribution

  One-dimensional magnetic field distribution allows us to estimate one-dimensional sheet current distribution. The $z$-component of magnetic flux density $B_z$ at the position of $(x, z) = (x, h)$ is given by

$$B_z(x) = B_{ex} + \frac{\mu_0}{2\pi}\int_{-a}^{a} dx' \frac{x - x'}{h^2 + (x - x')^2} J(x') \tag{1.5.14}$$

  Magnetic flux density generated by current flowing in the superconducting film $\Delta B_z(x)$ is given by:

$$\Delta B_z(x) = B_z(x) - B_{ex} = \frac{\mu_0}{2\pi}\int_{-a}^{a} dx' \frac{x - x'}{h^2 + (x - x')^2} J(x') \tag{1.5.15}$$

  Johansen *et al.* estimated sheet current density $J(x')$ at a point $x'$ from (1.5.15) using the Fourier transform [86]:

$$\mu_0 J(x') = \int_{-\infty}^{\infty} \frac{\Delta B_z(k)}{G(k)} e^{ikx} dk \tag{1.5.16}$$

where $\Delta B_z(k)$ and $G(k)$ are the Fourier transforms of the field profile and integral kernel, respectively. The measurement of magnetic flux densities is generally performed in a low-frequency environment. Assuming that the filter cuts the components with $|k| \geq K$, (1.5.16) is expressed as

$$\begin{aligned} \mu_0 J(x') &= \int_{-\infty}^{\infty} dx A(x'-x) B_z(x), \\ A(\xi) &= \int_{-K}^{K} dk \frac{e^{ik\xi}}{G(k)} = \frac{\xi\left(1 - e^{Kh}\cos K\xi\right) + he^{Kh}\sin K\xi}{h^2 + \xi^2} \end{aligned} \tag{1.5.17}$$

Here, introducing $\delta \equiv \pi/K$ and discretizing the coordinates, $x \equiv n\delta$, $x' \equiv n'\delta$ and $h \equiv d\delta$ shown in Figure 1-22, the (1.5.17) becomes

$$\mu_0 J(n') = \sum_n \frac{n-n'}{d^2 + (n'-n)^2} \frac{1-(-1)^{n'-n} e^{\pi d}}{\pi} \cdot 2B_z(n) \tag{1.15.18}$$

The introduction of the following Hanning filtering function results in a high-frequency cutoff of (1.5.18).

$$W(k) = \begin{cases} \dfrac{\left\{1 + \cos\left(\dfrac{\pi k}{K}\right)\right\}}{2} & |k| \leq K \\ 0 & |k| > 0 \end{cases} \tag{1.5.19}$$

The (1.5.18) becomes

$$\mu_0 J(n') = \sum_n \frac{n'-n}{\pi} \left\{ \frac{1-(-1)^{n-n'} e^{\pi d}}{d^2 + (n'-n)^2} + \frac{\left[d^2 + (n'-n)^2 - 1\right]\left[1 + (-1)^{n-n'} e^{\pi d}\right]}{\left[d^2 + (n-n'+1)^2\right]\left[d^2 + (n-n'-1)^2\right]} \right\} B_z(n) \tag{1.5.20}$$

Bobyl *et al.* and Yoo *et al.* improved the above solution using an iterative calculation [87, 88]. They combined this method with the Bean model. Figure 1-23 shows experimental (a) flux- and (b) current-density profiles determined from MO images. The initially flux-free YBCO strip carryies transport current $I$ =1.8, 2.8, 3.5, 4.3, 4.6 and 4.9 A. Figure 1-23 (c) shows the current density profiles based on (1.5.5) [87].

On the other hand, Ušák *et al.* estimated sheet current distribution using the Tikonov regularization method. The details are described in the section of 3.3.

- Two-dimensional current distribution

In 1988, Roth *et al.* suggested a method to estimate a unique solution to the inverse problems for a two dimensional current distribution [84]. Mathematical techniques of the Fourier transforms and spatial filtering are used in the method. This method has broad utility in processes that requires solving current distributions in superconducting thin films. For example, Koyanagi *et al.* solved the inverse problem using the Hanning window filtering function (1.5.19) [83]. They measured two-dimensional profiles of magnetic flux densities and obtained two-dimensional profiles of sheet current densities, as shown below. The measurement results $B_z(x, y)$ give two-dimensional discrete profiles using the Fourier transform, $b(k_x, k_y)$,

$$b(k_x, k_y) = \sum_{l=0}^{N-1} \sum_{m=0}^{M-1} B_z(l\delta x, m\delta y) e^{-i(k_x l\delta x + k_y m\delta y)} \tag{1.5.21}$$

where $i$, $N$ and $M$ are the imaginary numbers and the numbers of sampling points along the $x$, the $y$ direction, respectively. The Fourier component of sheet current densities $j_x(k_x, k_y)$ and $j_y(k_x, k_y)$ are obtained:

$$j_x(k_x, k_y) = -\frac{2i}{\mu_0} \frac{e^{kh}}{k} k_y b(k_x, k_y) \tag{1.5.22}$$

$$j_y(k_x,k_y)=\frac{2i}{\mu_0}\frac{e^{kh}}{k}k_x b(k_x,k_y) \qquad (1.5.23)$$

where $h$ is the distance between the surface of the superconducting film and the observation plane. The inverse Fourier transforms of $j_x(k_x,k_y)$ and $j_y(k_x,k_y)$ result in sheet current densities $J_x(x,y)$ and $J_y(x,y)$. Figure 1-24 shows (a) the self-field distribution observed from the tape surface of a YBCO CC and (b) two-dimensional current distribution converted from (a) [92].

As seen in Figures 1-23 and 1-24, actual current does not flow symmetrically to the width of the CC because of inhomogeneity in $J_c$.

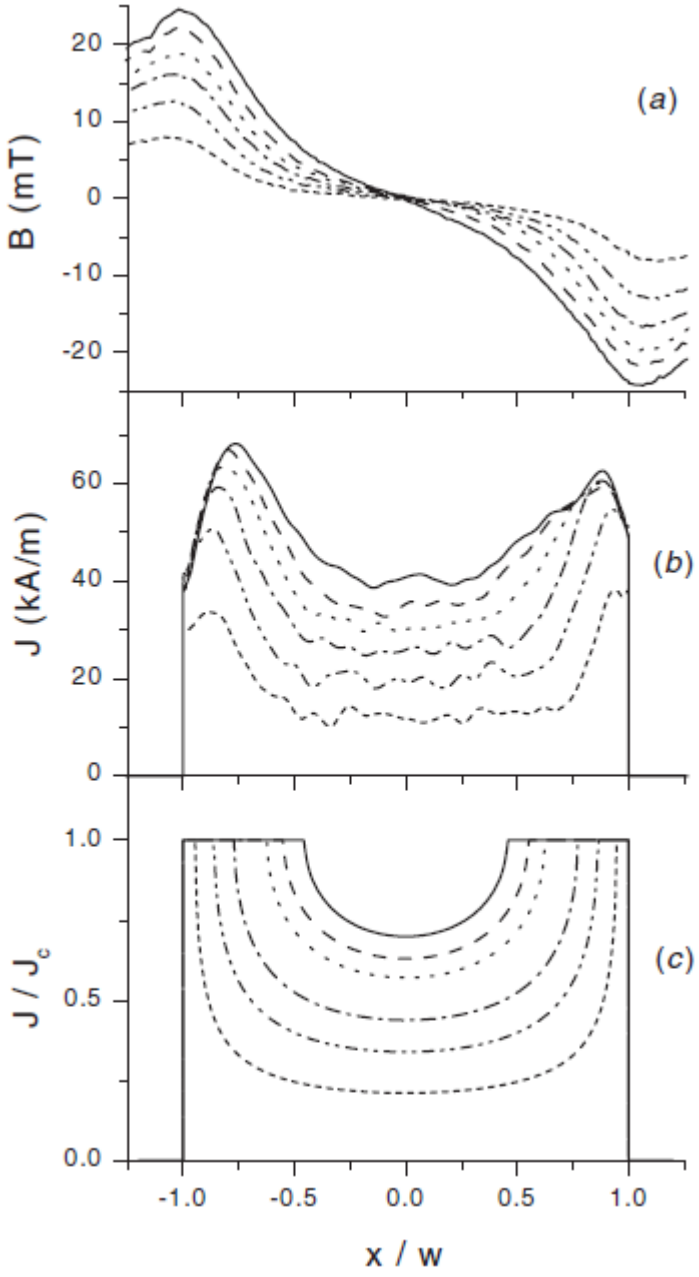


*Figure 1-23: Experimental (a) flux- and (b) current-density profiles determined from MO images. Initially flux-free YBCO strip carries transport current I =1.8, 2.8, 3.5, 4.3, 4.6 and 4.9 A. (c) shows the current density profiles based on (1.5.5).* [87]

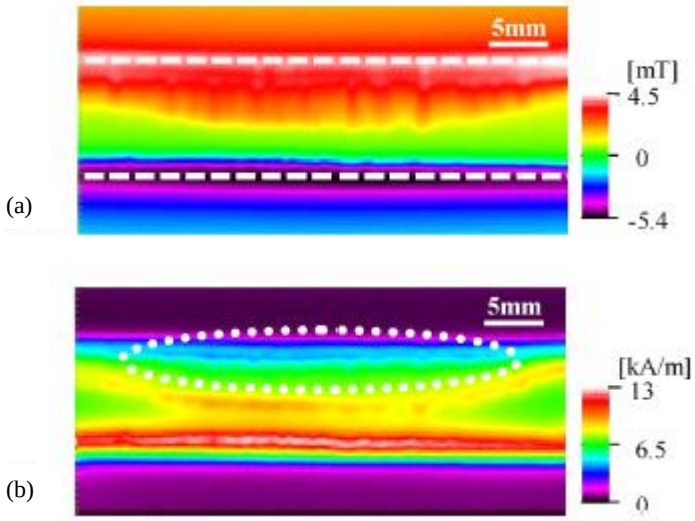


*Figure 1-24: (a) Self-field distribution observed from the tape surface of a YBCO CC and (b) two-dimensional current distribution converted from (a)* [92]

### 1.5.4 Temporal variation in screening current [30,94]

The screening current in a Type-II superconductor decays logarithmically with time because the superconducting state with an inhomogeneous magnetic flux density is in non-equilibrium. The relaxation of the flux is referred to as the flux creep. Anderson and Kim proposed that the flux creep is caused by thermal activation [93]. Flux with density of $\boldsymbol{B}$ motion results in electric field $\boldsymbol{E}$ within the superconductor. Anderson and Kim expressed $\boldsymbol{E}$ as

$$\boldsymbol{E} = \boldsymbol{B} \times v = \boldsymbol{B}\omega d \exp\left(-\frac{U}{k_B T}\right) \tag{1.5.21}$$

where $\omega$, $d$, $U$, $k_B$ and $T$ are the oscillation frequency [95], the hopping distance of the flux, the energy barrier of the pin, the Boltzmann constant and temperature, respectively. Assuming a thin superconducting strip with current in only one direction the $y$-axis in Figure 1-21, the Maxwell equations give

$$\frac{dB_z}{dx} = \mu_0 J_y \tag{1.5.22}$$

$$\frac{dB_z}{dt} = -\frac{dE}{dx} \tag{1.5.23}$$

The time derivative of $J_y$ is given by

$$\frac{dJ_y}{dt} = -\frac{1}{\mu_0}\frac{d^2}{dx^2}E \tag{1.5.24}$$

Assuming a steady flow, this can be simplified to,

$$\frac{dJ_y}{dt} = -\frac{J_c}{\tau_0}\exp\left(-\frac{U}{k_B T}\right) \tag{1.5.25}$$

where $\tau_0$ is a characteristic time. The energy barrier, the so-called pinning potential can be expanded up to linear accuracy [30].

$$U = U_0^*\left(1 - \frac{J}{J_c}\right) \tag{1.5.26}$$

where $U_0^*$ is the apparent pinning potential energy. A logarithmic relaxation of $J$ is obtained as follows.

$$J(t) = J_c\left\{1 - \frac{k_B T}{U_0^*}\ln\left(1 + \frac{t}{\tau_0}\right)\right\} \tag{1.5.27}$$

Given sufficient time, $U_0^*$ is estimated as

$$-\frac{d}{d\log t}\left(\frac{J}{J_c}\right) = \frac{k_B T}{U_0^*} \tag{1.5.28}$$

Accordingly, the temporal variation of the screening current depends on the temperature.

## 1.6 Purpose of This Study

As mentioned in this chapter, YBCO NMR magnets are expected to become the next-generation NMR magnets from the view point of construction of high-field and compact NMR magnets. YBCO pancake coils have the advantage of tolerance against mechanical stress. However, there are still several challenges in terms of fabrication techniques and operating conditions of YBCO coils. In particular, one challenge that remains to be solved is that the screening current in YBCO CCs directly affects the feasibility of YBCO NMR magnets. Further investigations regarding the screening current were carried out in this thesis. These additional investigations have simplified the calculations for electromagnetic design of YBCO magnets and optimization of the operating conditions of the magnet. This chapter presented the properties of the screening current flowing in a YBCO CC as follows:

- Large current corresponding to the superconducting critical current depending on the magnetic field, temperature, and mechanical stress;
- Inhomogeneity of the screening current along the width of the CC;
- Temporal drift of the screening current due to flux creep.

To suggest a design concept of a YBCO magnet by taking into account the properties of the screening current, the following evaluations were performed:

- The current distribution flowing in a YBCO CC was estimated from magnetic field distribution.
- Temporal variations of the screening current were measured.
- Magnetic field distributions induced by screening currents flowing in YBCO CCs and the interaction between the screening currents in CCs were evaluated.
- An electromagnetic design method was suggested for fabricating a YBCO coil taking into consideration the current distribution, temporal variations and the interaction of the screening current between the CCs.

Figure 1-25 shows an overview of this thesis. Chapter 1 describes the background and purpose of this thesis. Experimental equipments used in the following measurements are illustrated in chapter 2. Chapter 3 uses a current-flowing model to discuss a method for estimating the current distribution from magnetic field distribution. Chapter 4 provides distributions of current density, which are solved using the model in chapter 3 in a single CC in which a transport current and an external magnetic field are applied. Chapter 5 expands the current distribution solved in Chapter 4 to magnetic field distribution induced by multiple CCs. Chapter 6 discusses temporal variations of a magnetic field induced by screening currents in CCs and then moves on to temporal variations of the screening currents. Chapter 7 deals with magnetic field distribution generated by coils, by taking into consideration Chapter 5 and Chapter 6. Chapter 8 summarizes this thesis and mentions techniques required to construct YBCO-based NMR magnet.

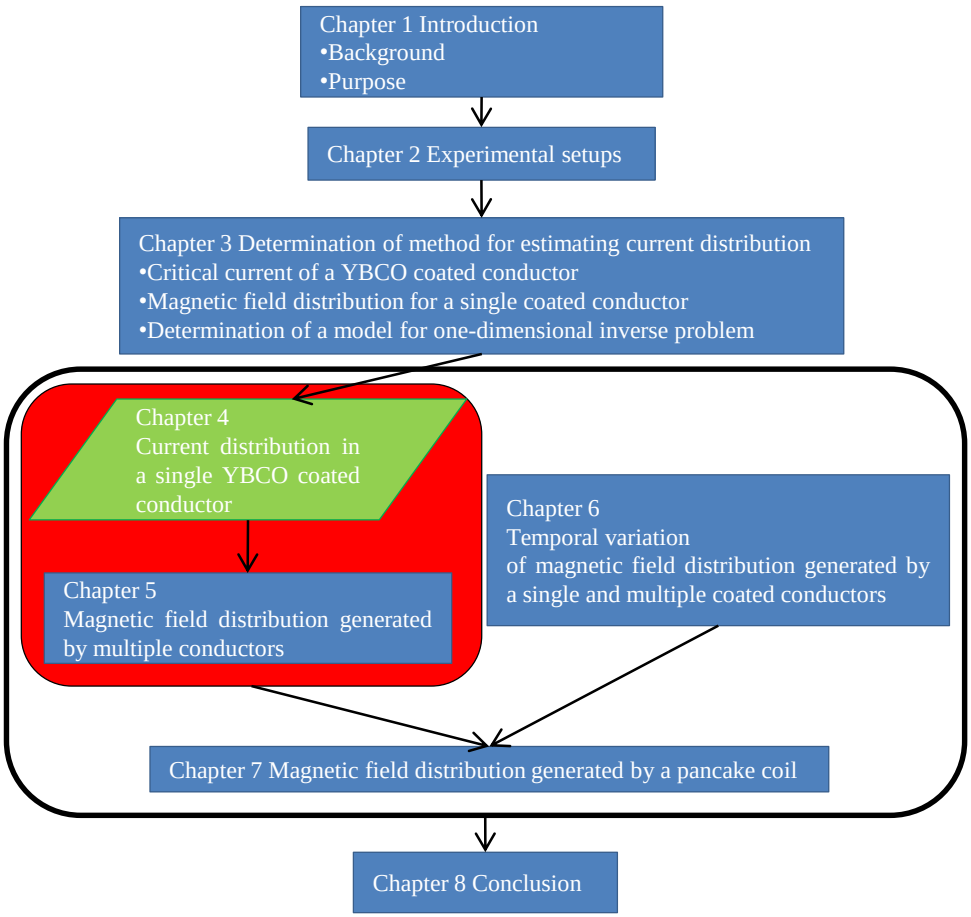


*Figure 1-25: An overview of this thesis*

# Chapter 2

# Experimental Setups

The following measurements were carried out in this study:

A. Measurement of critical current of a YBCO CC under an external magnetic field perpendicular to the tape surface of the CC.

**B.** Measurement of magnetic field distributions induced by currents flowing in the single and multiple CCs under an external magnetic field.

This chapter describes the experimental equipments commonly used in these measurements.

## 2.1 YBCO CCs Used in The Measurements

The CC used in the experiments was a MOCVD YBCO CC, SCS4050, manufactured by SuperPower Inc. Figure 2-1 shows a photo of the CC. The CC has a surrounding copper stabilizer, a width of 4.1 mm, and a 50-μm-substrate made from Hastelloy C-276. Table 2-1 lists the specifications of the CCs.

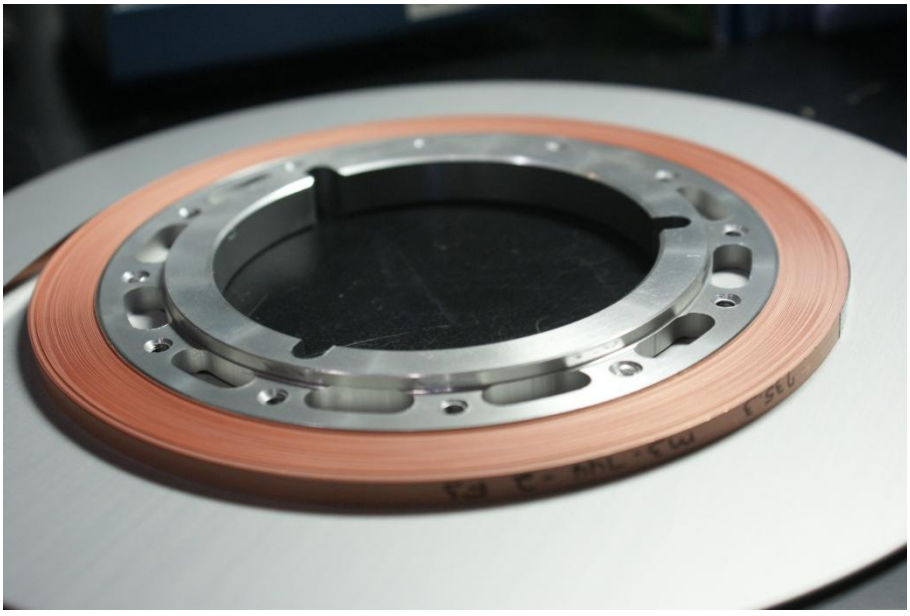

*Figure 2-1: A photo of the CC used in the measurement.*

*Table 2-1: Specifications of the CC used in the measurements.*

| Parameters | Value |
|---|---|
| **Width (2*a*)** | 4.1 mm |
| **Thickness of a CC (*t*)** | 0.1 mm |
| **Thickness of a superconducting layer** | 1 μm |
| **$I_c$ at 77 K, self-field** | 115 A |

## 2.2 Experimental Tools in Cryogen

Figure 2-2 shows a schematic overview of experimental tools in the cryogen, namely, a superconducting magnet, a Hall sensor, current leads, and a jig on which to fix a CC.

- Cryostat and superconducting magnet

  Liquid helium, vaporized helium gas, and liquid nitrogen were employed as the cryogen. Cryostats differ depending on the cryogen. Table 2.1 is a summary of the cryostats used in the measurements. Three kinds of cryostats and superconducting magnets were used in the measurements. A cryostat and a superconducting magnet were required for measuring both, the critical current and the magnetic field distribution. For conducting measurements in liquid helium, two kinds of cryostats, No. 1 and No. 3, were used. The No. 1 cryostat contains an 18 T-superconducting magnet made by JASTEC. The No. 1 cryostat has limited space for specimens, and can only accommodate specimens with lengths up to 40 mm. The No. 3cryostat has the largest bore of 152.4 mm. The magnet attached to the No. 3 cryostat has a large room-temperature bore of 300 mm. The No. 3 cryostat is suitable for large-scale tests, such as coil tests. In addition, the No. 3 cryostat is made of nonmagnetic materials, aluminum, and glass epoxy (GFRP). Figure 2-2 shows a photograph of the No. 3 cryostat and the 5-T superconducting magnet. The sample space in No. 2 cryostat is smaller than those in No. 1 and No. 3. The No. 2 cryostat enables us to vary the temperature of the sample space by adjusting the amount of helium gas and heat generated by a heater attached to the dedicated probe.

  The magnet attached to the No. 1 cryostat can be energized faster than those attached to the other cryostats. Therefore, the No. 1 cryostat and the attached magnet were mainly used in measurements A and B.

- Hall sensor

  Two kinds of Hall sensors are used in measurement B. The active areas and distances between the surface and active areas of the Hall sensors are listed in Table 2.2. The No. 1 Hall sensor has an active area of a circle with a diameter of 0.51 mm. The No. 2 Hall sensor has seven active areas arranged 0.5 mm away from each other, as shown in Figure 2-3. The black part is a package to protect the sensors. The seven sensors lye in a straight line located at the diagonal seven red lines. Both the Hall sensors have high linearity to magnetic fields at low temperatures. However, quantum oscillation for both Hall sensors occurs at 4.2 K under a high field [96]. The Hall sensors were set on the side of the substrate of the CC.

- Current leads and jig

  Copper current leads and voltage taps were soldered. During the soldering, the soldering iron was not attached to the CC so as to avoid deteriorating the YBCO superconducting properties. The nonmagnetic jig was composed of GFRP and brass screws, to get fixed current leads, and a Hall sensor, as shown in

Figure 2-5. Figure 2-5 (a) shows an overview of the jig attached to a CC, which is mounted on the probe for measurement. The jig was adjusted so that the location of the CC should be at the center of the superconducting magnet. Figure 2-5 (b) is an enlarged view of (a). Figure 2-5 (c) shows a Hall sensor that a brass screw gets fixed to. It was difficult to move a Hall sensor in liquid helium. Therefore, a method of scanning a Hall sensor using jigs with different geometry was employed. Figure 2-6 shows a Hall sensor scanned by a brass screw and jigs.

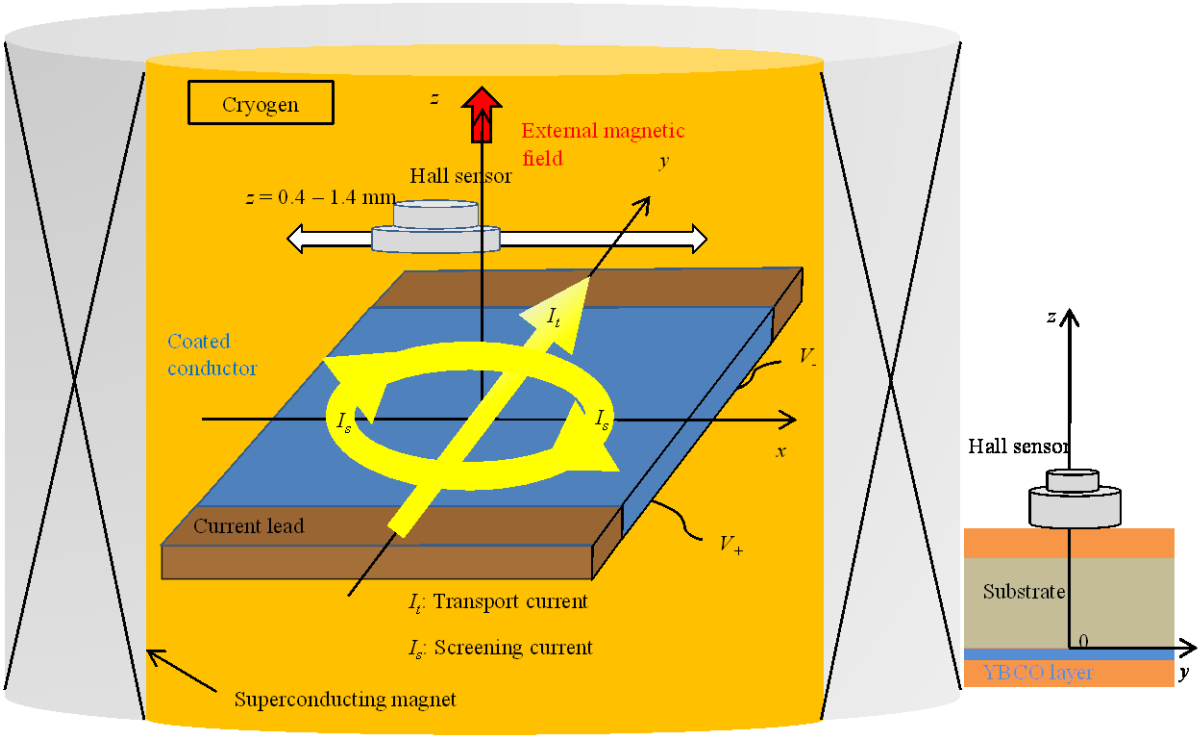


*Figure 2-2: A schematic overview of experimental tools in the cryogen, namely, a cryostat, a superconducting magnet, a Hall sensor, current leads, and a jig to fix a CC.*

*Table 2-2: A summary of cryostats used in the measurements*

| No. | Cryostat (maker) | Bore size (mm) | Measurement | Cryogen | Magnet attached to the cryostat |
|---|---|---|---|---|---|
| **1** | JSD-18T52 at TML (JASTEC) | 52 (Cold bore) | A<br>B | Liquid helium | 18 T (JASTEC) |
| **2** | Cryostat attaching temperature variable probe at TML | | B | Vaporized helium gas | 18 T (JASTEC) |
| **3** | 21-10339 (International Cryogenics Inc.) at UT | 152.4 (Room-temperature bore) | A | Liquid nitrogen<br>Liquid helium | 5 T (KOBELCO) |

TML: Tsukuba Magnet Laboratory at National Institute for Materials Science

UT: The University of Tokyo


*Figure 2-3: A photo of the No. 3 cryostat and the 5-T superconducting magnet*

*Table 2-3: Specifications of Hall sensors*

| No. | Hall sensor (maker) | Active area | Distance between the surface and active area |
|---|---|---|---|
| **1** | BHA-921 (F. W. BELL) | Circle with diameter of 0.51 mm | About 0.86 mm |
| **2** | MULTI-7A (Arepoc s. r. o) | $0.1 \times 0.1$ mm$^2$<br>Active area spacing: 0.5 mm | 0.3 mm |

*Figure 2-4: The front wall of the No. 2 Hall sensor (MULTI-7A)*

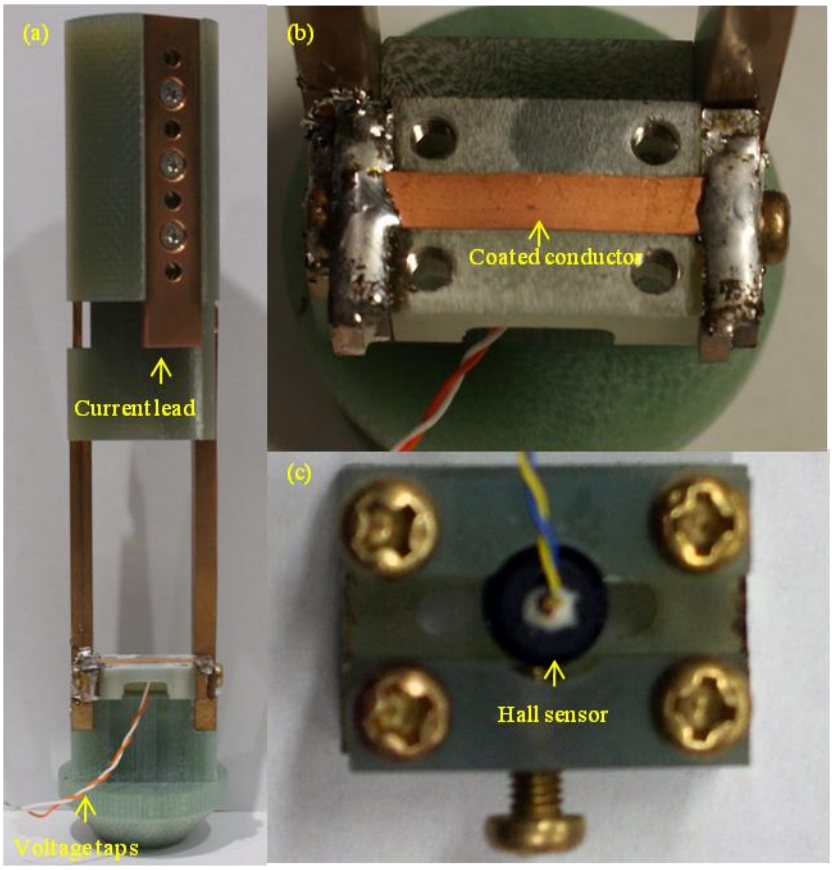


*Figure 2-5: The (a) an overview of the jig attaching a CC, (b) an enlarged view of (a), (c) a Hall sensor that a brass screw gets fixed to.*


*Figure 2-6: A Hall sensor scanned by a screw.*

## 2.3 Measurement System

Figure 2-7 shows electric devices connected to each other using GP-IB (IEEE 488) cables when measuring magnetic field distributions induced by a current in a CC while external magnetic fields are applied. The devices used are as follows: seven voltmeters (nanovoltmeter 2182A, Keithley instruments Inc.) for the No. 2 Hall sensor, a voltmeter (nanovoltmeter 2182A, Keithley instruments Inc.) for measuring the electric field in the CC, a voltmeter (Model 2000, Keithley instruments Inc.) to read a current supplied to the superconducting magnet, a voltmeter (Model 2000, Keithley instruments Inc.) to read the transport current, and two DC power supplies to the CC. These devices were controlled by a laptop-PC. Figure 2-8 shows an actual photograph of these devices except for the two DC power supplies. Figure 2-9 shows the equipment, an 18-T superconducting magnet and the power supply, used for applying an external magnetic field, and the electrodes used for supplying current to the CC.

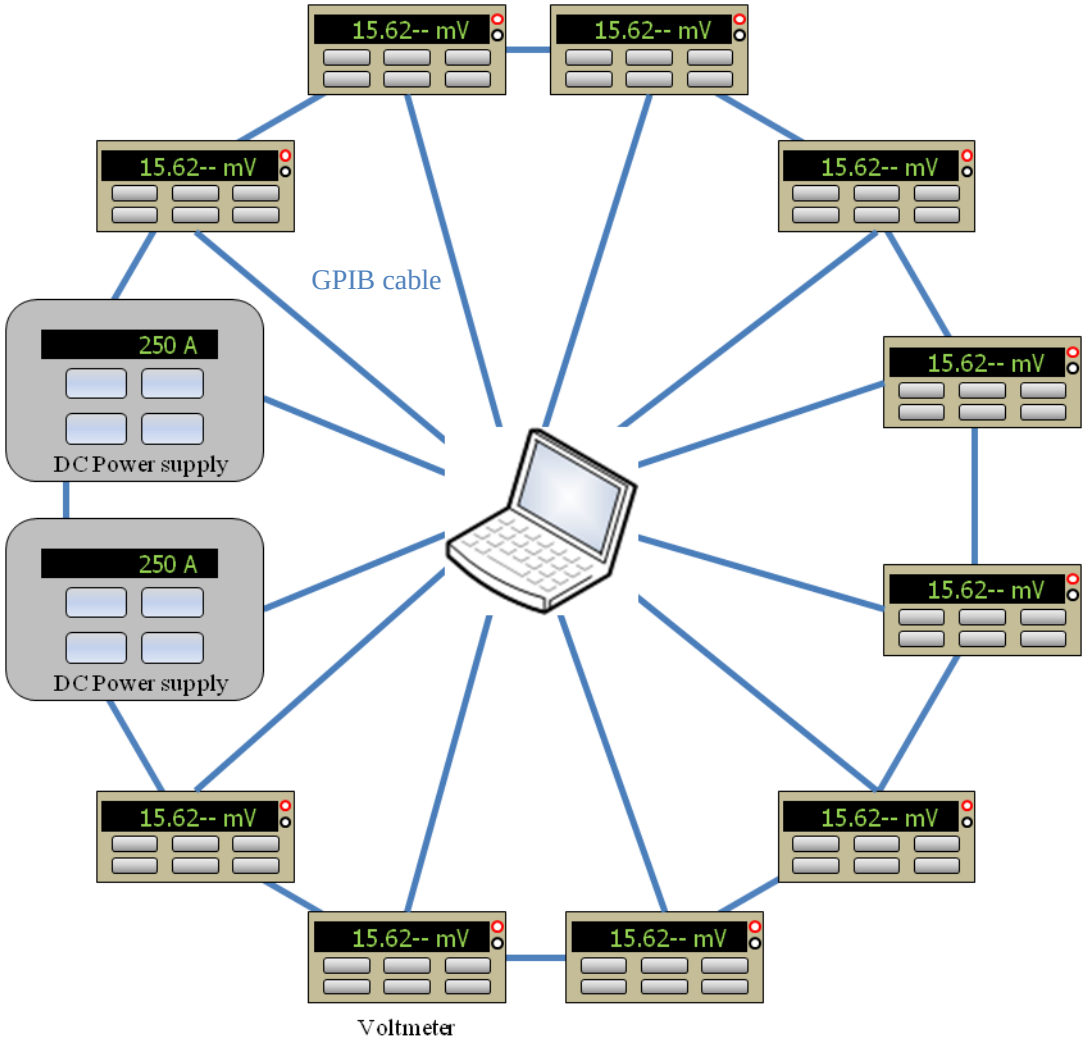


*Figure 2-7: Electric devices controlled by a PC.*

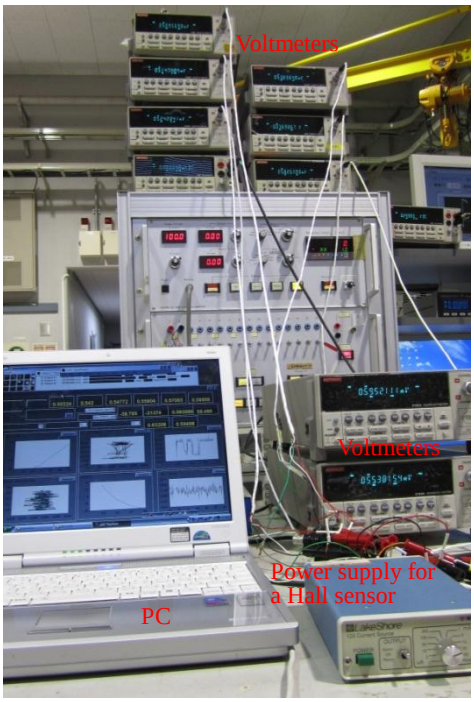


*Figure 2-8: Actual image of electric devices used in the experiment.*


*Figure 2-9: Equipment to apply external magnetic field and electrodes supplying current to the CC.*

# Chapter 3

# Determination of Method for Estimating Current Distribution

As stated in Chapter 1, there are many approaches to current distribution in superconducting thin films. This thesis focuses on current distribution that is possible to apply to electromagnetic designs of YBCO coils. Transport and screening currents flow in a CC wound into the coil. The distribution of the total current is influenced by the distribution of the critical current density of a CC. Section 3.1 discusses the magnetic-field dependence of the critical current of the CC. In section 3.2, a simple model for screening current flow in a CC is suggested and verified. Section 3.3 presents a model for evaluating current distribution in a CC which is based on the simple model in the section of 3.2. In section 3.4, current distribution is estimated using the model and verified.

## 3.1 Magnetic Field Dependence of Critical Current

Many critical state models, including the Bean model, describe magnetic-field dependence of a critical current, $I_c$ [4]. Inoue *et al.* estimated *E-J* characteristics for a YBCO CC at low temperature and high field based on the percolation model [97]. This section presents critical currents of the CC under magnetic field perpendicular to the tape surface, where the amount of the magnetic flux penetrating the CC becomes largest.

### 3.1.1 Procedures of measurement of critical current

Figure 3-1 shows a CC soldered to current leads. The setup is used when conducting the measurement in liquid helium. The voltage taps are soldered to the surface of the CC. We applied an external magnetic field along the *z*-axis, with flux densities up to 18 T and 3.5 T in liquid helium and liquid nitrogen, respectively. When the transport current, $I_t$, was supplied to a CC by a power source under a static magnetic field, an electric field was observed. We define $I_c$ as the value of the current at $E$ = 1 μV/cm.

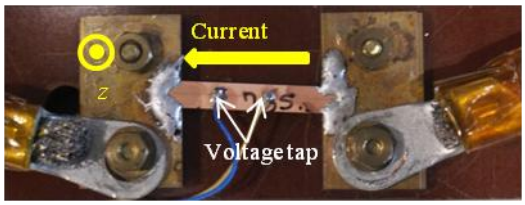


*Figure 3-1: A setup for measuring critical current in liquid nitrogen*

### 3.1.2 Results and discussion

Figure 3-2 shows the electric field-current (*E*-*I*) curve of the CC at 4.2 K under 2 T. The open circles are experimental values. When $I_t$ increased from 0 A to 400 A, the electric field strength did not generate an electric field. When $I_t$ reached approximately 410 A, the strength of electric field steeply increased due to the generation of resistance and heat. The *E*-*J* curve generally is given by:

$$E = E_c\left(\frac{I}{I_c}\right)^n \tag{3.1.1}$$

where $E_c$ is the electric field strength at $I = I_c$ and $n$ is called the $n$-value. The temperature and magnetic-field dependence of $n$ can provide insight into the property of the dissipation process of the CC. The curve was plotted based on (3.1.1).

Figure 3-3 shows the critical currents measured at 4.2 K and 77 K as functions of the external magnetic field parallel to the *z*-axis. The symbols are experimental values. Inoue *et al.* [97] expressed the magnetic-field dependence $I_c$ as

$$I_c(B) = \alpha\left(\frac{B_{ex}}{\beta}\right)^{\gamma}\left(1-\frac{B_{ex}}{\beta}\right)^{\delta} \tag{3.1.2}$$

where $B_{ex}$ is magnetic flux density of the external magnetic field and $\alpha$, $\beta$, $\gamma$ and $\delta$ are fitting parameters. In Figure 3-3, $\alpha$, $\beta$, $\gamma$, and $\delta$ are 50.9, 247, -0.444, and 3.33, respectively. (3.1.2) is used for magnetic fields in which the magnetic flux is present over the entire width of the CC.

Figure 3-4 shows the $n$-values at 4.2 K and 77 K as functions of an external magnetic field parallel to the tape surface of the CC. The $n$-values at 77 K are more sensitive to the magnetic field along the *z*-axis than those at 4.2 K. The dissipation process at 4.2 K does not depend on the magnetic field when the magnetic flux density is below 18 T.

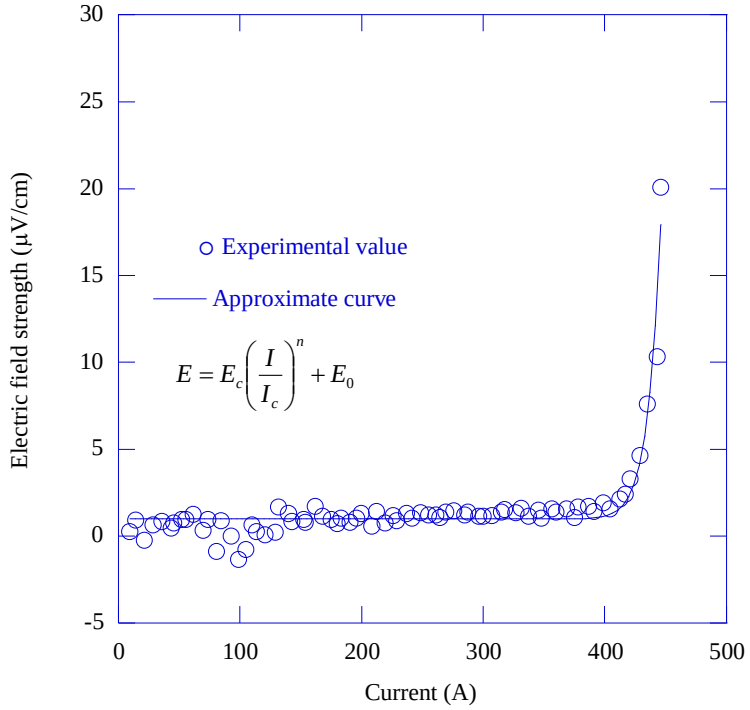


*Figure 3-2: An electric field-current (E-I) curve of the CC at 4.2 K under 2 T. The curve is plotted based on (3.1.1).*

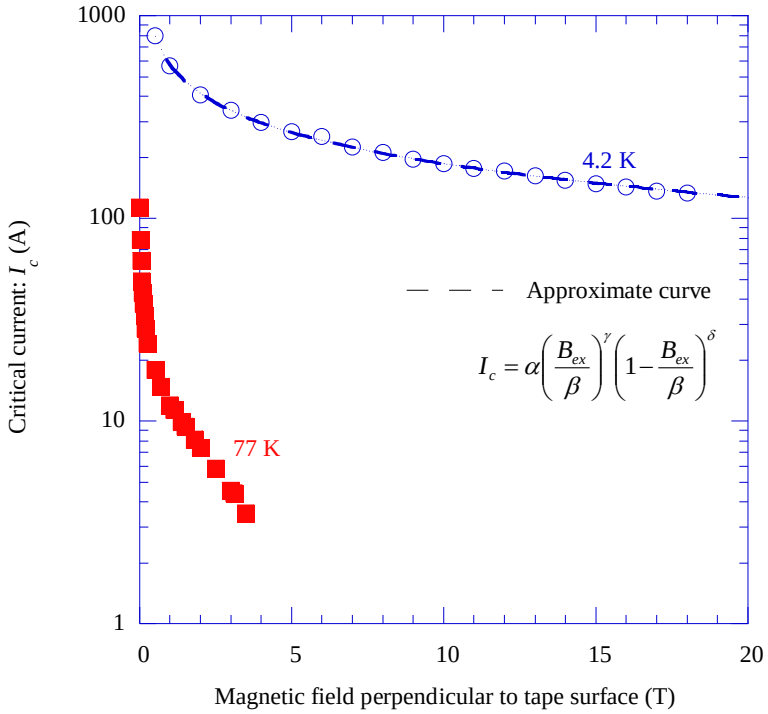


*Figure 3-3: Critical currents measured at 4.2 K and 77 K as functions of an external magnetic field parallel to the z-axis. Blue circles and red squares show experimental values at 4.2 K and 77 K, respectively. The dashed line is a curve approximated by (3.1.2).*

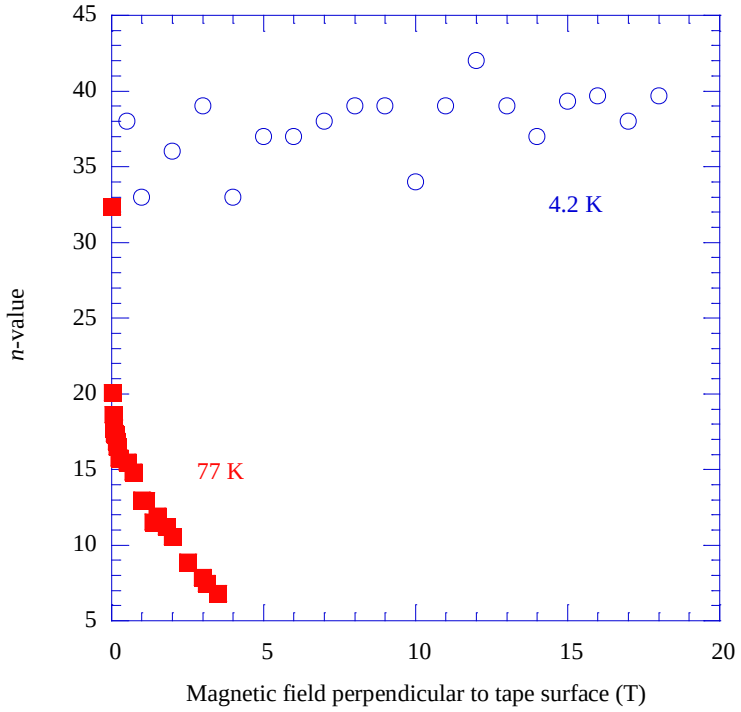


*Figure 3-4: n-values at 4.2 K and 77 K as functions of an external magnetic field parallel to the z-axis. Blue circles and red squares show experimental values at 4.2 K and 77 K, respectively.*

## 3.2 Magnetic Field Distribution above The Center of The CC

As mentioned in chapter 1, the intensity of the screening current increases and decreases with that of the critical current. Many studies treat current distributions in thin superconducting films one- or two-dimensionally. Essentially, macroscopic current distributions are described one-dimensionally. In contrast, the size of a sample space is limited by the bore size of the cryostat. That is why a CC should be cut to be at most 40 mm in length when conducting measurements in liquid helium. This section explains that the current distribution in a short CC can be described one-dimensionally.

### 3.2.1 Experimental procedures

CCs were cut into short specimens, with lengths of 20 mm. Figure 3-5 shows a schematic diagram of the measurements of the screening-current-induced field (SCF) generated in a CC. The CC was inserted into the bore of a superconducting magnet attached to the No. 1 cryostat, which was used to apply an external field to the CC. External magnetic fields varying from 0 T to 18 T and 18 T to 0 T were applied. The rates of charging and discharging magnetic fields of 0 T to 15 T and 15 T to 18 T were ±14.4 mT/s and ±7.2 mT/s, respectively, due to the maximum rate of charging and discharging the magnet. This indicates that the rates are independent of the SCF in appendix A. The CCs were cooled down using liquid helium and helium gas. We defined a position ($x$, $y$, $z$) = (0, 0, 0) as the center of the top surface of the CCs. In the experiments, magnetic flux densities ($B_z$) in the direction of the $z$-axis at positions ($x$, $y$, $z$) = (0, 0, $z$) were measured with the No. 1 Hall sensor.

The SCFs were evaluated according to the following procedure: 1) we measured magnetic fields with and without CCs under charging and discharging external magnetic fields; 2) we subtracted the values of magnetic fields without CCs from those of magnetic fields with CCs under charging and discharging external fields, respectively; 3) we defined the SCFs as half of the difference of the measured fields at the same external fields, when charging and discharging. The SCFs do not include magnetization influences of paramagnetic materials under a high field.

### 3.2.2 One-dimensional symmetric current model

Let us consider a high-field region in which magnetic flux spans the entire width of the CC. Assuming that $l \to \infty$, symmetric screening currents in directions of $\pm y$ are induced by a magnetic field perpendicular to the tape surfaces, as shown in Figure 3-5. Then, a $B_z$ of the SCF is given using a width of $2a$ = 4 mm, a thickness of 1 μm, and a length of $l$ = 20 mm of a superconducting layer:

$$B_z(0,0,z) = \frac{\mu_0 I}{\pi a} \ln\left(\frac{\sqrt{a^2 + z^2}}{z}\right) \tag{3.2.1}$$

where $\mu_0$ is the permeability of free space.

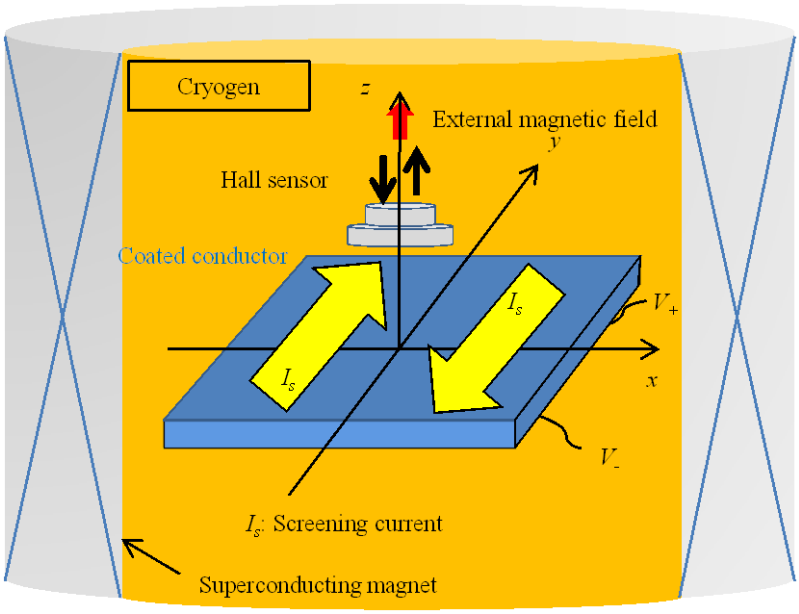


*Figure 3-5: Schematic diagram of measurements of magnetic fields generated by screening currents on a coated conductor*

### 3.2.3 Results and discussion

Figure 3-6 shows SCFs as a function of $z$ under varying external magnetic fields. Blue open circles, red open triangles, green open squares, and black open diamonds, which are evaluated from experimental data, show SCFs at positions of $z$ = 2 mm, 3 mm, 5 mm and 9 mm, respectively. The dashed lines in Figure 3-6 were drawn by substituting the magnetic-field dependence of $I_c$ at 4.2 K shown in Figure 3-3 into (3.2.1). The experimental and calculation results agree well. The agreement indicates that the screening currents can be described one-dimensionally in Figure 3-5, even for the short length of 20 mm.

Figure 3-7 shows the SCFs at a position ($x$, $y$, $z$) = (0 mm, 0 mm, 2 mm) as a function of temperature. The dashed lines are curves approximated by a combination of (3.1.2) and (3.2.1). Here, the screening current, $I$, in (3.2.1) is equal to $I_c/2$. In Figure 3-7, σ is also a fitting parameter. Conversely, the magnetic-field dependence of $I_c$ at 20 K and 30 K were calculated from the approximated curve. The $I_c$ at 20 K and 30K are drawn in Figure 3-8. The $I_c$ of the CC under a magnetic field perpendicular to the tape surface is lower than that of the CC under magnetic fields with any angles to the tape surface. An operating current density of a superconducting magnet more than 100 A/mm$^2$, which is determined by coil shapes, is required to generate a high magnetic field. A thickness and a width of the CC are 0.1 mm and 4.1 mm, respectively. Therefore, an operating current over 41 A for a high-field YBCO magnet is needed. Operating temperatures of a high-field YBCO magnet should be below 20 K.

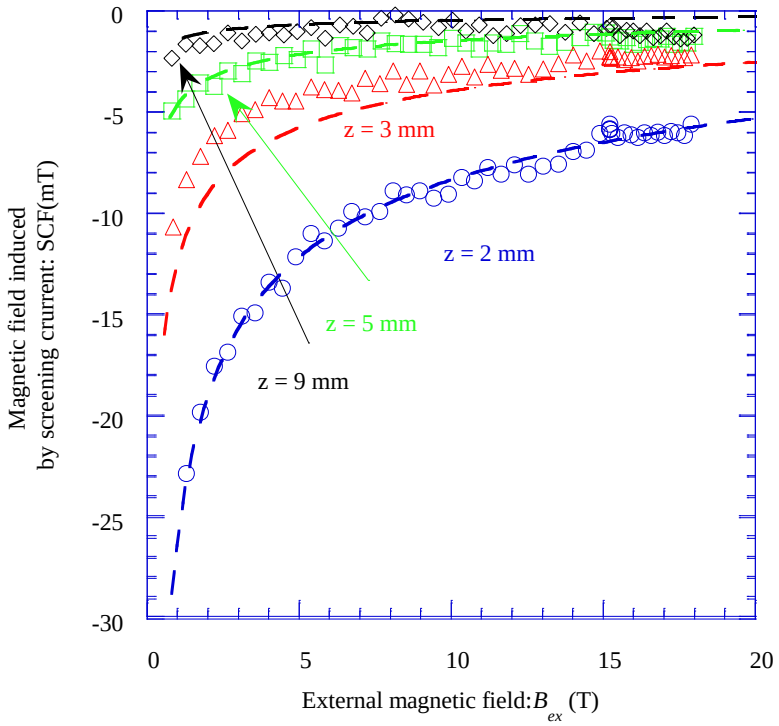


*Figure 3-6: SCFs above the center of the CC under external magnetic fields as a function of z. Blue circles, red triangles, green squares and black diamonds show experimental values for z = 2 mm, 3 mm, 5 mm, and 9 mm, respectively. The dashed lines were calculated using (3.1.2) and (3.2.1).*

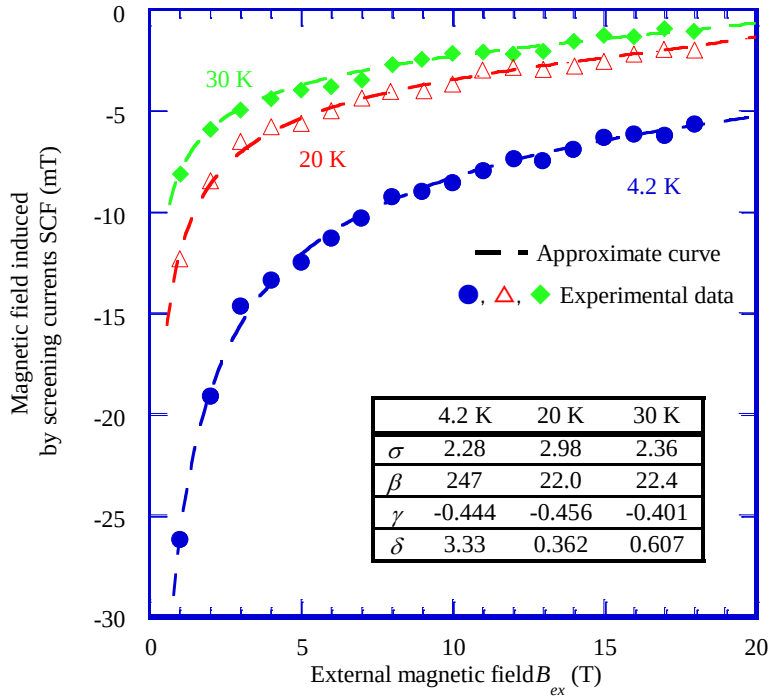


| | 4.2 K | 20 K | 30 K |
|---|---|---|---|
| $\sigma$ | 2.28 | 2.98 | 2.36 |
| $\beta$ | 247 | 22.0 | 22.4 |
| $\gamma$ | -0.444 | -0.456 | -0.401 |
| $\delta$ | 3.33 | 0.362 | 0.607 |

*Figure 3-7: SCFs at a position of (x, y, z) = (0 mm, 0 mm, 2 mm) as function of temperatures. Blue circles, red triangles, and green diamonds show experimental values at 4.2 K, 20 K and 30 K, respectively. The dashed lines are curves approximated by (3.1.2).*

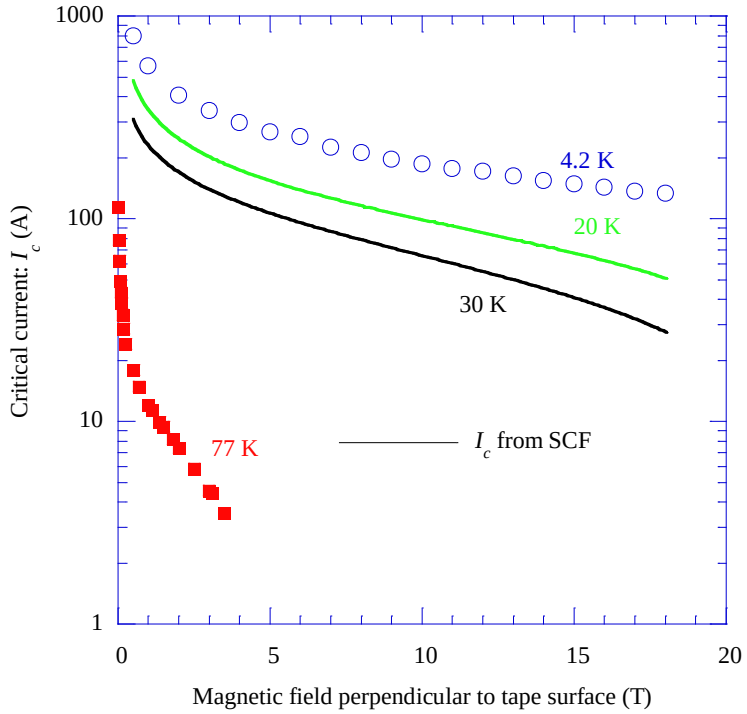


*Figure 3-8: Critical current of the CC at 4.2 K, 20 K, 30 K, and 77 K as a function of external magnetic field perpendicular to the tape surface. The critical current at 20 K and 30 K were estimated from the screening-current-induced field.*

## 3.3 A Model for Calculating Current Distribution

In section 3.2, we explained that expressing the SCF using a one-dimensional symmetric current model was reasonable. The expansion of this model is an effective way to express the current flowing in a CC.

### 3.3.1 A model of a solution for the one-dimensional inverse problem

A CC was divided into the *n* areas in which uniform one-dimensional currents flowed along the *y*-axis, as shown in Figure 3-9. Compared to the width, the thickness of the superconducting layer is so small that current distribution along the *z*-axis is negligible. Here, $B_z$ on $z = h$ is described by Biot-Savart's law

$$B_z(x,h) = B_{ex} + \frac{\mu_0}{4\pi} \times \sum_{k=1} J_y(k) \log\left( \frac{(x+a-(k-1)d)^2 + h^2}{(x+a-kd)^2 + h^2} \right) \tag{3.3.1}$$

where $J_y(k) = \int j(x,z)dz$ is the sheet current density in $Am^{-1}$. The $j(x, z)$, the current density, is integrated over the thickness. The second term of (3.3.1), which shows magnetic flux density resulting from current in the CC, was replaced by

$$\mathbf{B} = \mathbf{AJ} \tag{3.3.2}$$

where $\boldsymbol{B} \equiv (B_z(x_1,h),..., B_z(x_m,h))$, $\boldsymbol{J} \equiv (J_y(1),..., J_y(n))$ and $\mathbf{A}$ is a $m \times n$ matrix. Here, $m$ is the number of the sampling points.

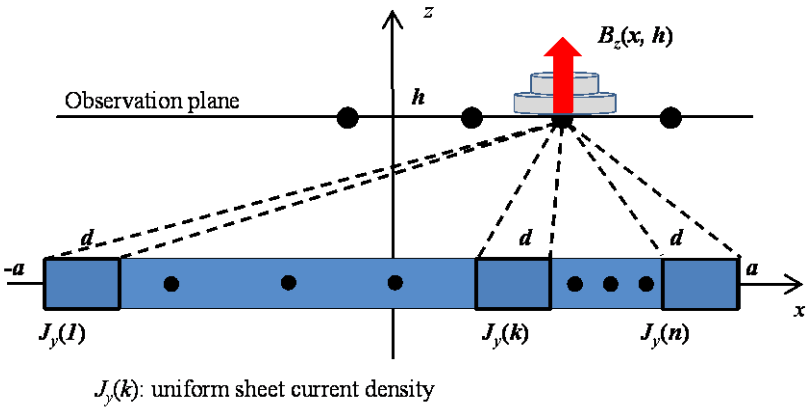


*Figure 3-9: Geometry to solve one-dimensional inverse problem.*

### 3.3.2 Solution of the one-dimensional inverse problem using the Tikhonov regularization method

The value of **J** obtained directly from (3.3.2) can have a large dissipation due to **B** having the following errors.

- Errors of the sampling position
- Errors of linearity of the Hall sensors due to the quantum oscillations at 4.2 K and under a high field

We can use the linear least-squares method to solve for **J** in (3.3.2). That is, the method requires the norm (3.3.4) to minimize

$$\|\mathbf{AJ} - \mathbf{B}\|^2 \tag{3.3.3}$$

(3.3.4) is ill-conditioned and cannot be solved.

The Tikhonov regularization was used to solve an inverse problem of **J** from **B** with errors in (3.3.2) as described in [89, 98, 99]. The method gives approximate solutions of **J** by minimizing the function

$$f = \|\mathbf{AJ} - \mathbf{B}\|^2 + \lambda\|\mathbf{J}\|^2 \tag{3.3.4}$$

where $\lambda$, a real number, is a parameter that must be minimized (3.3.4). In this calculation, $\lambda$ = 5e-9. The detail giving $\lambda$ is described in appendix B.

## 3.4 Validity of The Solution for Calculating Current Distribution

The validity of the model and the solution described in section 3.3 is verified in this section. This section discusses sheet current distributions calculated from magnetic field distributions using experimental results and calculation results based on Brandt's critical state model, expressed as (1.5.5) and (1.5.6).

### 3.4.1 Distribution of sheet current density from SCF

This section presents the distribution of sheet current density in a CC calculated from the distribution of the SCF under a low field in which magnetic flux does not reach the center of the CC.

#### 3.4.1.1 Procedures for measuring the SCF distribution along the *x* axis

We measured the distributions of the *z*-component of magnetic flux densities, $B_z$, both with and without a CC, under charging and discharging external magnetic fields with magnetic flux densities in the range of 0 T to 5 T. The difference, $\Delta B_z$, between $B_z$ with and without a CC was defined as the SCF. The No.2 multi-arrayed Hall sensor was used in this measurement. The rate of the varying external field was ±14 mT/s. The intensities of the SCF were constant at rates of varying external magnetic fields between 3.5 mT/s and 14 mT/s. In this measurement, it was assumed that distributions of the SCF were symmetric over the width of the CC.

#### 3.4.1.2 Results and discussion

Figure 3-10 shows the magnetic flux density, $\Delta B_z$, at the position ($x$, $z$) = (0.2 mm, 0.4 mm) generated by a screening current under a varying external magnetic field. Two arrows point in the direction of the varying external magnetic field. As the external magnetic field increases, the value of $\Delta B_z$ decreases linearly. The value of $\Delta B_z$ is lowest when the external magnetic field has a magnetic flux density of about 0.3 T, when the magnetic flux reaches the center of the CC. As the external magnetic field increases further, the value of $\Delta B_z$ varies depending on $I_c$-$B$, as described in Figure3-3. When external magnetic field goes up to 5 T and then decreases slightly, the value of $\Delta B_z$ changes from negative to positive. The value of $\Delta B_z$ does not go back to zero in the absence of the external magnetic field. The remnant magnetic field decays with logarithm of time, as described in chapter 6.

Figure 3-11 shows the distributions of magnetic flux density in the CC during an increase in the external magnetic field. The symbols show the experimental results. Solid lines are drawn using the Brandt's critical state model (1.5.7). Dashed lines are calculated from the sheet current density in Figure 3-12. The lower the external magnetic field is, the better the agreement between the experimental results and the solid lines. The dashed lines, being the forward problem solution, agree well with the experimental results, regardless of the strength of the external magnetic field. Figure 3-12 describes the distributions of sheet current density in the CC during an increase in the external magnetic field. The symbols were calculated from the distributions of magnetic flux density. The dashed lines are drawn using the Brandt's critical state model (1.5.8). As the external magnetic field increases, the sheet current density within the CC becomes large. The sheet current density then becomes flat over the half the width of the CC at about 0.3 T, when the magnetic flux goes to the center of the CC. If we consider the sheet current as a one-dimensional current, the gradients of the magnetic flux density on the surface of the CC correspond to the intensity of the current. Figure 3-11 and Figure 3-12 are valid results.

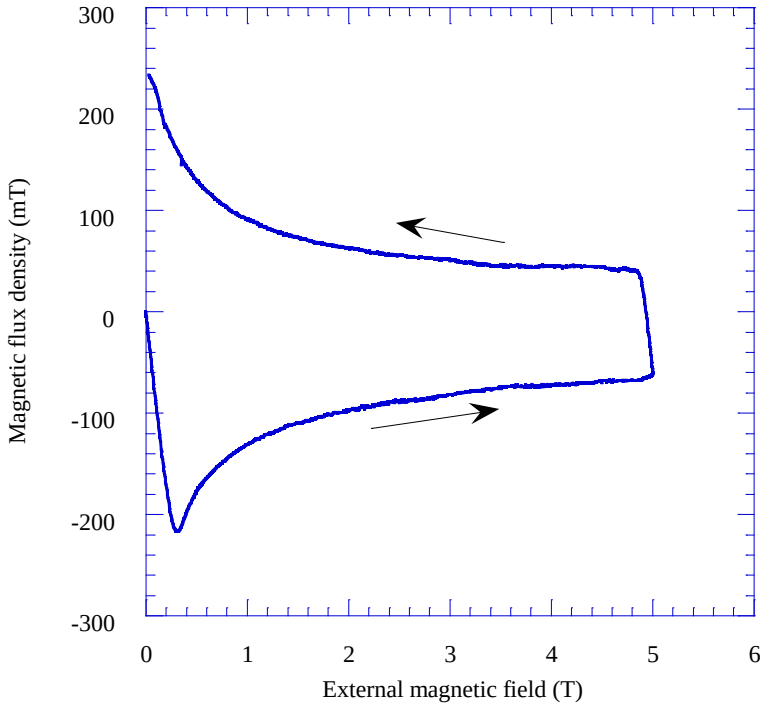


*Figure 3-10: Magnetic flux density at position (x, z) = (0.2 mm, 0.4 mm) generated by screening current under varying external magnetic field. The two arrows show directions of the varying fields.*

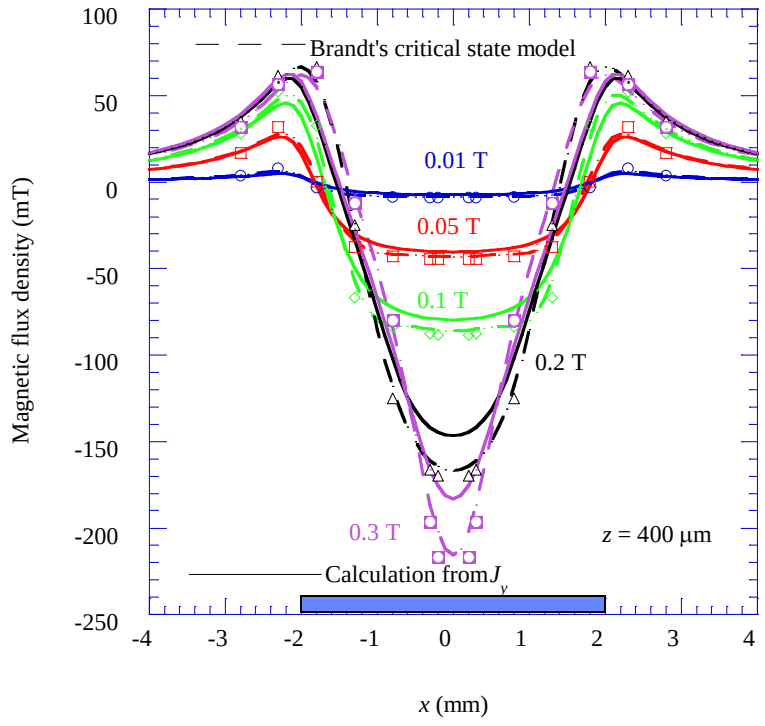


*Figure 3-11: Distributions of magnetic flux density in the CC during an increase in external magnetic field. Symbols are experimental values. Solid lines are plotted using the Brandt's critical state model (1.5.7). Dashed lines are calculated from the sheet current density in Figure 3-12.*

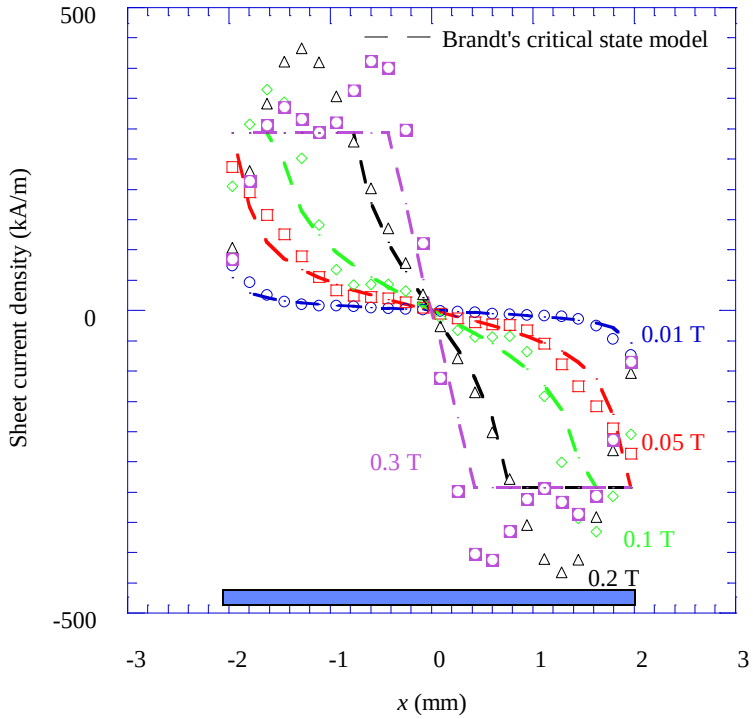


*Figure 3-12: Distributions of sheet current density in the CC during an increase in external magnetic field. Symbols were calculated from the distributions of magnetic flux density. Dashed lines are drawn using Brandt's critical state model (1.5.8).*

### 3.4.2 Distribution of sheet current density from self-field

This section presents the distribution of the sheet current density in a CC calculated from the distribution of a self-field. The self-field is generated when a transport current is applied to the CC.

#### 3.4.2.1 Procedures for measuring self-field distribution

A YBCO coated conductor (CC) was cooled using liquid helium. Then, a DC electric transport current, $I_t$, was supplied to the CC, continuously increasing from 0 A to 800 A. Subsequently, magnetic flux density was measured at a position using the No. 1 Hall sensor. The Hall sensor was scraped off and the distance between the surface and the active area was reduced to 0.4 mm. After the $I_t$ had returned to 0 A, the CC was heated in order to remove any remnants of screening currents. The Hall sensor was shifted at the other position 0.5 mm away from the original position.

#### 3.4.2.2 Results and discussion

Magnetic flux densities were measured at 14 positions of ($x$, $z$) = (±0.1 mm, 0.5 mm), (±0.6 mm, 0.5 mm), (±1.1 mm, 0.5 mm), (±1.6 mm, 0.5 mm), (±2.1 mm, 0.5 mm), (±2.6 mm, 0.5 mm), and (±3.1 mm, 0.5 mm). Figure 3-13 shows the distributions of the self-field on $z$ = 0.5 mm. Dashed lines were calculated from the sheet current densities shown in Figure 3-14. Assuming that $I_c$ is 1200 A at 4.2 K and the self-field, the dotted line in Figure 3-13, is calculated from (1.5.5). The $I_c$ is estimated from $I_c$-$B$ curve shown in Figure 3-3. The blue bar on the bottom of Figure 3-13 represents a CC. The actual magnetic field distributions immediately above the CC agree with those calculated from the distributions of the sheet current density better than they do with those calculated from Brandt's critical state model. This indicates that the critical current density near the edges of the CC is lower, and that the actual magnetic flux goes deeper into the center of the CC.

The YBCO CC was divided into 16 sections, in which uniform sheet current flowed. Figure 3-14 shows distribution of sheet current densities in the CC. The symbols show the experimental data. As the $I_t$ increases, the sheet current densities increase over the width and their symmetry over the CC width break. This is caused by local inhomogeneities in critical current densities. Dashed lines show sheet current densities based on Brandt's critical state model. The solid and dashed lines agree well, especially in low $I_t$ (100 – 400 A). The solution of the one-dimensional inverse problem could not stand for a nonlinearly increased sheet current density near the edges of a CC.

Figure 3-15 and Figure 3-16 show the distributions of the magnetic flux densities on $z$ = 1 mm and $z$ = 1.4 mm, respectively. The dashed lines were estimated from $J_y$, as the solution calculated from self-field distribution on $z$ = 0.5 mm, as shown in Figure 3-14. The agreement between the actual densities and the calculation results enhances the validity of the sheet current densities shown in Figure 3-16.

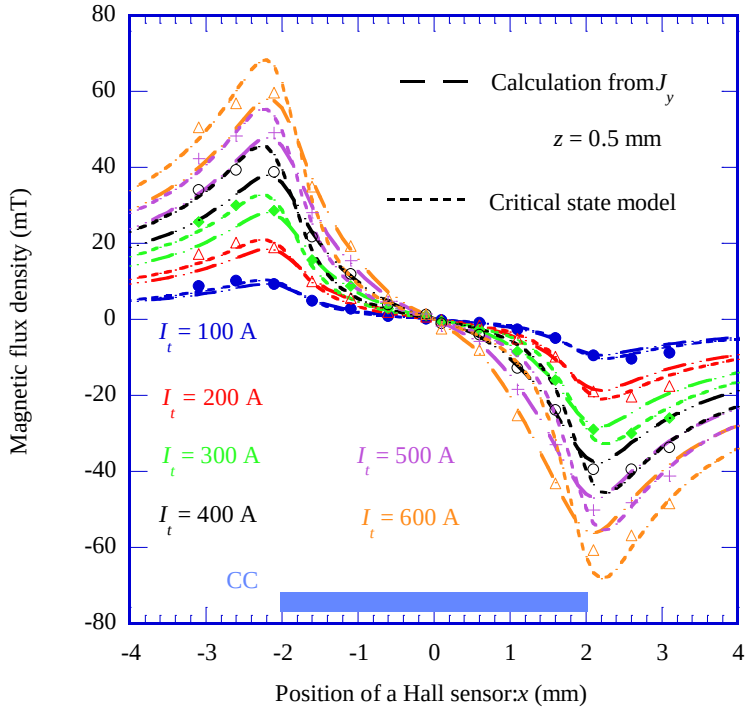


*Figure 3-13: Distributions of magnetic flux density at z = 0.5 mm generated by a CC that transports currents of 100 A, 200 A, 300 A, 400 A, 500 A, and 600 A. Symbols are experimental results. Dashed lines are calculated from the sheet current densities described in Figure 3-14. Dotted lines are estimated using (1.5.5).*

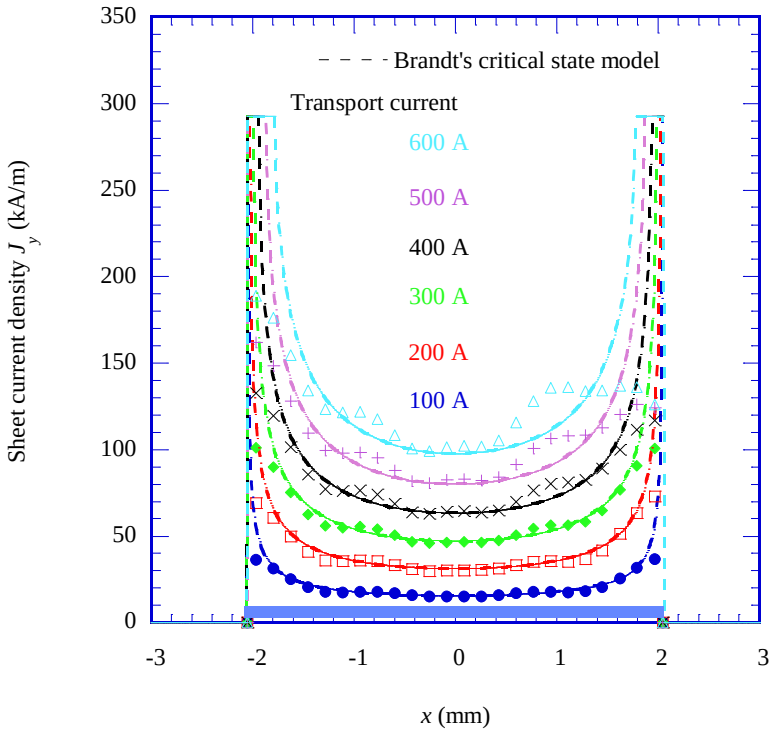


*Figure 3-14: Distributions of sheet current density in a CC transporting 100 A, 200 A, 300 A, 400 A, 500 A, and 600 A currents. Symbols are experimental results. Dashed lines estimated using (1.5.6).*

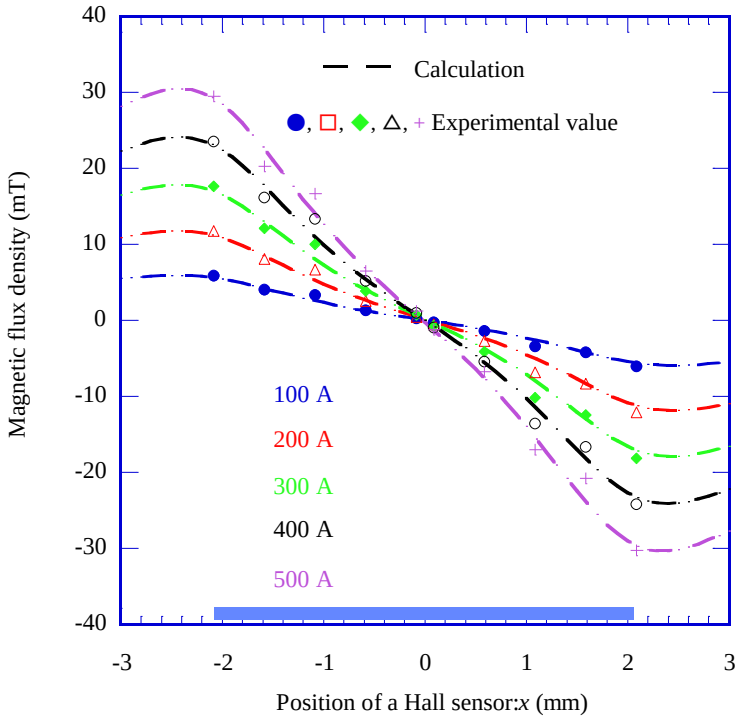


*Figure 3-15: Distributions of magnetic flux density at z = 1 mm generated by a CC transporting 100 A, 200 A, 300 A, 400 A and 500 A currents. Symbols are experimental results. Dashed lines are calculated from the sheet current densities described in Figure 3-14.*

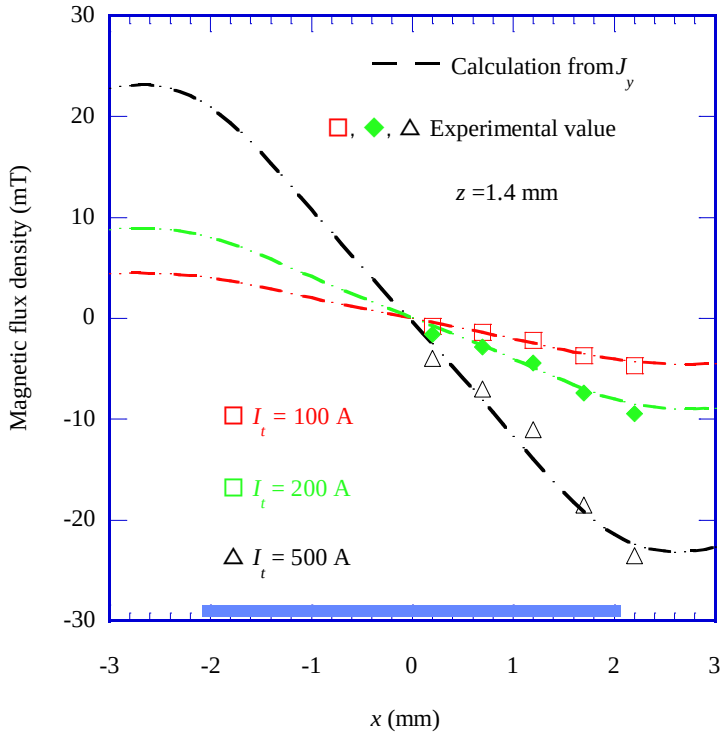


*Figure 3-16: Distributions of magnetic flux density at z = 1.4 mm generated by a CC transporting 100 A, 200 A and 500 A currents. Symbols are experimental results. Dashed lines are calculated from the sheet current densities described in Figure 3-14.*

### 3.5 Summary of Chapter 3

In this chapter, we examined models of total currents, consisting of screening and transport currents, flowing in a short CC. Observations of magnetic flux densities above the center of the CC under an external magnetic field gave a macroscopic view of the screening current flowing one-dimensionally, even in the short CC. The magnetic-field dependencies of macroscopic critical current estimated from transport measurement expressed external magnetic-field dependencies of a screening-current-induced magnetic field (SCF). This result verifies that the screening current corresponds to the critical current. This may be helpful when considering the intensity of the magnetic flux density, the angular dependence of the magnetic field, and the operation temperature in a magnet design.

Assuming that current flows one-dimensionally, we described a model and a solution using the Tikhonov regularization. The distribution of sheet current density was calculated from the distribution of an actual magnetic field. Using the distributions of sheet current density, we calculated magnetic field distributions at different positions, and then compared them to the actual distributions. The calculation and experimental results agreed well and the validity of the model and solution were confirmed. For a low external magnetic field and low transport current, the sheet current density given by the actual magnetic field distributions and Brandt's critical state model agreed well. In Brandt's critical state model, $J_c$ is constant. Therefore, the agreement enhances the validity of the solution of the sheet current density.

# Chapter 4

# Current Distribution in a Single-Coated Conductor in a Background Magnetic Field

Compact high-field magnets require a combination of background (LTS/HTS) coils and YBCO coils, as mentioned in chapter 1. Actual YBCO coils are applied to a self-field and background magnetic field. Accordingly, it is very important to examine the current distribution in YBCO under the magnetic fields. This chapter deals with current distributions in a single-coated conductor under high and low external magnetic fields. The experimental insight of the current distributions becomes very important when designing YBCO magnets.

## 4.1 Procedure for Measuring Magnetic Field Distribution Produced by Screening and Transport Currents

The measurements were performed in liquid helium. Distributions of magnetic flux densities were observed using the No. 1 or No. 2 Hall sensors by the following procedure:

1) The *z*-component magnetic flux densities, $B_z$, with and without a CC under a charging and discharging external magnetic field with magnetic flux densities in the range of 0 T to 5 T were measured in order to evaluate the SCF.
2) The external magnetic field was removed completely.
3) The CCs were heated up to room temperature in order to remove any remnant magnetic fields, and then the CC was cooled to 4.2 K.
4) Transport current $I_t$ was supplied to the CC.
5) A magnetic field with magnetic flux densities ranging between 0 T and 5 T was applied to the CC with a constant $I_t$ of either 50 A, 100 A, 200 A, or 250 A.
6) The differences in $B_z$ ($\Delta B_z$) with and without the CC were calculated from the respective measurements.
7) The Hall sensor was then scanned to the other position and steps 1) – 6) were repeated.

Figure 4-1 shows a schematic overview of this measurement. As described in chapter 3, we assumed that one-dimensional currents flow in the CC.

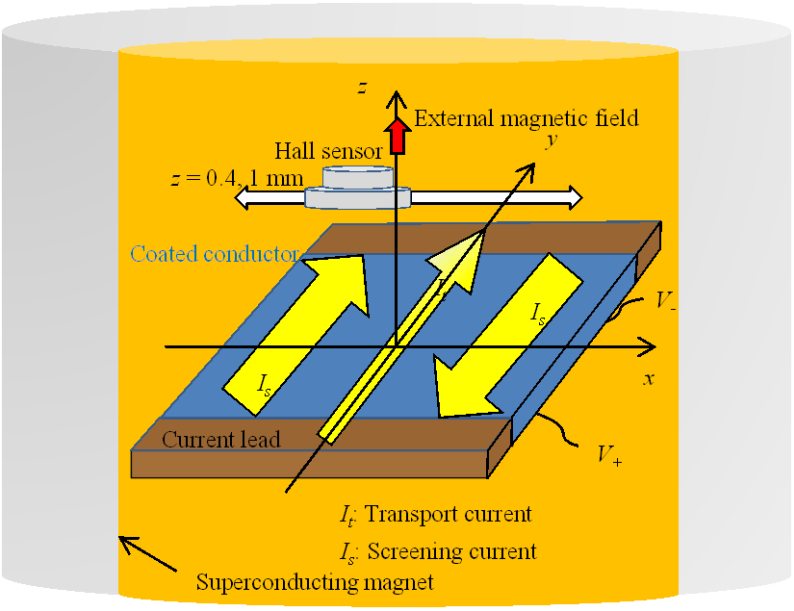


*Figure 4-1: A schematic overview of a measurement of total current distribution consisting of screening and transport currents.*

## 4.2 Current Distribution in a Single Coated Conductor Under a High Field

This section deals with sheet current distributions in a CC placed under a high magnetic field, in which the magnetic flux is at the center of the width of the CC.

Figure 4-2 (a) shows $\Delta B_z$ at position ($x$, $z$) = (0.6 mm, 1 mm) for $I_t$ = 0 A (blue), 50 A (red), 100 A (green) and 200 A (black). The arrows indicate the direction of the varying magnetic field. An increase in the external magnetic field first enhances the SCF, and then reduces it. The hysteresis reveals that magnetic flux exists at the center of the CC under external fields with magnetic flux densities over 0.3 T. As $I_t$ becomes large, the hysteresis of $\Delta B_z$ shrinks, and shifts in the negative direction of $\Delta B_z$. Fig. 4-2 (b) shows $\Delta B_z$ at position ($x$, $z$) = (-0.6 mm, 1 mm) for $I_t$ = 0 A, 50 A, 100 A, and 200 A. The shrinkage values of the hysteresis over the 0.3 T external magnetic field are the same as those at position ($x$, $z$) = (0.6 mm, 1 mm). In other words, the shrinkage of the hysteresis over 0.3 T is symmetric to the width of the CC. This indicates that $I_s$ reduces symmetrically as $I_t$ increases.

Figure 4-3 (a), Figure 4-4 (a) and Figure 4-5 (a) show the distributions of $\Delta B_z$ ($I_t$ = 0 A (blue), 50 A (red), 100 A (green), and 200 A (black)) under an external field with magnetic flux densities of 1 T, 3 T, and 5 T, respectively. The observation height of the Hall sensor was z =1 mm. The symbols represent actual values of $\Delta B_z$. Dashed lines show $\Delta B_z$, calculated from $J_y$, to be solved through inverse problems. The minimum peak positions of $\Delta B_z$ shift in the positive direction of the $x$-axis. As the external magnetic field increases, the shift becomes large. The shift of the position at 5 T is larger than those at 1 T and 3 T. In addition, $I_t$ = 200 A corresponds to 75% and 35% of $I_c$ at 5 T and 1 T, respectively. The differences in the ratios result in the differences in the shifts of the minimum peak positions of $\Delta B_z$. This indicates that if $I_t$ relative to $I_c$ is larger, the generated field will be less symmetric over the width of the CC.

Figure 4-3 (b), Figure 4-4 (b) and Figure 4-5 (b) show the distributions of sheet current densities at 1 T, 3 T, and 5 T, respectively. The value of $J_c$ is the critical sheet current density, which is the critical current over the width of the CC. The critical currents at the respective magnetic fields are described in Figure 3-3. When $I_t$ = 0 A, the screening currents corresponding to a critical current flow in 0.5 mm < $|x|$ < 2.05 mm. An increasingly positive

value of $I_t$ results in an enlargement of the tape cross-section containing a critical current flowing in the $+y$ direction. The steep gradients of $J_y$ seen around $x$, where the direction of $J_y$ reverses, result from the process of solving $J_y$ from the magnetic field distributions.

A further understanding of the relationship between the sheet current distributions and the transport currents is given in Figure 4-6. The sheet current distributions at 1 T and 5 T were normalized at $J_c$ depending on the external magnetic field. In Figure 4-6, the blue circles and green diamonds are $J_y$ relative to $J_c$ under 1 T for $I_t$ = 200 A and 100 A, respectively, which corresponds to $I_t/I_c$ = 0.35 and 0.18. The red squares and black triangles show $J_y$ relative to $J_c$ under 5 T for $I_t$ = 100 A and 50 A, respectively, which corresponds to $I_t/I_c$ = 0.37 and 0.19. The blue and red profiles agree well, as do the green and black profiles. This indicates that the distributions of $J_y$ relative to $J_c$ are determined by $I_t/I_c$. In other words, knowledge of the critical current as a function of the magnetic field enables us to estimate the current distribution in a CC under a high field in which the magnetic flux reaches the center of the width of the CC. In Figure 4-7, $J_y$ relative to $J_c$ is unified with respect to $I_t/I_c$. As the value of $I_t/I_c$ increases, the regions of sheet current density with $J_c$ expand.

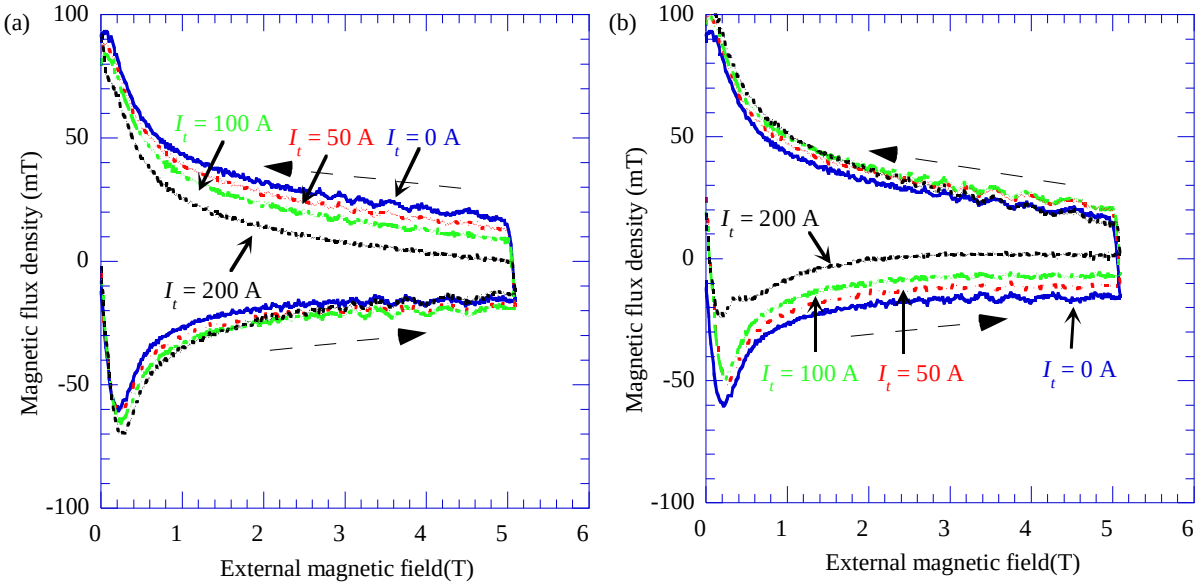


*Figure 4-2: (a) Magnetic flux density at position (x, z) = (0.6 mm, 1 mm) for $I_t$ = 0 A (blue), 50 A (red), 100 A (green), and 200 A (black). (b) Magnetic flux density at position (x, z) = (-0.6 mm, 1 mm) for $I_t$ = 0 A (blue), 50 A (red), 100 A (green) and 200 A (black). Two arrows show the direction of the varying magnetic field.*

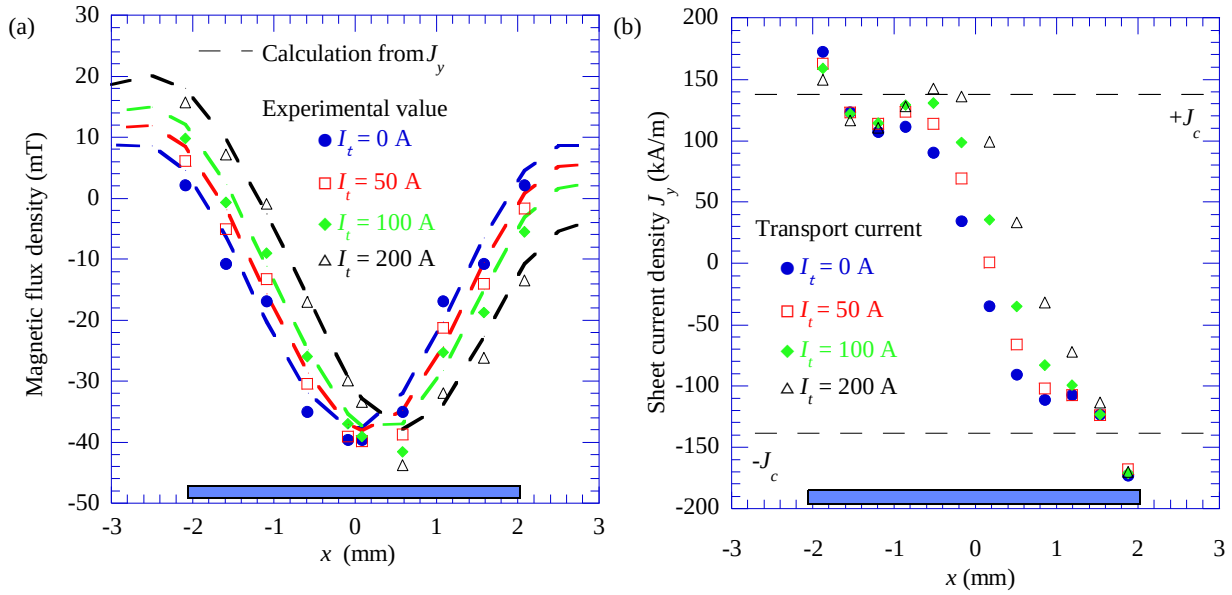


*Figure 4-3: (a) Distributions of magnetic flux densities ($I_t$ = 0 A (blue), 50 A (red), 100 A (green), and 200 A (black)) under an external field with a magnetic flux density of 1 T. The observation height was z = 1 mm. (b) Distributions of sheet current densities at 1 T estimated from (a).*

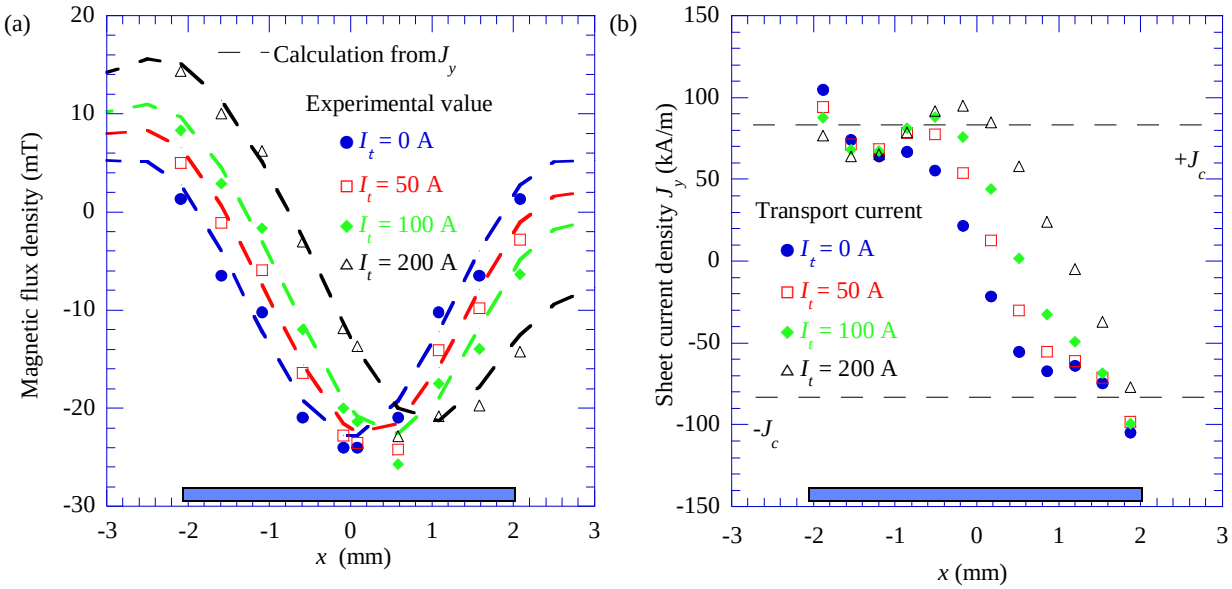


*Figure 4-4: (a) Distributions of magnetic flux densities ($I_t$ = 0 A (blue), 50 A (red), 100 A (green), and 200 A (black)) under an external field with a magnetic flux density of 3 T. The observation height was z = 1 mm. (b) Distributions of sheet current densities at 3 T estimated from (a).*

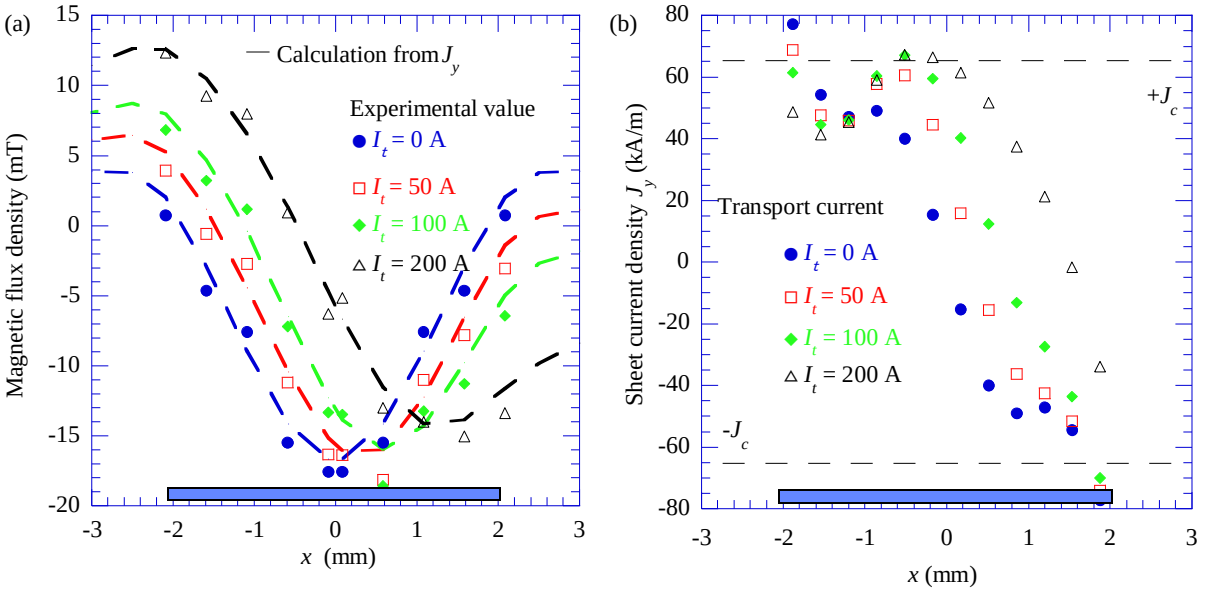


*Figure 4-5: (a) Distributions of magnetic flux densities ($I_t$ = 0 A (blue), 50 A (red), 100 A (green), and 200 A (black)) under an external field with a magnetic flux density of 5 T. The observation height was z = 1 mm. (b) Distributions of sheet current densities at 5 T estimated from the (a).*

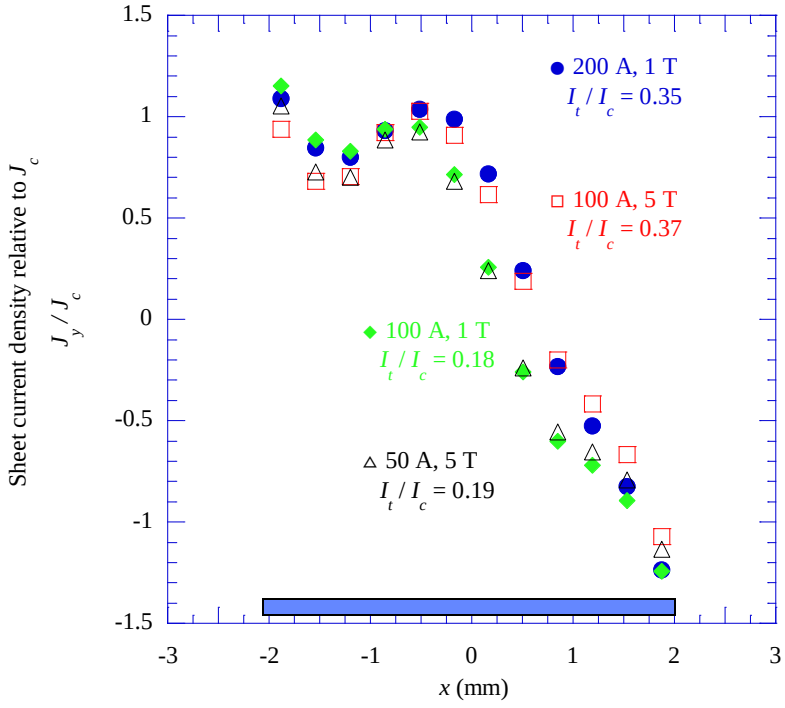


*Figure 4-6: Profiles of $J_y$ relative to $J_c$ under an external magnetic field. The blue circles and green diamonds show $J_y$ relative to $J_c$ under 1 T for $I_t$ = 200 A, and 100 A, respectively, which corresponds to $I_t/I_c$ = 0.35 and 0.18. The red squares and black triangles show $J_y$ relative to $J_c$ under 5 T for $I_t$ = 100 A and 50 A, respectively, which corresponds to $I_t/I_c$ = 0.37 and 0.19.*

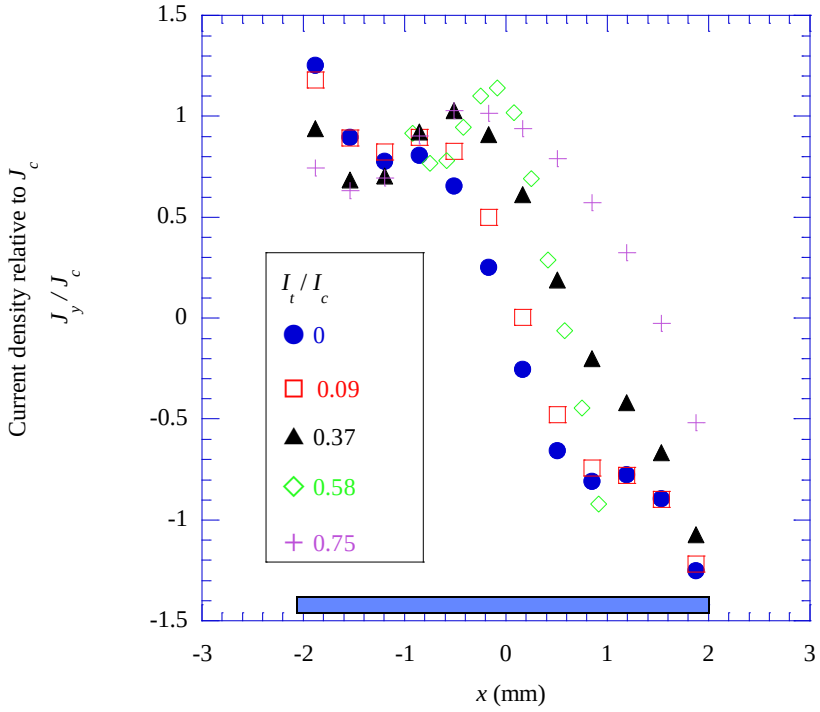


*Figure 4-7: Profiles of $J_y$ relative to $J_c$ unified by the value of $I_t/I_c$.*

### 4.3 Current Distribution in a Single Coated Conductor Under a Low Field

This section discusses sheet current distributions in a CC placed under a low magnetic field, in which the magnetic flux is not at the center of the width of the CC.

Figure 4-8 shows the distributions of the magnetic flux densities produced by screening and/or transport currents flowing in a CC under 0.1 T. The observation height using the No.2 Hall sensor was 0.4 mm. The blue circles show the distributions of the SCF. The red, green, and black profiles describe the distributions for $I_t$ = 100 A, 200 A, and 250 A, respectively. The magnetic flux densities near the center of the CC do not depend on the transport current. Under an external field with a magnetic flux density of 0.1 T, the critical current is very high when compared to $I_t$. However, the self-field generated by the transport current is small relative to the external field. It is considered that the external magnetic field is more dominant over the variations of the distributions of the magnetic flux densities than is the transport current. In addition, the absolute values of the magnetic flux densities at the center do not exceed the intensity of the external magnetic field.

Figure 4-9 shows the distributions of sheet current density calculated from the distributions of Figure 4-8. The sheet current densities are high near the edges of the CC. Variations in sheet current densities concerning transport currents are small inside the CC and the magnetic field distributions, as shown in Figure 4-8. Figure 4-9 describes the sheet current densities in a CC with transport currents under 0.05 T. Considering the differences between Figure 4-9 and 4-10, the variations in the external magnetic field are more dominant over current distributions in the CC under a low magnetic field than over those of the self-field generated by the transport currents. The dominance of external magnetic fields shows the same tendency as Brandt's model [85].

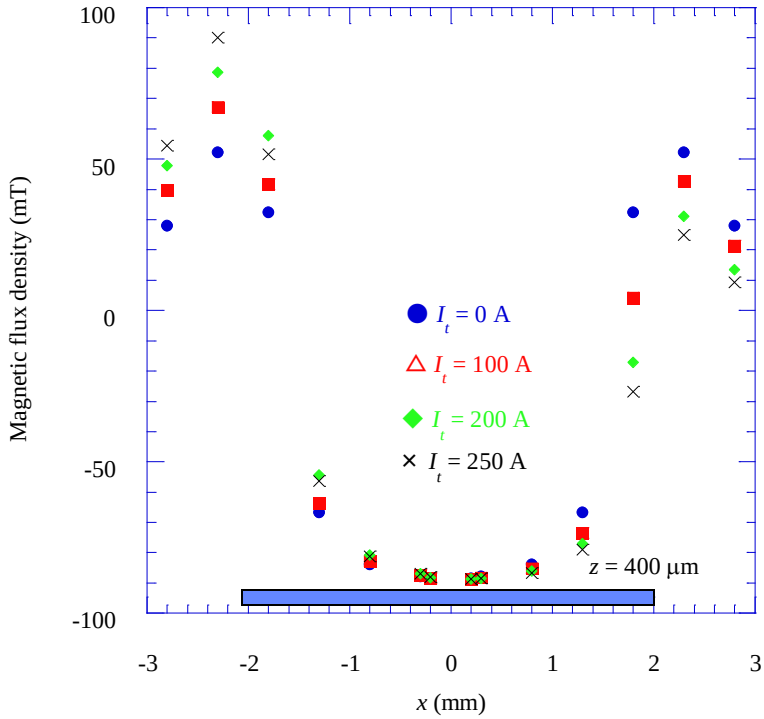


*Figure 4-8: Distributions of magnetic flux densities ($I_t$ = 0 A (blue), 100 A (red), 200 A (green), and 250 A (black)) under an external field with a magnetic flux density of 0.1 T.*

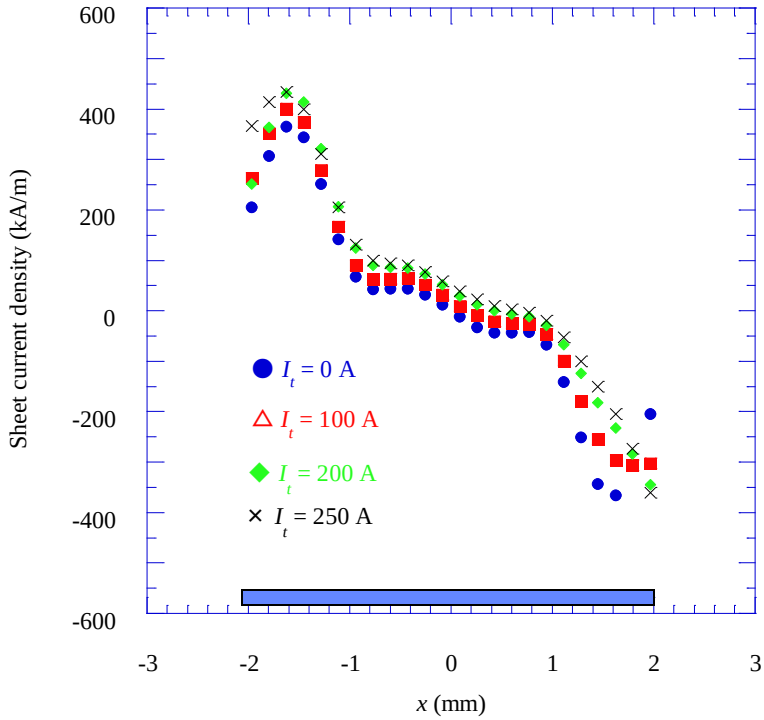


*Figure 4-9: Distributions of sheet current densities under 0.1 T, estimated from the distributions of Figure 4-8.*

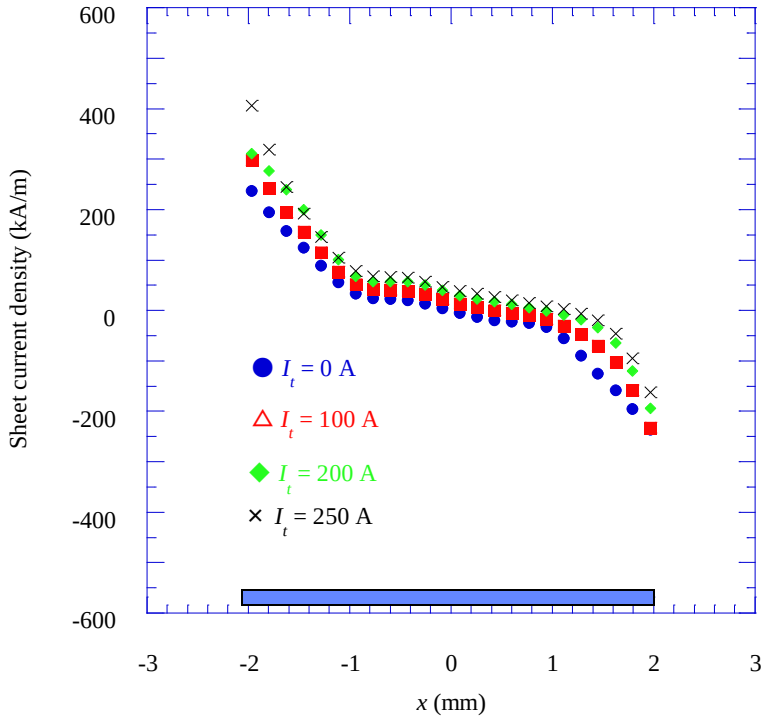


*Figure 4-10: Distributions of sheet current densities under 0.05 T, estimated from the distributions of the magnetic flux densities.*

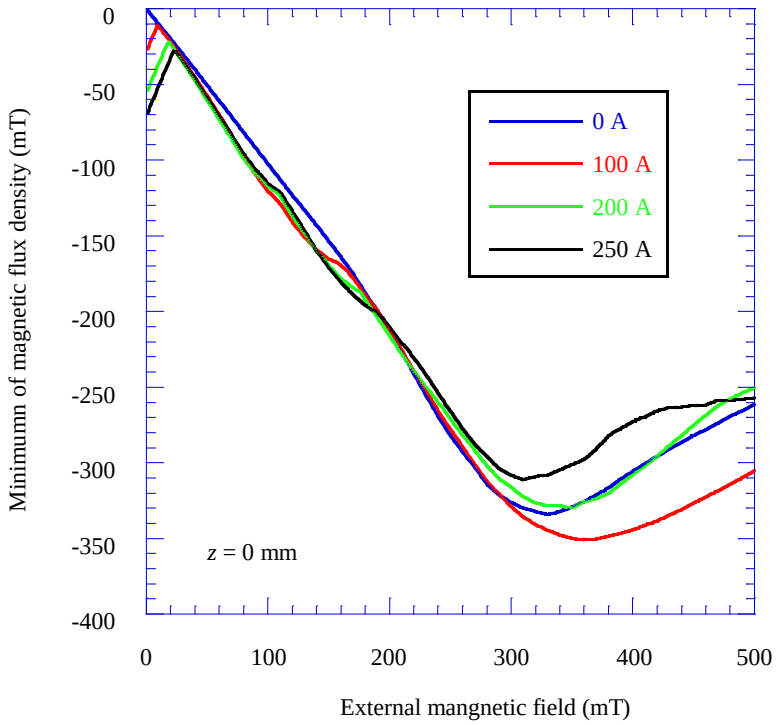


*Figure 4-11: The Minimum magnetic flux density at z = 0 mm, estimated from the current distributions as functions of the external magnetic field.*

Figure 4-11 shows that the minimum magnetic flux density at $z$ = 0 mm, that is, the surface of the superconducting layer of the CC, estimated from the current distributions as functions of the external magnetic field. The magnetic flux densities at 0 mT are due to transport currents. Magnetic flux densities were estimated at 0.1 mm intervals. The positions of CCs with transport currents, in which magnetic flux densities become lowest, vary from external magnetic field to external magnetic field. The discretized positions cause ripples in the profiles for 100 A, 200 A, and 250 A. From 30 mT to 280 mT, all the minimum values of magnetic flux densities decrease linearly, and are superimposed. The gradient is approximately -1. In other words, the minimum magnetic flux density is a magnetic flux density with an external magnetic field. Above 280 mT, the profiles are lowest in an external magnetic field in which the magnetic flux increases to more than the width of a CC.

## 4.4 **Summary of Chapter 4**

This chapter deals with sheet current distributions in a single CC with a transport current under an external magnetic field. The differences between sheet current distributions are discussed in two sections.

Section 4.2 discusses the sheet current density in a CC under an external magnetic field in which the magnetic flux is high enough to be at the center of the CC. It transpired that the transport current relative to critical current determines the distribution of the sheet current density under a high field, depending on the external magnetic field.

Section 4.3 discusses the sheet current density under a low magnetic field, in which the magnetic flux is not at the center of the CC. The section reveals that variations in the external magnetic field are dominant over the distributions of the sheet current density under a low magnetic field. The minimum magnetic flux density on the surface of a CC is equal to the magnetic flux density with an external magnetic field in the region where the external magnetic field is dominant.

# Chapter 5

# Magnetic Field Distribution Generated by Multiple Coated Conductors

Superconducting coils have number of layers and turns of superconducting wires. Therefore, in electromagnetic designs of YBCO coils, we need to examine interactions of screening current in multiple CCs. This chapter deals with distributions of a magnetic field produced by the following multiple YBCO coated conductors: superimposed CCs, arranged-CCs, and arranged-and –superimposed CCs. This thesis targets a design method of a YBCO pancake coil. The pancake coil is wound with a CC concentrically. Then, a superconducting magnet is composed of the pancake coils superimposed concentrically.

## 5.1 Screening-current-induced Field Generated by Superimposed Coated Conductors

This section discusses magnetic field distribution produced by superimposed CCs cut into short lengths simulated a single-pancake coil. In particular, this section deals with interaction between CCs exposed to a considerably high magnetic field up to 18 T.

### 5.1.1 Procedures for measuring screening-current-induced field generated by superimposed Coated conductors

CCs were cut into short specimens with lengths of 20 mm. The CCs were insulated using polyimide tapes. The thickness $t$ of CCs including the insulation was 0.33 mm. The CCs were superimposed each other, as shown in Figure 5-1 (a). They were attached on FRP jigs. Then, the CCs were inserted into the bore of a superconducting magnet attaching to the No.1 cryostat, which was used to apply an external field to the CCs. External fields varying from 0 T to 18 T and 18 T to 0 T were applied. The rates of charging and discharging magnetic fields of 0 T to 15 T and 15 T to 18 T were ±14.4 mT/s and ±7.2 mT/s, respectively. In the superconducting magnet, the ramp rates are highest in the respective ranges. The CCs were cooled down using liquid helium. The tape surface of $z = 0$ was defined as an outer surface of cupper layer deposited on a substrate of a top CC. In the experiments, fields ($B_z$) in a direction of $z$ axis at a position of ($x$, $y$, $z$) = (0, 0, 2 mm) were measured with the No.1 Hall sensor, as shown in Figure 5-1 (b).

SCFs were evaluated with the following procedure:

1) Measurement of magnetic fields with and without CCs under charging and discharging external fields.
2) Subtraction of the values of magnetic field without CCs from those of magnetic fields with CCs under charging and discharging external fields.
3) Definition of SCFs as half of differences between the measured fields at the same external fields under charging and discharging.

The SCFs do not include magnetization of paramagnetic materials under a high field.

(a)

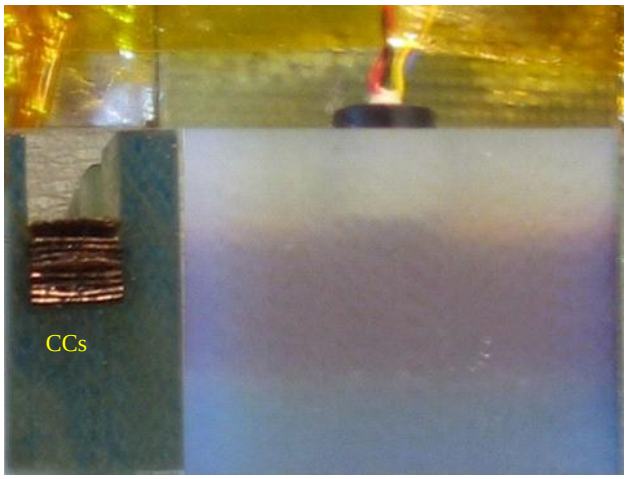


(b)

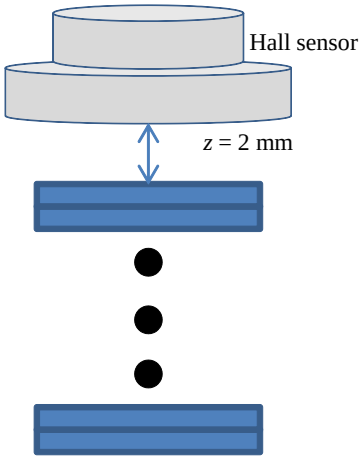


*Figure 5-1: (a) CCs superimposed on each other for the measurement, (b) Geometry of the Hall sensor and CCs.*

### 5.1.2 Results and discussion

Figure 5-2 shows SCFs at the position ($x$, $y$, $z$) = (0, 0, 2 mm) for superimposed CCs under varying external fields from 0.5 T to 18 T, in which magnetic flux exists in the entire widths of the CCs. Four kinds of symbols show experimental data. As an external magnetic field decreases, the absolute values of SCFs become small depending on magnetic-field dependence of critical the current density of the CCs. The ripples of SCF under high magnetic fields are caused by magnetic quantum oscillation occurring in the Hall sensor. The three kinds of lines are values of SCFs estimated from a SCF for a single CC based on the symmetric current model in Figure 3-5. The SCFs produced by the superimposed CCs are given by

$$B_z = \frac{\mu_0 I}{\pi a}\sum_{k=1}^{n}\log\frac{\sqrt{a^2+\{2+t(k-1)\}^2}}{2+t(k-1)} \qquad (5.1.1)$$

where $I$ is screening current, $a$ is a half width of a CC and $n$ is the number of CCs. The SCF for a single CC was described well using the current model in section 3.2.3. Interestingly, the lines and measurement results agree well, especially under high magnetic fields. This indicates that the superimposed CCs under a high magnetic field have same current distributions and the interaction between SCFs generated by the CCs is negligible.

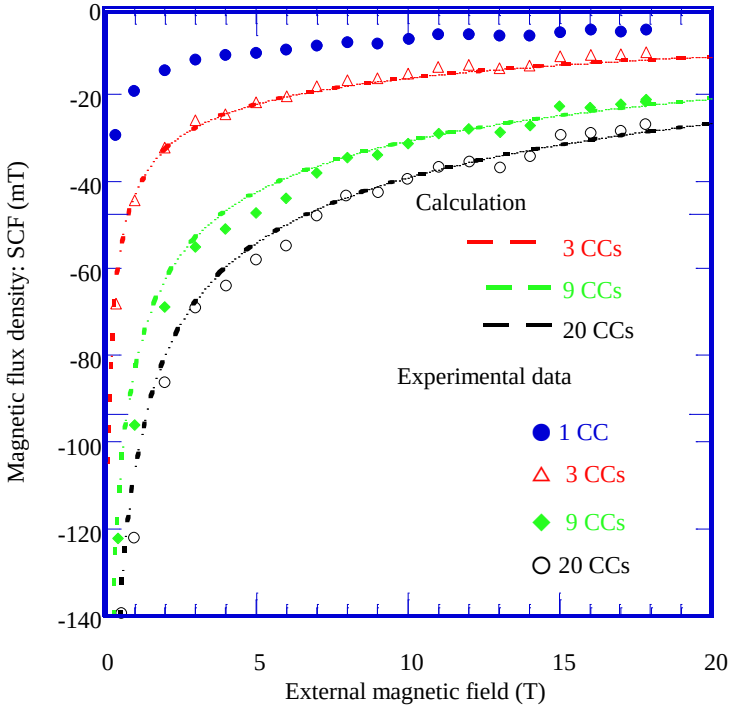


*Figure 5-2: SCFs at the position of z = 2mm for the superimposed CCs under varying an external magnetic field. Four kinds of symbols show experimental data for SCFs. (Blue filled circles: 1 CC, Red open squares: 3 CCs, Green filled diamonds: 9CCs and Black open circles: 20 CCs) The dashed lines are calculation results base on the symmetric current model.*

## 5.2 Distributions of Screening-current-induced Field Generated by Arranged and/or Superimposed Coated Conductors

This section presents distributions of SCF generated by arranged- and/or superimposed CCs. This section expands an understanding of SCF for superimposed CCs stated in section 5.1. The configurations simulate cross-sections of multi-pancake coils.

### 5.2.1 Procedures of measuring screening-current-induced field generated by arranged and/or superimposed coated conductors

CCs were cut into short specimens with lengths of 20 mm. The CCs were not insulated. The CCs were arranged in a few rows and/or superimposed, as shown in Figure 5-3 (a). The CCs were attached to FRP jigs. In Figure 5-3 (b), the four female screws inserted in the FRP jig got fixed the other jig and a Hall sensor. The No. 2 Hall sensor was used in this measurement. Figure 5-3 (b) shows an actual photograph of a FRP jig and three YBCO CCs arranged in a row. The Hall sensor was attached on the top surface of the CCs and scanned along the $x$ axis, as shown in Figure 5-2. The top surface of the superconducting layer of CCs was defined as $z$ = 0 mm. The observation height was at $z$ = 0.4 mm. The CCs were inserted into the bore of a superconducting magnet attached to the No.1 cryostat, which was used to apply an external field to the CCs. External fields from 0 T to 5 T and 5 T to 0 T were applied. The rates of charging and discharging magnetic fields of 0 T to 5 T was ±14.4 mT/s. The rates are highest in the ranges of external magnetic fields. The CCs were cooled down using liquid helium. The $z$-components of magnetic flux densities were observed during increase and decrease of an external magnetic field. The experimental values were subtracted from the external magnetic field and the values $\Delta B_z$ were regarded as SCFs. It is assumed that distribution of SCFs is symmetric to the $x$ = 0 mm in this measurement.

### 5.2.2 SCFs generated by the arranged and/or superimposed coated conductors

Figure 5-4 shows $\Delta B_z$ at a position ($x$, $z$) = (0.2 mm, 0.4 mm) generated by the four kinds of arranged and/or superimposed CCs under varying external magnetic field. As an external magnetic field increases, the values of $\Delta B_z$ decrease linearly and reaches bottom at a peak field, where magnetic flux reaches the centers of the CCs. The gradients of $\Delta B_z$ relative to an external magnetic field between 0 T and the peak field are constant regardless of the numbers of CCs. In addition, the values of the peak fields do not depend on the numbers of the CCs arranged but the numbers of the CCs superimposed. The values of $\Delta B_z$ increase according to magnetic-field dependence of critical current densities under an external magnetic field more than the peak field. When an external magnetic field decreases from 5 T, the values of $\Delta B_z$ increase with the same gradients as that during initial charge from 0 T to the peak field. The more the numbers of CCs arranged in a row and the smaller the numbers of the superimposed CCs, the smaller the hysteresis of $\Delta B_z$ becomes.

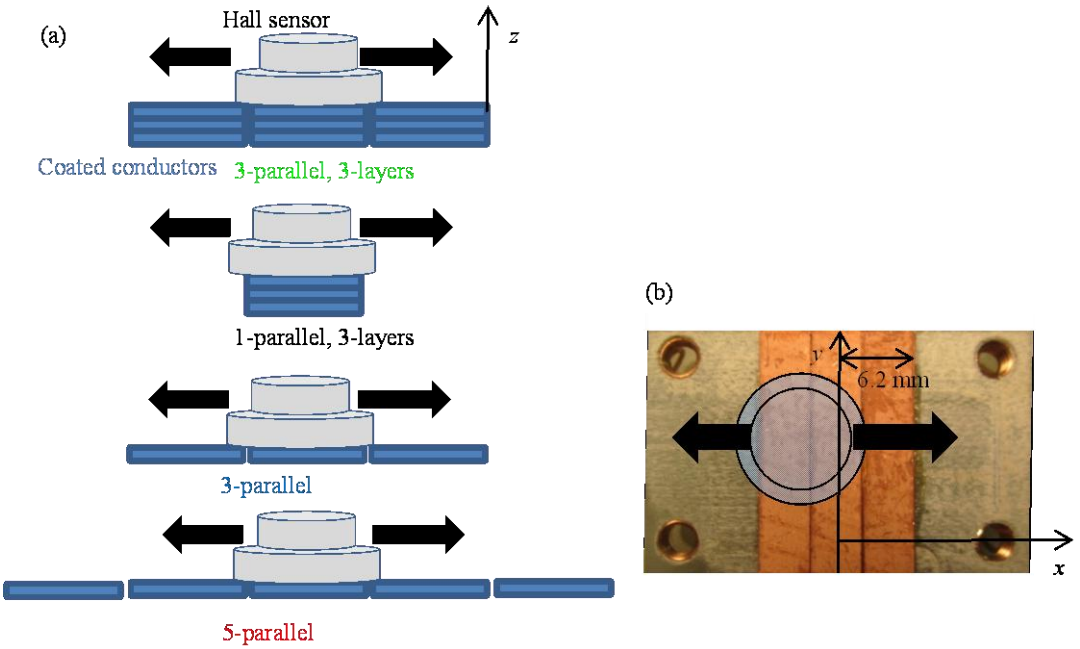


*Figure 5-3: (a) Arranged and/or Superimposed Coated Conductors used in the measurement. (b) An actual photograph of a FRP jig and three YBCO CCs arranged in a row.*

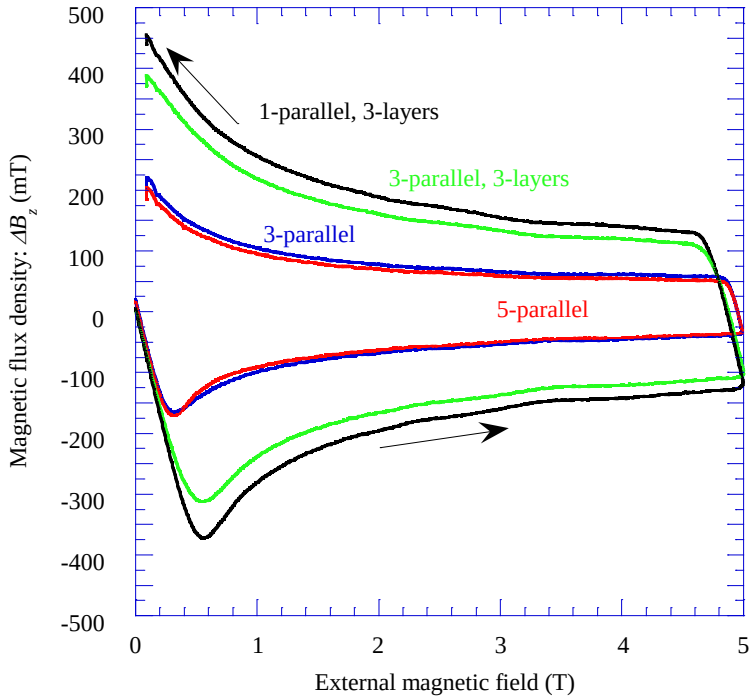


*Figure 5-4: $\Delta B_z$ at a position (x, z) = (0.2 mm, 0.4 mm) generated by the four kinds of arranged and/or superimposed CCs under varying external magnetic field.*

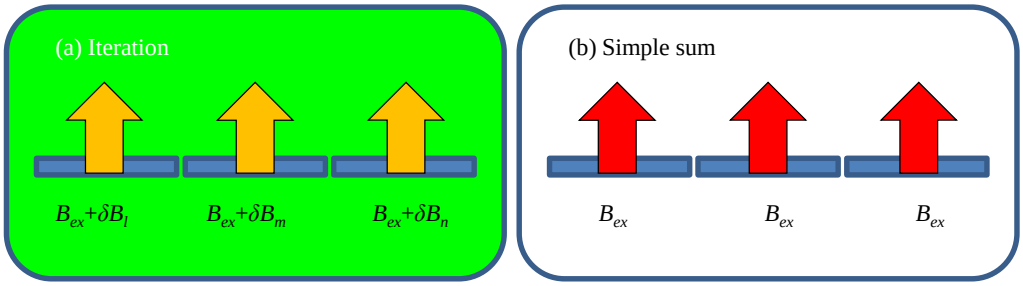


*Figure 5-5: A schematic view of the iteration method and simple sum method.*

#### 5.2.2.1 Calculation of SCFs using a sheet current distribution in a single CC under high magnetic field

A calculation method for estimating SCFs generated by multiple CCs was studied. In chapter 4, sheet current distributions in a single CC were estimated. In the calculation method for SCFs, the sheet current densities in the single CC were used. The calculations were employed to estimate SCFs for high external magnetic field where magnetic flux is at the center of the CC. They were carried out as follows (Figure 5-5):

1) External magnetic field with constant magnetic flux $B_{ex}$ density is applied to multiple CCs.
2) The sheet current densities in the CCs are determined by the given magnetic flux density.
3) Magnetic flux densities $dB$ on the surface of the CCs are calculated from the sheet current densities in the CCs.
4) Average of magnetic flux density $B_{ex}+\delta B_{av}$ on the surface of the CCs gives the sheet current densities of the each CC.
5) Step 1)-4) are repeated once.

In Figure 5-5, schematic views of the iteration method and simple sum method, in which calculation stops just after the step 2), are illustrated.

#### 5.2.2.2 Distributions of SCF generated by the arranged and/or superimposed coated conductors

Figure 5-6 shows distribution of SCF for 3-parallel CCs under an external field with magnetic flux of 1 T. The blue circles show experimental values. Three curves being convex downward locate at the center of the widths of CCs. The upward peak positions show the edges of the CCs. Green and red lines were calculated using the iteration and the simple sum method, respectively. On the whole, the green and red lines are superposed over the width. This indicates that interaction between screening currents in CCs arranged in a row is very small. Absolute values of $\Delta B_z$ at the peak position calculated using the iteration method are smaller than those calculated using the simple sum method. The smaller values estimated using the iteration method describe that the CCs lay side by side increase an magnetic field exposed to each CC. Disagreement near $x = \pm 6$ mm between the experimental data and the calculation results are caused by the reduction of the critical current density at the edge of the CC. Figure 5-7 shows distribution of SCF for 5-parallel CCs at an external field with magnetic flux of 1 T. The blue circles show experimental values. The green and red lines were calculated using the iteration and the simple sum method, respectively. CCs are placed on the position $-10.25$ mm $< x <$ 10.25 mm. The green line agrees better with the experimental result. Figure 5-8 shows distribution of SCF for 3-layers CCs under an external magnetic field with magnetic flux of 1 T. In contrast with Figure 5-6 and Figure 5-7, the absolute value of $\Delta B_z$ at the peak position in the green line is larger than that in the red line. This is because the superimposed CCs reduce an external magnetic

field each other. Distances between each CC in the 3-layers CCs are 0.1 mm. Compared with section 5.1, interaction between CCs is large. In Figure 5-9, distribution of SCF for 3-parallel, 3-layers CCs at 1 T are described. The difference between results estimated from the iteration and the simple sum methods is larger than those of SCF for the CCs arranged only in a row. Calculation results using the iteration method agree well with the experimental values. Figure 5-10 shows distributions of a magnetic field generated by transport and screening currents flowing in 3-parallel, 3-layers CCs. The distributions show the magnetic-field distribution 0.4 mm above top layer of the CCs. The distributions were calculated using the iteration method. In this calculation, it was assumed that transport currents with same intensity were supplied to all the nine CCs. The blue, red, and green lines are the distributions for the transport current: 0 A, 100 A, and 200 A, respectively. As transport currents increase, the values of $\Delta B_z$ in region $x < 0$ mm decrease.

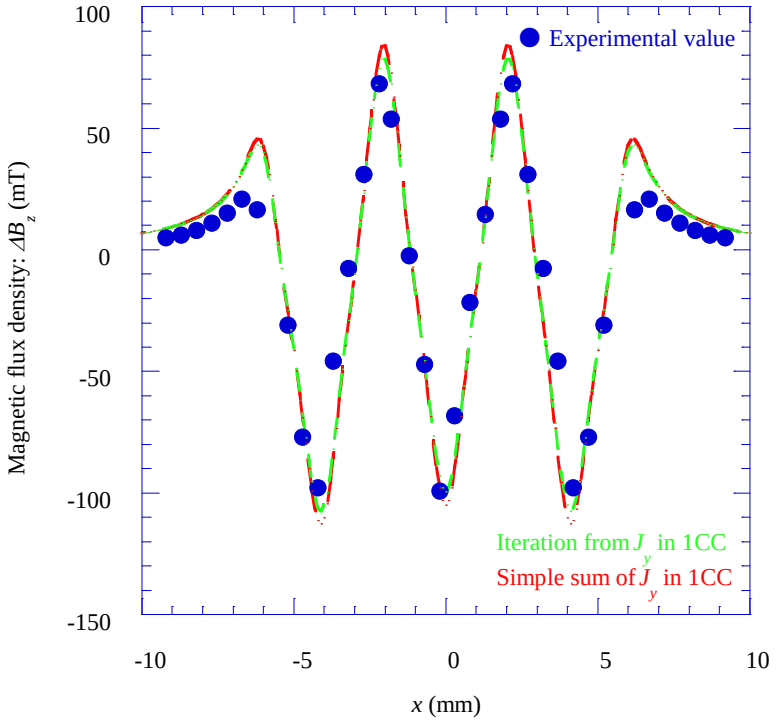


*Figure 5-6: Distribution of SCF for 3-parallel CCs under an external field with magnetic flux of 1 T. The blue circles show experimental values. Green and red lines were calculated using the iteration and the simple sum methods, respectively.*

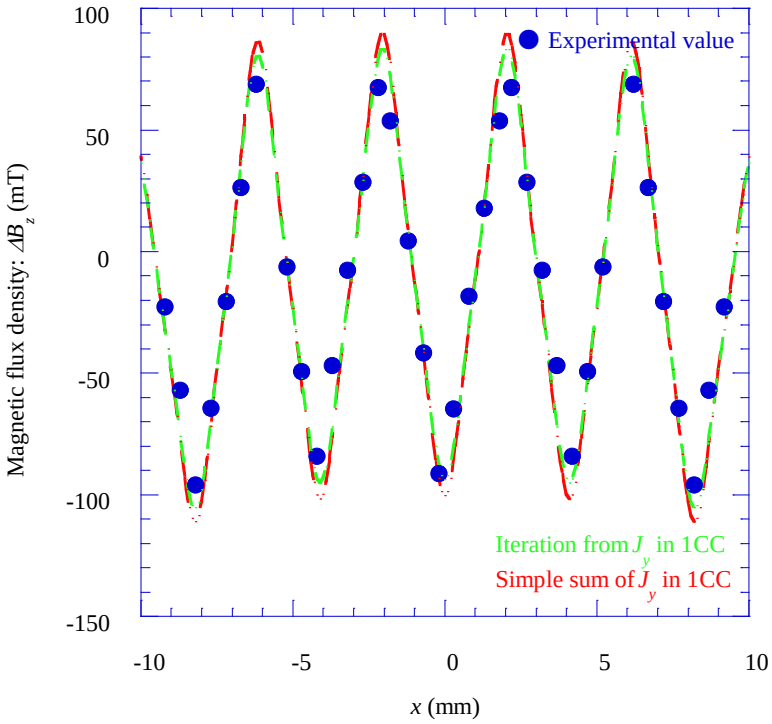


*Figure 5-7: Distribution of SCF for 5-parallel CCs under an external field with magnetic flux of 1 T. The blue circles show experimental values. Green and red lines were calculated using the iteration and the simple sum method, respectively.*

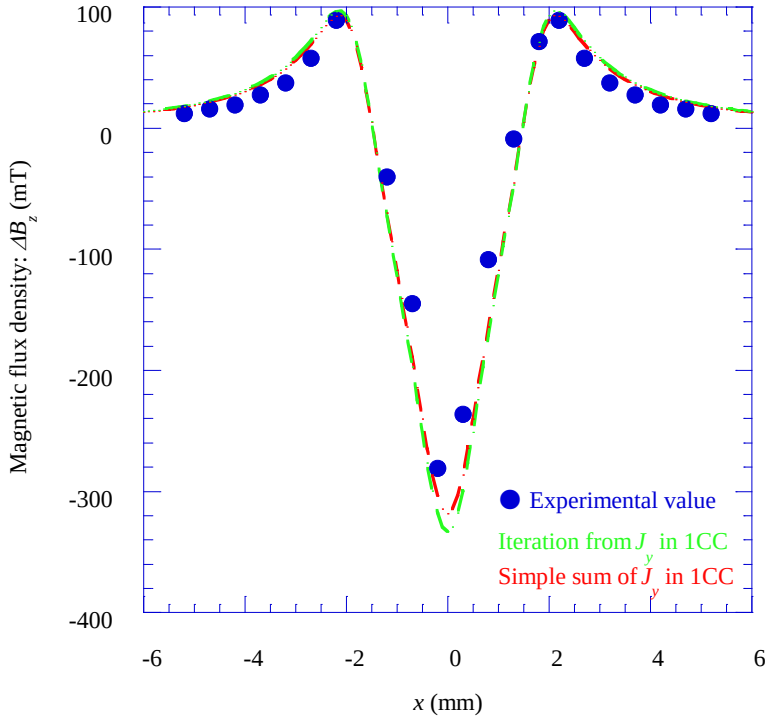


*Figure 5-8: Distribution of SCF for 3-layers CCs under an external field with magnetic flux of 1 T. The blue circles show experimental values. Green and red lines were calculated using the iteration and the simple sum method, respectively.*

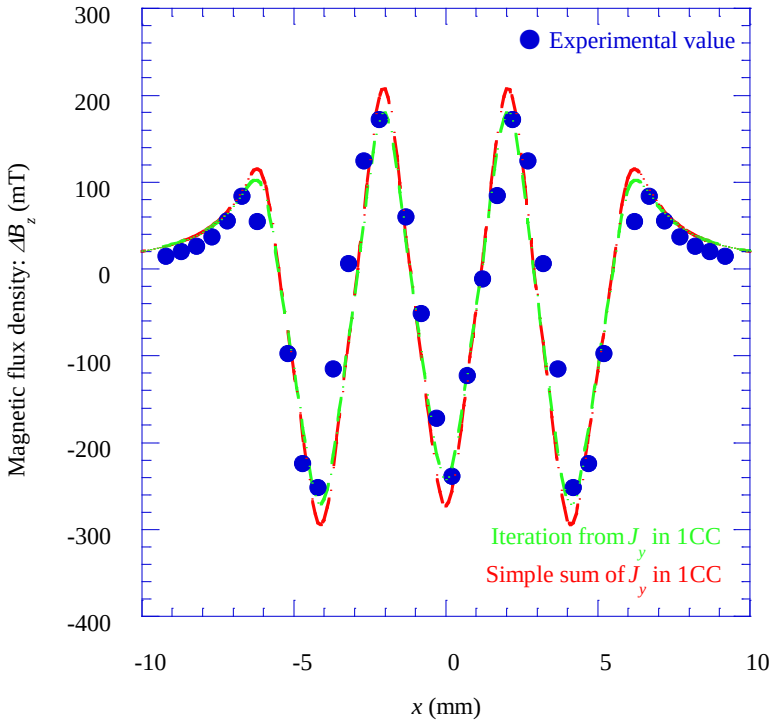


*Figure 5-9: Distribution of SCF for 3-parallel, 3-layers CCs under an external field with magnetic flux of 1 T. The blue circles show experimental values. Green and red lines were calculated using the iteration and the simple sum method, respectively.*

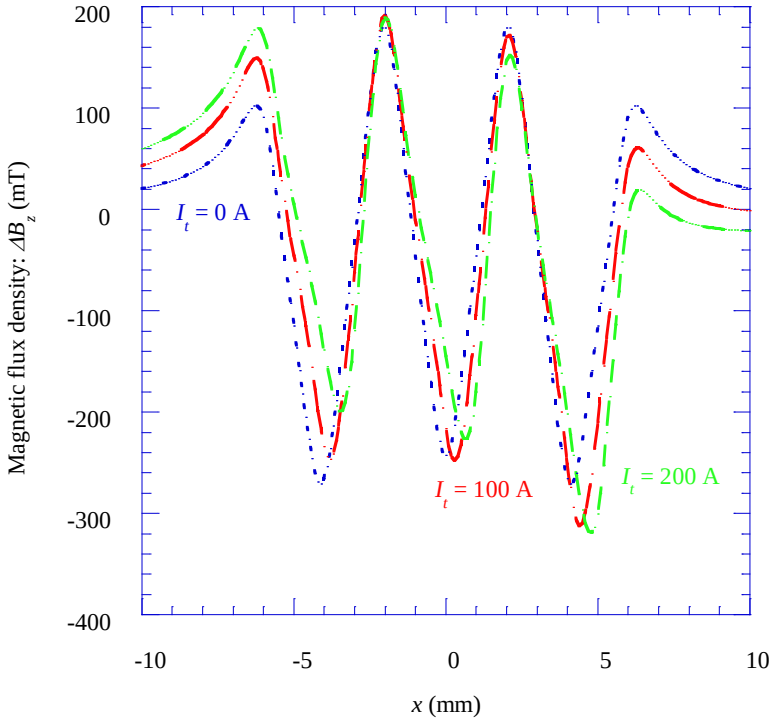


*Figure 5-10: Distribution of a magnetic field generated by transport and screening currents flowing in 3-parallel, 3-layers CCs under an external field with magnetic flux of 1 T. The distributions were calculated using the iteration method. The blue, red, and green lines show the distribution for transport current: 0 A, 100 A, and 200 A, respectively.*

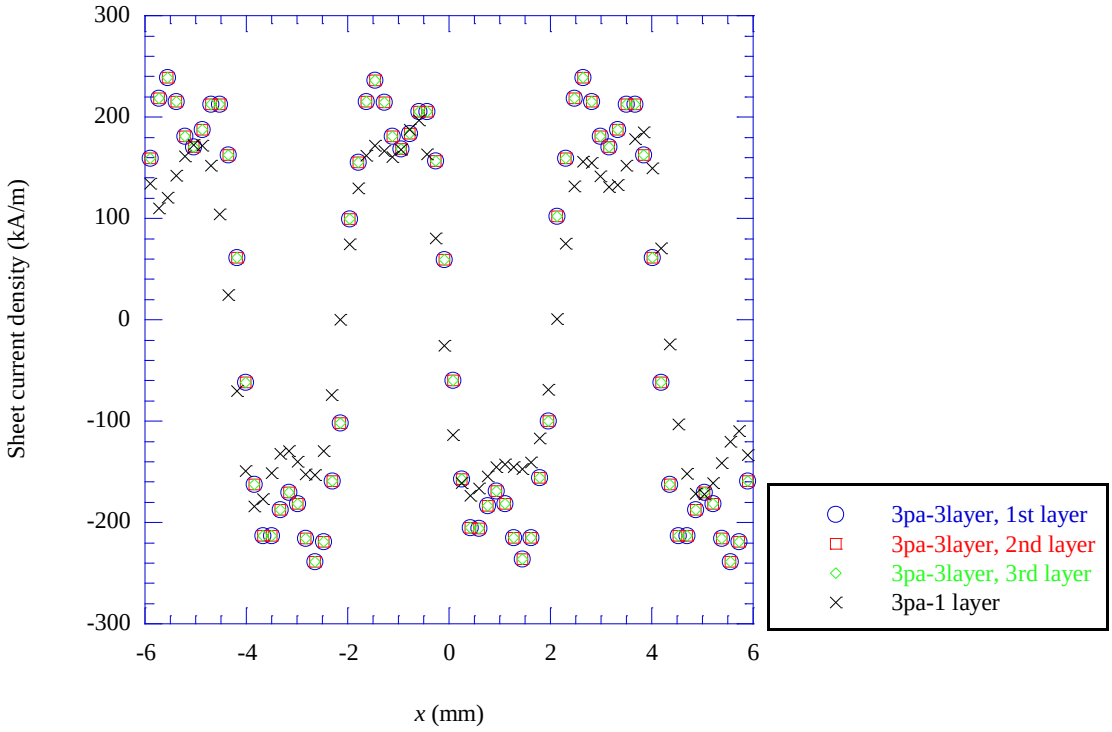


*Figure 5-11: Sheet current densities in arranged and/or superimposed CCs under magnetic field of 1 T. The blue, red and green profiles show sheet current densities in 3-parallel, 3-layers CCs and in the bottom layer, middle layer and top layer, respectively. The black cross was estimated from the distributions of experimental values through the inverse problem.*

### 5.3 Distributions of Sheet Current Densities in Arranged and/or Superimposed Coated Conductors

Figure 5-11 shows sheet current densities in CCs under magnetic field of 1 T. The blue, red and green profiles show sheet current densities in 3-parallel, 3-layers CCs and in the bottom layer, middle layer and top layer, respectively. The black cross was estimated from the distributions of experimental values through the inverse problem. Sheet current densities in the three layers fit closely. The agreement bears out the indication in section 5.1.3. It is considered that enhancement of sheet current densities in 3-layers CCs result from interactions of screening current in the surrounding CCs. Clem *et al.* suggested a calculation model to simplify AC losses of superimposed thin superconductors [100]. In this model, same amount of magnetic flux goes in each thin superconductor. In other words, same screening current flows in each conductor. These experimental results for thin 3-layers CCs agree well with the Clem model.

### 5.4 Summary of Chapter 5

This chapter presents screening-current-induced field (SCF) generated by multiple CCs under high field, where magnetic flux is at the center of the CC. Distributions of SCF generated by the arranged and/or superimposed CCs are examined and then the calculation method for estimating the distributions from sheet current densities in a single CC is suggested. The calculation results give the accordance with the experimental values. The sheet current densities estimated in the calculation process gives an insight that the superimposed CCs have the same sheet current densities. This result is effective to make calculation duration of SCF short.

# Chapter 6

# Temporal Variations of Magnetic Field Generated by Screening Current

Superconducting magnets are expected to generate a highly stable magnetic field. This chapter presents temporal stability of SCFs generated by multiple CCs. As stated in section 1.5.4, current flowing in superconductors dissipates proportionally to logarithm of time due to flux creep. The rate of dissipating depends on temperature and magnetic field. This chapter discusses interaction of temporary variations of SCF.

## 6.1 Procedure for Measuring Temporary Variations of Magnetic Field Generated by Screening Current

Temporal variations of remnant magnetic field, which is a magnetic field trapped by CCs after removing background magnetic field completely, were measured. The CCs were cut into the lengths of 20 mm. The following three measurements were carried out.

(A) Temperature dependences of temporal variations of SCFs generated by a single CC.

1) A CC was cooled down using liquid helium and helium gas in bores of the No.1 and the No.2 cryostats, respectively.
2) A superconducting magnet was energized up to 18 T, and then external magnetic field was removed completely.
3) A measurement using the No. 1 Hall sensor started at instant when the external magnetic field reduced to 0 T. Magnetic flux density was observed at the position 2 mm above the center of the CC.
4) Step 1) – 3) were repeated at 4.2 K, 20 K and 30 K.

(B) Temporal variations of SCFs generated by superimposed CCs.

1) Superimposed CCs were cooled down using liquid helium in bores of the No.1 cryostat.
2) A superconducting magnet was energized up to 18 T, and then external magnetic field was removed completely.
3) A measurement using the No. 1 Hall sensor started at instant when the external magnetic field reduced to 0 T. Magnetic flux density was observed at the position 2 mm above the center of the top CC.
4) Step 1) – 3) were repeated regarding three, nine and twenty CCs superimposed.

(C) Temporal variations of SCFs generated by arranged and superimposed CCs.

1) Arranged and/or superimposed CCs were cooled down using liquid helium in bores of the No.1 cryostat.
2) A superconducting magnet was energized up to 5 T, and then external magnetic field was removed completely.
3) A measurement using the No. 2 Hall sensor started at instant when the external magnetic field reduced to 0 T. Magnetic flux density was observed at the position 0.4 mm above the center of the CC. The No.2 Hall sensor was measured at seven positions at the same time.
4) Step 1) – 3) were repeated for 3-parallel-3-layers CCs, 3-parallel CCs, and 5-parallel CCs.

## 6.2 Results and Discussion

Figure 6-1 shows a temporal variation of remnant magnetic field at $z$ = 2 mm induced by screening current in a single CC at 4.2 K. The blue profile shows an experimental result. The red line is a curve approximated by (6.2.1).

$$B_z(t) = A\left(1 - \frac{U_0^*}{k_B T}\log(Ct+1)\right) + D\exp(Et) \tag{6.2.1}$$

where $A$, $C$, $D$, $E$ are fitting parameters. The first term is derived from flux creep. The second term shows decay of current induced in normal conductors. CCs have metallic conductors, such as copper stabilizer and silver layer. The green line is a curve drawn only by the first term of (6.2.1). These lines are superposed at $t$ = 100 s. Therefore, temporal variations of the magnetic field after $t$ = 100 s are regarded as a decay due to flux creep.

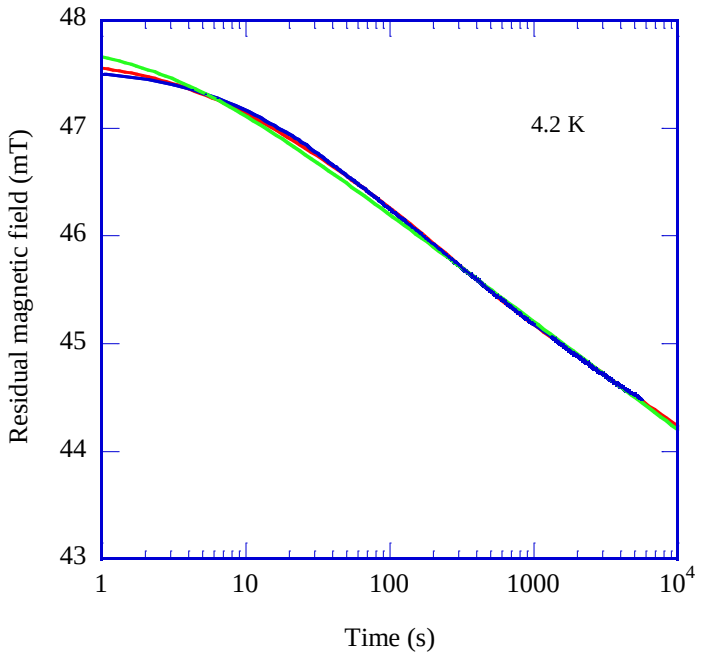


*Figure 6-1: A temporal variation of remnant magnetic field at z = 2 mm induced by screening current in a single CC at 4.2 K. The blue, red and green lines show an experimental result, curves approximated using (6.2.1) and only the first term of (6.2.1), respectively.*

(A) Temperature dependences of temporal variations of SCFs generated by a single CC

Figure 6-2 (a) shows temperature dependences of temporal variations of SCFs at a position of $z$ = 2 mm for a CC, and Figure (b) shows those normalized by the values at $t$ = 100 s. The drifts between $t$ = 0 s and 100 s are governed by decays of currents induced by discharging external magnetic fields. According to [30], the drifts at $t >> 0$ s are derived from flux creep. The drifts due to flux creep are described as (1.5.28). From approximate curves based on (1.5.28) in Figure 6-2 (b), apparent pin potentials at 4.2 K, 20 K and 30 K are evaluated as 18.3 meV, 47.0 meV and 54.6 meV, respectively. As temperatures rise from 4.2 K to 30 K, decays of SCFs become large as shown in Figure 6-2 (a). Therefore, the decay of the screening current at 4.2 K due to flux creep is smaller than those at 20 K and 30 K.

(B) Temporal variations of SCFs generated by superimposed-CCs.

Figure 6-3 (a) shows drifts of SCFs as a function of the number of superimposed-CCs. Figure 6-3 (b) shows the SCFs normalized by the values at $t$ = 100 s. The temporal variations of normalized SCF are $3.2\times10^4$ ppm/h in duration of 100 s < $t$ < 4000 s. These results confirm that drifts of SCFs due to flux creep for the superimposed-CCs are independent of the number of CCs. At $t$ = 4000 s, the variations are $1.8\times10^4$ ppm/h. The rates of temporal drifts of SCF are very high for NMR magnets.

(C) Temporal variations of SCFs generated by arranged- and superimposed-CCs

Figure 6-4 (a) shows temporal variation of SCF distribution produced by 3-parallel, 3-layers CCs and 3-parallel CCs. Intensities of SCF reduce and increase near center and edges of the CCs, respectively. This is caused by dissipations of screening currents flowing in CCs. Therefore, the reduction of SCF around the center of the CC is large compared with the other regions. The variation and intensity of SCF for 3-parallel, 3-layers CCs is larger than that for 3-parallel CCs. Figure 6-4 (b) shows the SCFs at a position ($x$, $z$) = (0.2 mm, 0.4 mm) normalized by the values at $t$ = 100 s. Temporal variation of the normalized SCF for 3-parallel, 3-layers CCs is seemingly a little different from the variations of the normalized SCF for 3-parallel and 5-parallel CCs. The temporal variation of the SCF for 3-parallel, 3-layers CCs normalized at $t$ = 300 s is same as those normalized at $t$ = 100 s for 3-parallel and 5-parallel CCs. This is because the temporal decay due to normal conductors, which are given by the second term of (6.2.1), gets slow on account of increase of the surrounding CCs. Temporal variation of the normalized SCF due to flux creep for arranged and /or superimposed CCs did not have interactions between the CCs. Accordingly, a factor determining rate of temporal decay at 4.2 K can be seen as amount of magnetic flux in the CCs.

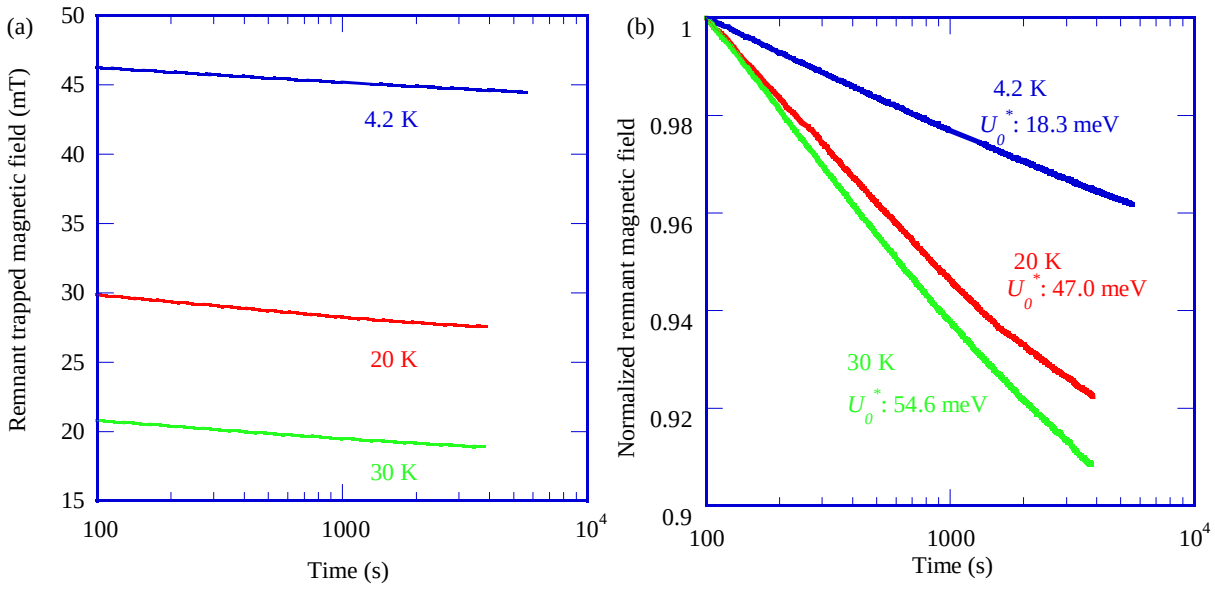


*Figure 6-2: (a) Temperature dependences of temporal variations of remnant magnetic fields at a position z = 2 mm for a CC, and the lower figure shows those normalized by the values at t = 100 s.*

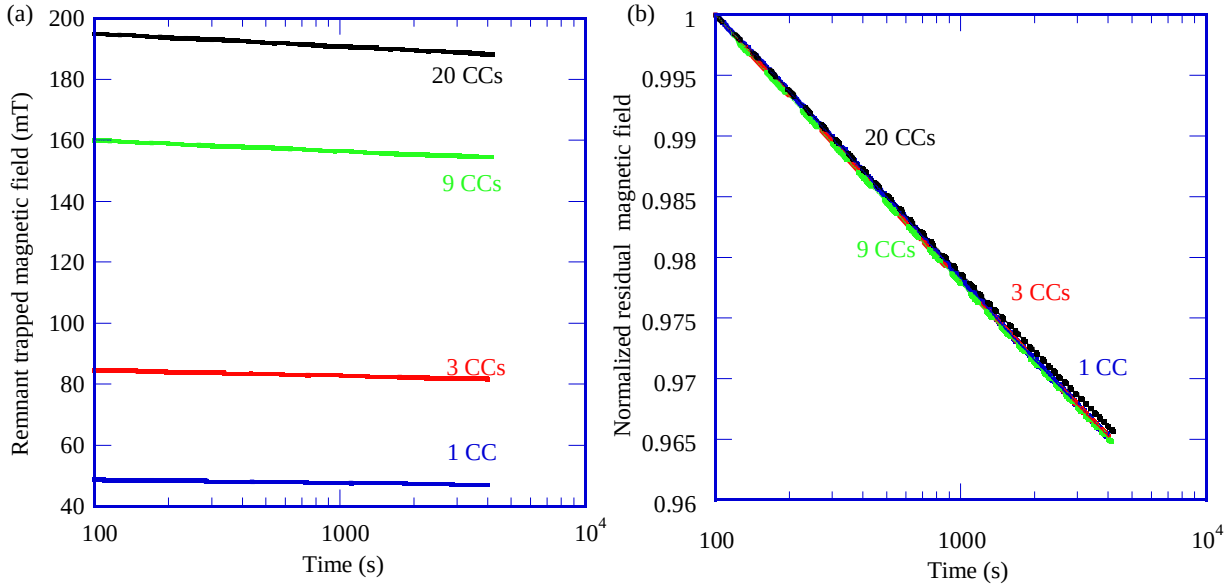


*Figrure6-3: (a) Drifts of SCFs as a function of the number of superimposed-CCs. (b) The SCF normalized by the values at t = 100 s.*

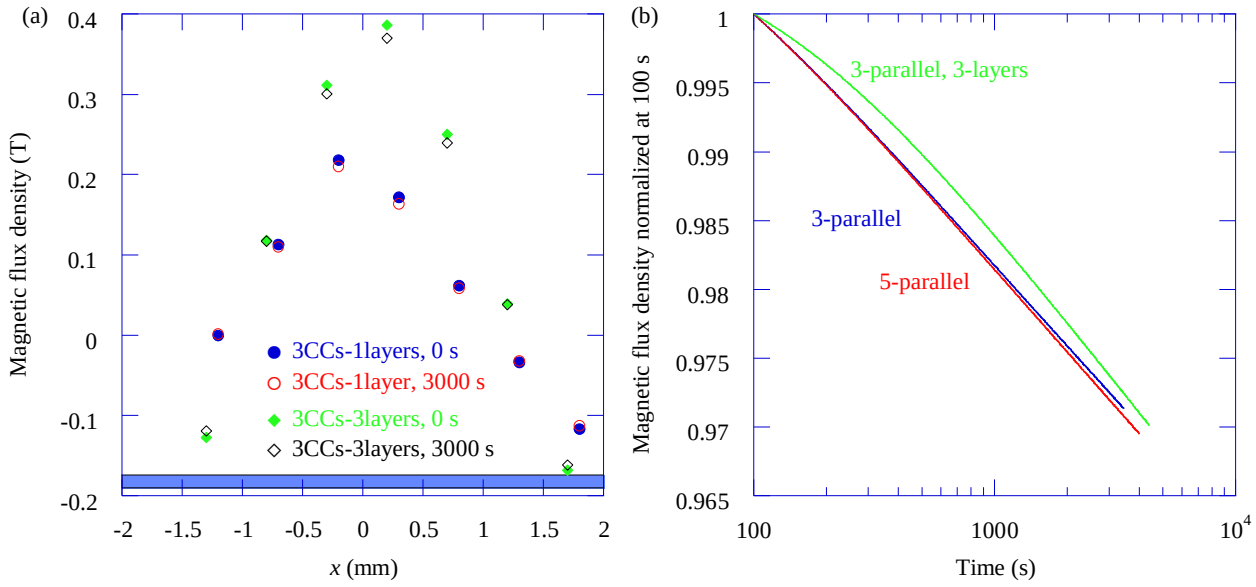


*Figure 6-4: (a) Temporal variation of SCF distribution produced by 3-parallel-3layered CCs and 3-paralle-1-layered CCs. (b) The SCFs at a position of (x, z) = (0.2 mm, 0.4 mm) normalized by the values at t = 100 s.*

### 6.3 Summary of Chapter 6

Temperature dependence of temporal variations of SCF was observed. Following a theory of flux creep [30], the decays of SCF become smaller at lower temperature. In addition, the temporal decays of SCF generated by multiple CCs are determined by amount of magnetic flux in the multiple CCs. The decays of SCF are very large for magnetic field used in NMR spectrometers. Temporal stability of a magnetic field generated by a superconducting coil for an NMR magnet is expected to be below about 3 ppm/h [69]. The temporal decays become large at the position where SCF is high. Therefore, the reduction of SCF is needed to reduce the temporal decays. Therefore, a control of current distribution in CCs is effective in order to reduce the temporal decays of a magnetic field generated by a YBCO coil. The operating condition, such as temperature, a background magnetic field, and transport current, of YBCO coils enables us to control the current distribution in the CCs.

# Chapter 7

# Magnetic Field Distribution Generated by YBCO Pancake Coil

This chapter presents a method for calculating a magnetic field generated by a pancake coil from the sheet current density estimated in chapter 3 and chapter 4. As stated in chapter 1, pancake coils have advantages from views of mechanical stress, requirement of long wires and ease of winding are suitable for a high-field magnet. The calculation method of a magnetic field generated by the coil is based on the iteration method, described in chapter 5. The calculation method may be useful as a simple method for a magnetic field taking into an account a screening current. In this chapter, the method is described in section 7.1 and then actually used in the calculation of a magnetic field generated by a pancake coil in section 7.2 and 7.3.

## 7.1 Calculation of Magnetic Field from Sheet Current Density

Magnetic flux density $B$ is analytically given using the elliptic integrals of the first and second kinds [56, 68]. Let us consider a single circular current $I$ loop with a radius of $a$ in cylindrical coordinates as shown in Figure 7-1 (a). The circular current flows on the plane of $z = 0$. The origin of the coordinate is at the center of the circular current. Then, the magnetic vector potential $A_\theta$ is given by

$$A_\theta = \frac{\mu I}{\pi k}\sqrt{\frac{a}{\rho}}\left\{\left(1-\frac{k^2}{2}\right)K(k)-E(k)\right\} \tag{7.7.1}$$

where $K(k)$, $E(k)$ are the elliptic integrals of the first and the second kinds:

$$K(k)=\int_0^{\pi/2}\frac{d\theta}{\sqrt{1-k^2\sin^2\theta}} \tag{7.7.2}$$

$$E(k)=\int_0^{\pi/2}\sqrt{1-k^2\sin^2\theta}\,d\theta \tag{7.7.3}$$

Here,

$$k^2=\frac{4a\rho}{(a+\rho)^2+z^2} \tag{7.7.4}$$

The magnetic flux density $B$ is given by

$$B = \nabla\times A_\theta \tag{7.7.5}$$

Figure 7-1 (b) shows a current model for calculating a magnetic field generated by a YBCO coil. Currents flowing in a CC are divided into the numbers of $n$ along the width. In this calculation, the current distribution, estimated in chapter 4, is employed as the divided currents. The current distribution results from screening and transport currents. Regarding each circular current loop, (7.7.5) gives $B$ at arbitrary positions.

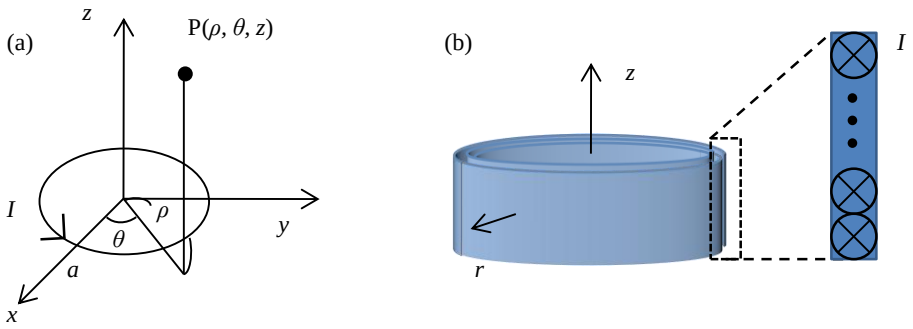


*Figure 7-1: (a) A circular current loop,*
*(b) Current model for calculating a magnetic field generated by a YBCO coil.*

## 7.2 Calculation of Magnetic Field Generated by a Pancake Coil

This section describes calculation results of magnetic-field distributions generated by a YBCO coil under a background magnetic field. Section 7.2.1 deals with differences in magnetic-field distributions generated by a single-turn YBCO coil that homogeneous and inhomogeneous currents flow. The inhomogeneous current consists of transport and screening currents. Section 7.2.2 presents magnetic-field distributions generated by multi-turn pancake coils under a background magnetic field. This section also differences in magnetic-field distributions due to history of a background magnetic field.

### 7.2.1 Difference in magnetic-field distributions generated by a single-turn coil with homogeneous and inhomogeneous current

Magnetic-field distributions generated by transport currents flowing in a single-turn YBCO coil with a diameter of 18 mm [71] were calculated. The diameter of 18 mm is large enough not to damage CCs [101]. Position ($r$, $z$) = (0 mm, 0 mm) was defined as the center of the single-turn YBCO coil.

Figure 7-2 (a) shows distributions of the $z$-component of magnetic flux densities on $z$ = 0 mm along radius of the coil. Figure 7-2 (b) shows distributions of the $z$-component of magnetic flux densities on $r$ = 0 mm along the $z$-axis. In these calculations, the distributions of sheet current density described in Brandt's critical state model were used. A CC was divided into circular currents of the numbers of 410 along the width. Magnetic-field distributions produced by homogeneous transport currents were drawn as the solid lines in Figure 7-2. The dashed lines are magnetic flux densities produced by transport and screening currents. The screening currents reduce intensities of the magnetic flux density at the center of the coil generated by a single-turn YBCO coil. As transport currents increase, the amounts of reduction in the magnetic flux density become large. The differences between the magnetic flux densities for $I_t$ = 200 A and $I_t$ = 300 A at the center of the coil, ($r$, $z$) = (0 mm, 0 mm), are 0.01 mT and 0.10 mT. This is because the $J_c$ regions, where the currents with the critical current density flow, expand from the both edges of CCs to the center. The expansion of the $J_c$ regions is described in Figure 3-14. Accordingly, an intensity of a magnetic field generated by a coil wound with CCs is not proportional to the transport current flowing in the coil. When the absolute value of the $z$ increases, the dashed lines become larger than the solid lines. This is because currents with high current densities flow in CCs near edges.

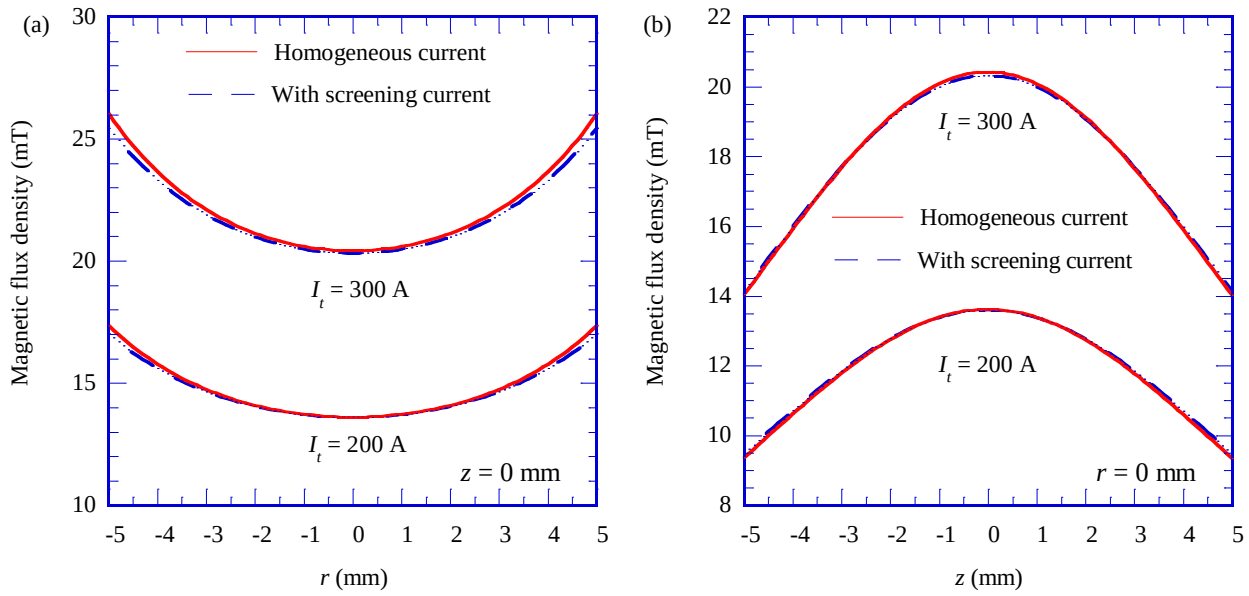


*Figure 7-2: (a) Distributions of z-component of magnetic flux densities on z = 0 mm along radius of the YBCO coil. (b)Distributions of z-component of magnetic flux densities on r = 0 mm along the z-axis. The transport currents of 200 A and 300 A are supplied to the YBCO coil.*

### 7.2.2 Magnetic-field distribution generated by multi-turn YBCO pancake coil under a background magnetic field

Magnetic-field distributions generated by transport and screening currents in a 3-layered and 3-turn YBCO pancake coil with a diameter of 18 mm were calculated. High-field superconducting magnets are composed of several coils. In particular, YBCO CCs have high critical current density under a high magnetic field. Therefore, a YBCO coil is used as an innermost coil of a high-field superconducting magnet. The YBCO coil is exposed to a background magnetic field, as shown in Figure 7-3. Here, let us consider magnetic field distributions generated by the 3-layered and 3-turn CCs near the top edge of the YBCO coil, where a magnetic field in a radial direction is highest. A homogeneous external magnetic field is applied in a radial direction of the 3-layered and 3-turn YBCO pancake coil. When the magnetic-field distribution is calculated, the interaction between CCs is taken into account using the iteration method, which is described in chapter 5.

Figure 7-4 shows a difference in the distribution of the *z*-component of magnetic flux densities on $r$ = 0 mm along the *z*-axis due to the history of a background magnetic field. The transport current supplied to the YBCO pancake coil is 200 A. The blue line shows a distribution of magnetic flux density along the *z*-axis under a background magnetic field increasing from 0 T to 1 T. The red line shows a magnetic-field distribution during a reduction of a background magnetic field from 5 T to 1 T. Magnetic-field distributions during charge and discharge of an external magnetic field are different. The peak position, where the magnetic flux density is a maximum value, shifts and homogeneity of a magnetic field changes due to the difference of a history of a background magnetic field. This is caused by a variation of the current distribution in the CC. Figure 7-5 shows distributions of the *z*-component of magnetic flux densities on $z$ = 0 mm, 1 mm, and 2 mm along the *r*-axis. The blue and red profiles show the magnetic-field distributions generated by the 3-layered and 3-turn YBCO coil under a background magnetic field of 1 T from 0 T and 5 T, respectively. The solid lines, the dashed lines, and the

triangle-and-line show the distribution on $z$ = 0 mm, 1 mm, and 2 mm, respectively. As the position is far from the center of the coil, the magnetic flux densities are more sensitive to the history of a background magnetic field.

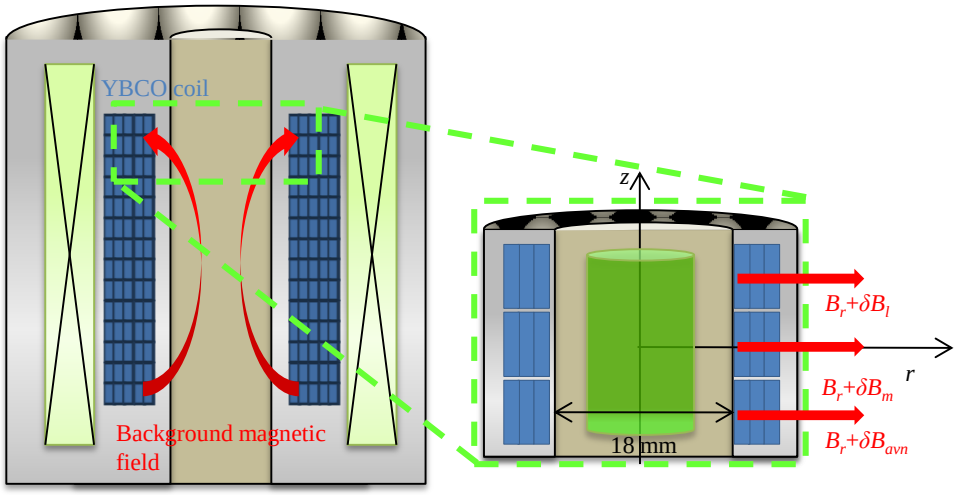


*Figure 7-3: A 3-layered and 3-turn YBCO pancake coil under a background magnetic field.*

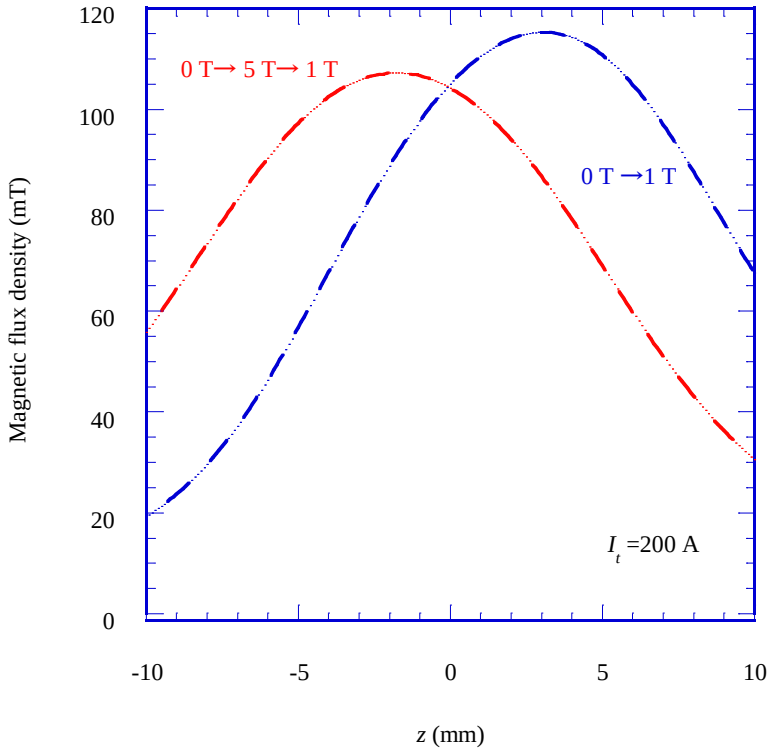


*Figure 7-4: The distributions of the z-component of magnetic flux densities on r = 0 mm along the z-axis generated by a 3-layered and 3-turn YBCO pancake coil with a diameter of 18 mm. Homogeneous magnetic field with magnetic flux density of 1 T in a radial direction of the coil is applied.*

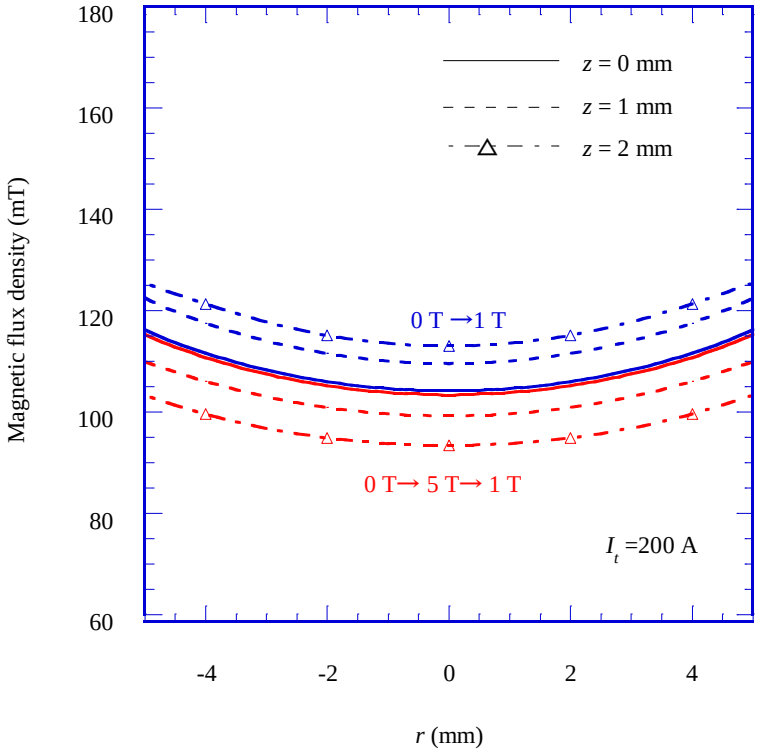


*Figure 7-5: The distributions of the z-component of magnetic flux densities on z = 0 mm, 1 mm, and 2 mm along the r-axis generated by a 3-layered and 3-turn YBCO pancake coil with a diameter of 18 mm. Homogeneous magnetic field with magnetic flux density of 1 T in a radial direction of the coil is applied.*

### 7.3 Possibility of Reducing Influence of SCF

This section presents a possibility of reducing influence of SCF. Figure 7-6 shows the *z*-component of the magnetic flux density along the *z*-axis generated by transport and screening currents flowing in a YBCO single-turn coil whose configuration is common to the coil used in section 7.2.1. The blue, red and green lines show distributions of magnetic flux densities induced by the coil with transport currents of 100 A, 200 A and 300 A, respectively. The solid lines are the distribution generated by the single-turn YBCO coil under a background magnetic field with a magnetic flux density of 0.4 T from 0 T. The dash lines are drawn in the presence of reversing background magnetic field from 0.5 T to 0.4 T. This is because current distributions in the YBCO CC interaction. In fact, operations of background magnetic field and/or transport current transfer current distributions and result in reduction of SCF.

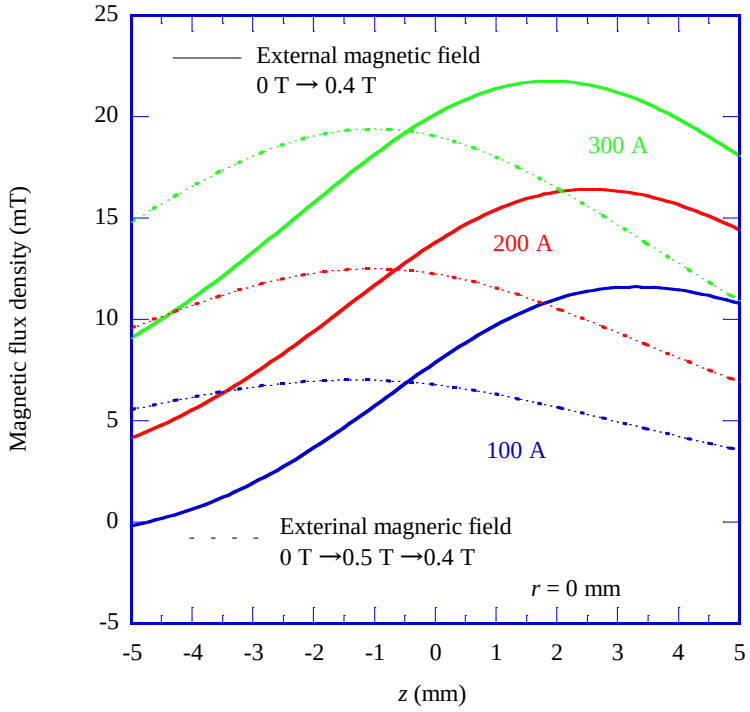


*Figure 7-6: The z-component of magnetic flux density along the z-axis generated by transport and screening currents flowing in a YBCO single-turn coil. The blue, red and green lines show distributions of magnetic flux densities induced by the coil with transport currents of 100 A, 200 A and 300 A, respectively. The solid lines are drawn as the distribution under a background magnetic field of 0.4 T during an increase. The dashed lines are drawn in the presence of reversing a background magnetic field from 0.5 T to 0.4 T.*

## 7.4 Summary of Chapter 7

This chapter presents a method for estimating distributions of magnetic flux densities generated by a pancake coil. This method enables us to calculate a magnetic-field distribution generated by the coil with screening currents. In order to take into account the screening currents in CCs, the sheet current densities, which were estimated in chapter 4, were used in this method. The calculations were carried out for a multi-turn and multi-layer YBCO coil with a background magnetic field. The history of the background magnetic field affects the magnetic-field distribution generated by the YBCO coil, especially the distribution along the *z* axis. The simple calculation is expected to be as a useful method for estimating a magnetic-field distribution including SCF generated by YBCO coils.

In addition, the calculation of magnetic flux density generated by a YBCO single-turn coil gives a possibility of reduction of drawbacks due to SCF. This result indicates that intentional operation of background magnetic field and/or transport current is effective in consideration of reducing SCF.

# Chapter 8

# Conclusions

Superconducting magnets using $YBa_2Cu_3O_{7-x}$ (YBCO) coated conductors are required to generate a high magnetic field and/or downsize. In particular, a high-field magnet generating a magnetic field with magnetic flux density above 25 T cannot be constructed using conventional superconducting wires, NbTi and $Nb_3Sn$ wires, due to their upper critical magnetic field. Compared with Bi2212 and Bi2223 wires, YBCO coated conductors have high tolerance against mechanical stress. Active researches and developments of fabricating process of the YBCO or REBCO coated conductor contribute to the applications. However, there are still some challenges to use YBCO coated conductors as a material of practical superconducting magnets. This thesis focuses on screening current in the coated conductor.

Critical current densities of coated conductors are not homogeneous over the width. Intensities of screening currents correspond to superconducting critical current. Screening current affects magnetic field generated by a superconducting magnet as follows: reduction of magnetic flux density at the center, inhomogeneity of magnetic flux density and temporal variations of magnetic field. That is why it is very important to evaluate how screening current flows in YBCO coated conductors. This thesis presents understandings of the current distribution and the temporal variation of the screening current flowing in the coated conductor. Based on the understandings, a magnetic field distribution generated by a YBCO coil is calculated.

Chapter 1 presents a background and a purpose of this thesis as stated above.

Chapter 2 describes the experimental equipments used in this research. The equipments enable us to conduct a measurement of a magnetic field distribution under a high magnetic field in liquid helium, nitrogen, and helium gas. The measurement provides magnetic flux densities at positions up to seven points at the same time.

In chapter 3, a model for solving current distributions in a single YBCO coated conductor is suggested. Then, the model is verified from the agreement between the solution and experimental results. In the model, the coated conductor is divided along the width and one-dimensional currents flow in the divided area. Magnetic-field distributions are measured in order to estimate the current distribution. The inverse problem of Biot-Savart law is solved using Tikhonov regularization. In the verification, it transpires that the screening-current distribution in the coated conductor under a low magnetic field agrees with the Brandt's model.

Chapter 4 describes current distributions estimated from the actual magnetic-field distributions using the method verified in chapter 3. The current distributions are verified experimentally that under a high background field, where magnetic flux exists at the center of the coated conductor, total current distributions consisting of screening and transport currents are determined by the intensity of transport current relative to the critical current. The critical current depends on intensity and angular dependences of a background magnetic field and temperature. In other words, operating temperature, a transport current and a background magnetic field of a

YBCO coil determines a current distribution in the coated conductor. On the other hand, under a low magnetic field, the critical current is so large that an external magnetic field to be applied is dominant to the current distributions.

Chapter 5 plays the role of binding chapter 4 and chapter 7. This chapter deals with distributions of a magnetic field produced by the multiple YBCO coated conductors. Superconducting coils have number of layers and turns of superconducting wires. Electromagnetic designs of YBCO coils require an understanding of interactions of screening current in multiple coated conductors. In this chapter, a method for estimating the magnetic field distributions generated by the multiple coated conductors is suggested. The calculation model employs the current distribution including screening currents, which is estimated in chapter 4. The calculation results of the magnetic-field distributions agree with experimental results very well. In addition, when the magnetic field generated by a coated conductor is much higher than a background magnetic field, the interaction between multiple coated conductors is negligible.

In this thesis, only chapter 6 deals with temporal variations of screening current induced field. However, the variation is very important for designing an NMR magnet, including main coils, shim coils, and lock systems. This chapter focuses on temporal variations of screening current induced field for multiple coated conductors. The temporal variations can be estimated by the amount of magnetic flux in the coated conductors. The temporal variations are very large for conventional NMR magnets, and especially, are crucial problems for constructing YBCO-based NMR magnets.

Chapter 7 presents a method for calculating a magnetic-field distribution generated by a YBCO coil. The method employs the current distribution in chapter 4 and then, takes into account interaction between coated conductors, as described in chapter 5. The method was expanded to the multi-turn and multi-layered coil. This method is useful as a method for calculating briefly magnetic field distribution. The calculation using the distributions of coil current gives knowledge that intentional operations of transport current and a background magnetic field are effective in order to reduce influences due to screening current.

This thesis reveals a relation between screening and transport currents in a coated conductor and then, a coil design based on the inhomogeneous current distribution including screening current becomes possible. This design method may promote a construction of YBCO magnet. In order to reduce the influence by screening currents in YBCO coated conductor, controls of operating temperature, current, and background magnetic field are effective. In addition, innovative magnet systems, such as shim coils and compensation coils for YBCO magnets are needed.

# Appendix

**A: Infulence of a screening current in a coated conductor on rate of varying an external magnetic field**

The difference in a screening current induced field SCF between rates of varying an external magnetic field was examined in the experiment. The experimental setup is illustrated in Figure 2-5. The distance between the voltage taps was 2.9 mm. The external magnetic field was increased and decreased at rate of 14.4 mT/s and 7.2 mT/s. During the increase and decrease, we observed magnetic flux density at a position of 2 mm above the center of the coated conductor and induced electromotive force between the voltage taps.

Figure A-1 shows the magnetic flux density and the induced electromotive force. The red and blue lines show the values observed at rates of 14.4 mT/s and 7.2 mT/s, respectively. The two solid arrows point to what the profiles show. The four dashed arrows denote the direction of varying the external magnetic field. The blue and red profiles for the magnetic flux densities are superposed very well. This indicates that the value of the magnetic flux denisty does not depend on the rate of varying the external magnetic field and the screening currents are the critical currents. On the other hand, the hysteresis area of the red profile for the induced electromotive force is twice the area of the blue profile. Faraday's law is given by

$$\nabla \times \boldsymbol{E} = -\frac{\partial \boldsymbol{B}}{\partial t} \qquad \text{(A. 1)}$$

The induced electromotive force follows the Faraday's law.

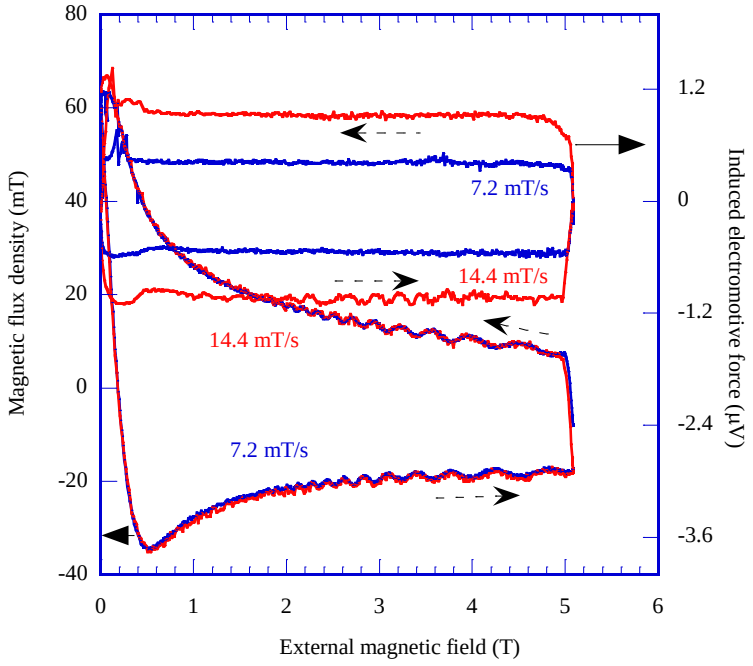


*Figure A-1: The magnetic flux density and the induced electromotive force produced by a coated conductor under varying an external magnetic field.*

**B: Discussion about solutions of one-dimensional inverse problem using the Tikhonov regularization method**

As stated in section 3.3.2, a calculation for the current distribution in the coated conductor employs the Tikhonov regularization method. The $\lambda$ was determined to minimize the (3.3.4). Section B. 1 presents the current distribution for variable $\lambda$. In addition, how the experimental error for positions of the Hall sensor influence is described in section B.2. In both section B. 1 and B. 2, we discuss the current distribution in a coated conductor under an external magnetic field with magnetic flux of 1 T perpendicular to the tape surface. The current does not include a transport current, but only a screening current. The current distribution was calculated from the magnetic field distribution based on the Brandt's model.

B. 1: Difference in the solution for the variable $\lambda$ used in the Tikhonov regularization method

Figure B-1 shows the distribution of sheet current density in the coated conductor under an external magnetic field with magnetic flux density of 1 T. The sheet current densities were estimated using variable $\lambda$. The coated conductor is placed on -2.05 mm < $x$ < 2.05 mm. The magnetic flux exists over the entire width of the coated conductor under the external magnetic field with the magnetic flux density of 1 T. Therefore, the sheet current densities are the positive and negative critical sheet current density in $x$ < 0 mm and $x$ > 0 mm, respectively. The critical sheet current density under 1 T is 138 kA/m. When $\lambda$ is more than $5\times10^{9}$, the absolute values of the sheet current densities are just about 138 kA/m. In addition, when $\lambda$ is more than $5\times10^{10}$, the sheet current densities near $x$ = 0 mm is much larger than the critical sheet current density. Accordingly, $5\times10^{9}$ is used as $\lambda$ in this thesis.

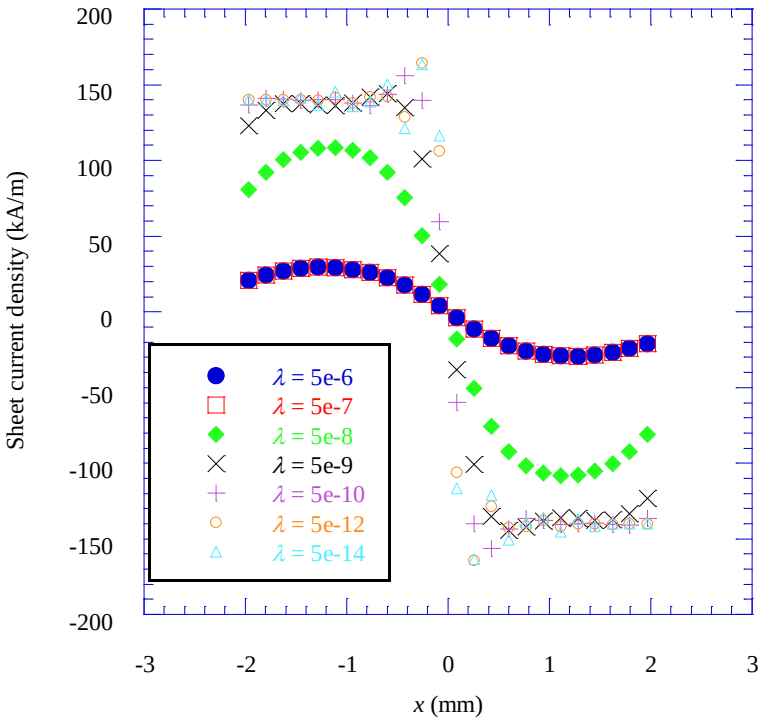


*Figure B-1: Distribution of sheet current density in the coated conductor under an external magnetic field with magnetic flux density of 1 T. The sheet current densities were estimated using the variable $\lambda$.*

B. 2: Difference in the solution due to the position error of the Hall sensor

Figure B-2 shows the distribution of the sheet current density in the coated conductor under an external magnetic field with the magnetic flux of 1 T. The distributions were estimated from variable *z*, which is a distance between the active area of a Hall sensor and the superconducting layer of the coated conductor, with the following procedure:

1) The magnetic field distribution at $z$ = 0.37 mm was estimated based on the Brandt's model.
2) The distributions of the sheet current density were solved from the magnetic field distribution at $z$ = 0.37 mm using the Tikhonov regularization method. In the method, the $z$ was arbitrarily varied as 0.37 mm, 0.5 mm, 0.6 mm, and 1 mm. The $z$ = 0.37 mm was a correct value.

The black crosses show the distribution of the sheet current density based on the critical state model. The ideal sheet current density, plotted as the black crosses, varies nonlinearly near the center of the coated conductor. The distributions estimated through the inverse problem cannot adequately describe the nonlinear variation near $x$ = 0 mm. However, the black circles, which is the distribution for $z$ = 0.37 mm, show the same values as the black crosses. As the difference between the correct $z$ (= 0.37 mm) and the variable $z$ increases, the distributions become more upward convex curves.

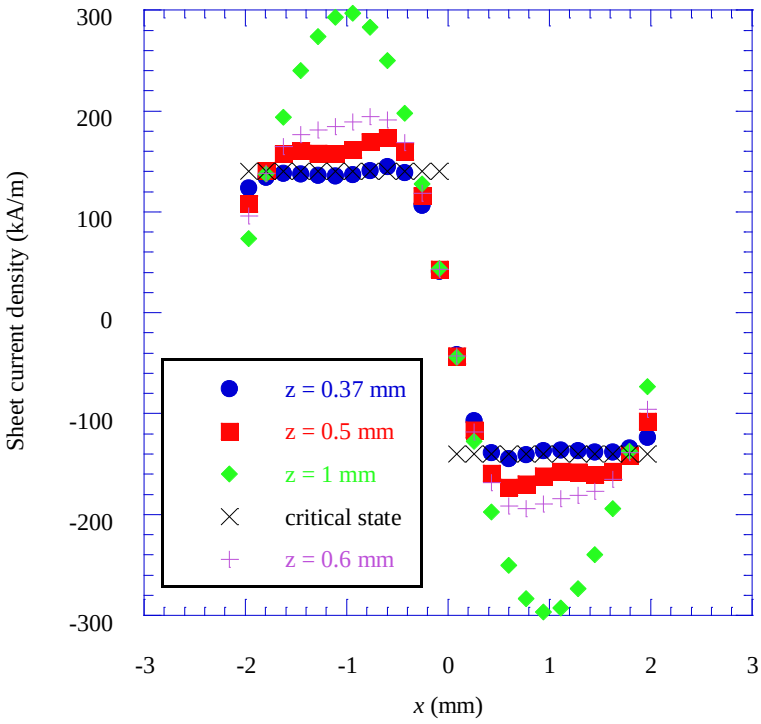


*Figure B-2: Distribution of sheet current density in the coated conductor under an external magnetic field with magnetic flux density of 1 T. The sheet current densities were estimated using the variable z.*

# Bibliography


[1] K. H. Onnes, Proc. Akad. Wetensch. Amsterdam **14** 820

[2] W. Meissner and R. Ochsenfeld, "Ein neuer Effekt bei Eintritt der Supraleitfähigkeit," *Naturwissenschaften* **21** (44) 787–788 1933.

[3] J. K. Hulm and B. T. Matthias, "Overview of superconducting materials development," in *Superconductor Materials Science-Metallurgy, Fabrication, and Applications*, Eds., S. Foner and B. B. Schwarz (Plenum Press, New York, 1981), 1.

[4] Charles P. Poole, Jr., Horacio A. Farach and Richard J. Creswick, "Superconductivity," Academic Press, 1995

[5] J. G. Bednorz and K. A. Müller, "Possible High $T_c$ Superconductivity in the Ba-La-Cu-O System," *Z. Phys. B, Condensed Matter* **64** 189-193 1986.

[6] M. K. Wu, J. R. Ashburn, C. J. Torng, P. H. Hor, R. L. Gao, Z. J. Huang, Y. Q. Wang and C. W. Chu, "Superconductivity at 93 K in a New Mixed-Phase Y-Ba-Cu-O Compound System at Ambient Pressure," *Phys. Rev. Let.* **58** 908-910 1987.

[7] Jun Nagamatsu, Norimasa Nakagawa, Takahiro Muranaka, Yuji Zenitani and Jun Akimitsu, "Superconductivity at 39K in magnesium diboride," *Nature* **410** 63-64 2001.

[8] Yoichi Kamihara, Hidenori Hiramatsu, Masahiro Hirano, Ryuto Kawamura, Hiroshi Yanagi, Toshio Kamiya and Hideo Hosono, "Iron-Based Layered Superconductor: LaOFeP," *J. Am. Chem. Soc.* **128** 10012-10013 2006.

[9] J. W. Ekin, "Experimental technique for low-temperature measurements," OXFORD University Press 2006.

[10] Takayoshi Miyazaki, Takayuki Miyatake, Hiroyuki Kato, Kyoji Zaitsu, Yukinobu Murakami, Takashi Hase and Mamoru Hamada, "Development of $Nb_3Sn$ superconducting wires for high field magnets at Kobe Steel and JASTEC," *Cryogenics* **48** 341-346 2008.

[11] J. Schwartz, F. Hunte, W. K. Chan, X. F. Gou, X. T. Liu, M. Phillips, Q. V. Le, G. Naderi, M. Turenne and L. Ye, "Status of High Temperature Superconductor Based Magnets and The Conductors They Depend upon," HE-LHC'10 AccNet Mini-Workshop on a "High Energy LHC." Reference No. ST262; Category 5, 6.

[12] J. W. Ekin, "Strain scaling law for flux pinning in practical superconductors. Part 1: Basic relationship and application to $Nb_3Sn$ superconductors," *Cryogenics*, **20**, 611-624 1980.

[13] Y. Shiohara, N. Fujiwara, H. Hayashi, S. Nagaya, T. Izumi and M. Yoshizumi, "Japanese efforts on coated conductor processing and its power application: New 5 year project for materials and power applications of coated conductors (M-PACC)," *PhysicaC*, **469** 863-867 2009

[14] R. Teranishi, T. Izumi and Y. Shiohara, "Highlights of coated conductor development in Japan," *Supercond. Sci. Tecnol.***19** S4-S12 2006

[15] Xudong Wang, Hiroshi Ueda, Atsushi Ishiyama, Masashi Yagi, Shinichi Mukoyama, Masayoshi Ohya, Takato Masuda, Naoji Kashima, Shigeo Nagaya and Yuh Shiohara, "Over-Current Characteristics of a 20-m-Long YBCO Model Cable," *IEEE Trans. Applied Superconductivity*, **19** 1722-1726 2009.

[16] V. Selvamanickam, Y. Chen, X. Xiong, Y. Y. Xie, J. L. Reeves, X. Zhang, Y. Qiao, K. P. Lenseth, R. M. Schmidt, A. Rar, D. W. Hazelton and K. Tekletsadik, "Recent Progress in Second-Generation HTS Conductor Scale-up at SuperPower," *IEEE Trans. Applied Superconductivity*, **17** 3231-3234 2007.

[17] Koji Shikimachj, Naoki Hirano, Shigeo Nagaya, Hiroshi Kawashima, Kohei Higashikawa and Taketsune Nakamura, "System Coordination of 2 GJ Class YBCO SMES for Power System Control," *IEEE Trans. Applied Superconductivity*, **19** 2012-2018 2009

[18] A. Tomioka, T. Otonari, T. Ogata, M. Iwakuma, H. Okamoto, H. Hayashi, Y. Iijima, T. Saito, Y. Gosho, K. Tanabe, T. Izumi and Y. Shiohara, "AC over-current test results of YBCO power transformer with fault current limiting function," *PhysicaC* in press.

[19] K. Nagao, T. Nakamura, T. Nishiuma, Y. Ogama, N. Kashima, S. Nagaya, K. Suzuki, T. Izumi and Y. Shiohara, "Development and fundamental characteristics of a YBCO superconducting induction/synchronous motor operated in liquid nitrogen," *Supercond. Sci. Tecnol.*, **21** 015022 2008.

[20] A. B. Abrahamsen, N. Mijatovic, E. Seiler, T. Zirngibl, C. Træholt, P. B. Nørgård, N. F. Pedersen, N. H. Andersen and J. Østergård, "Superconducting wind turbine generators," *Supercond. Sci. Tecnol.***23** 034019 2010.

[21] V. Selvamanickam Y. Chen, X. Xiong, Y. Y. Xie, M. Martchevski, A. Rar, Y. Qiao, R. M. Schmidt, A. Knoll, K. P. Lenseth, and C. S. Weber, "High Performance 2G wires: From R & D to Pilot-Scale Manufacturing," *IEEE Trans. Applied Superconductivity*, **19** 3225-3230 2009.

[22] K. Kakimoto, M. Igarashi, S. Hanyu, Y. Sutoh, T. Takemoto, T. Hayashida, Y. Hanada, N. Nakamura, R. Kikutake, H. Kutami, Y. Iijima and T. Saitoh, "Long RE123 Coated Conductors with High Critical Current over 500 A/cm by IBAD/PLD Technique," *PhysicaC* in press.

[23] D. Dimos, P. Chaudhari, J. Mannhart and F. K. LeGoues, "Orientation Dependence of Grain-Boundary Critical Currents in $YBa_2Cu_3O_{7-\delta}$ Bicrystals," *Phys. Rev. Lett.* **61** 219-222 1988.

[24] Amit Goyal, "Second-Generation HTS Conductors," Kluwer Acadeemic Publishers 2005.

[25] V. Braccini, A. Xu, J. Jaroszynski, Y. Xin, D. C. Larbalestier, Y. Chen, G. Carota, J. Dackow, I. Kesgin, Y. Yao, A. Guevara, T. Shi and V. Selvamanickam, "Properties of recent IBAD-MOCVD coated conductors relevant to their high field, low temperature magnet use," *Supercond. Sci. Technol.*, **24** 035001 2011

[26] Yasuhiro Iijima, Nobuo Tanabe, Yoshimitsu Ikeno and Osamu Kohno, "Biaxiallly Aligned $YBa_2Cu_3O_{7-x}$ Thin Film Tapes," *PhysicaC*, **185-189** 1959-1960 1991.

[27] Gerald B. Stringfellow, "Organometallic Vapor-Phase Epitaxy: Theory and Practice," Academic Press, San Diego 1989

[28] Davide Uglietti, Hitoshi Kitaguchi, Seyong Choi and Tsukasa Kiyoshi, "Angular Dependence of Critical Current in Coated Conductors at 4.2 K and Magnet Design," *IEEE Trans. Applied Superconductivity*, **19** 2909-2912 2009

[29] A. Otsuka, T. Kiyoshi and M. Takeda, "A 1.3 GHz NMR magnet Design Under High Hoop Stress Condition," *IEEE Trans. Applied Superconductivity*, **20** 596-599 2010

[30] Teruo Matsushita, "Flux Pinning in Superconductors," Springer-Verlag Berlin Heidelberg 2007

[31] B. Maiorov, S. A. Baily, H. Zhou, O. Ugurlu, J. A. Kennison, P. C. Dowden, T. G. Holesinger, S. R. Foltyn and L. Civale, "Synergetic combination of different types of defect to optimize pinning landscape using $BaZrO_3$-doped $YBa_2Cu_3O_7$," *Nature Materials*, **8** 398-404 2009

[32] Paolo Mele, Kaname Matsumoto, Tomoya Horide, Ataru Ichinose, Masashi Mukaida, Yutaka Yoshida, Shigeru Horii and Ryusuke Kita, "Ultra-high flux pinning properties of $BaMO_3$-doped $YBa_2Cu_3O_{7-x}$ thin films (M = Zr, Sn)," *Supercond. Sci. Technol.*, **21** 032002 2008.

[33] Y. Yamada, K. Takahashi, H. Kobayashi, M. Konishi, T. Watanabe, A. Ibi, T. Kato, S. Miyata, T. Kato, T. Hirayama and Y. Shiohara, "Epitaxial nanostructure and defects effective for pinning in Y(RE) $Ba_2Cu_3O_{7-x}$ coated conductors," *Appl. Phys. Lett.*, **87** 132502 2005.

[34] A. Xu, J. Jaroszynski, F. Kametani, Z. Chen, D. C. Labalestier, Y. L. Viouchkov, Y. Chen, Y. Xie and V. Selvamanickam, "Angular dependence of Jc for YBCO coated conductors at low temperature and very high magnetic fieds," *Supercond. Sci. Technol.*, **23** 014003 2010.

[35] V. Braccini, A. Xu, J. Jaroszynski, Y. Xin, D. C. Labalestier, Y. Chen, G. Carota, J. Dackow, I. Kesgin, Y. Yao, A. Guevara, T. Shi and V. Selvamanickam, "Properties of recent IBAD-MOCVD coated conductors relevant to their field, low temperature magnet use," *Supercond. Sci. Technol.*, **24** 035001 2011.

[36] J. W. Ekin, D. K. Finnemore, Qiang Li, J. Tenbrink and W. Carter, "Effect of axial strain on the critical current of Ag-sheathed Bi-based superconductors in magnetic fields up to 25 T," *Appl. Phys. Lett.*, 61 858-860 1992.

[37] D. C. vander Lan, H. J. N. van Eck, B. ten Haken, H. H. J. ten Kate and J. Schwartz, "Strain Effects in High Temperature Superconductors Investigated With Magneto-Optical Imaging," *IEEE Trans. Applied Superconductivity*, 13 3534-3539 2003.

[38] K. Osamura, S. Machiya, H. Suzuki, S. Ochiai, H. Adachi, N. Ayai, K. Hayashi and K. Sato, "Mechanical behavior and strain dependence of the critical current of DI-BSCCO tapes", *Supercond. Sci. Technol.*, **21** 054010 2008.

[39] Michinaka Sugano, Kouji Shikimachi, Naoki Hirano and Shigeo Nagaya, "The reversible strain effect on critical current over a wide range of temperatures and magnetic fields for YBCO coated conductors," *Supercond. Sci. Technol.*, **23** 085013 2010

[40] M. Sugano, Y. Yoshida, M. Hojo, K. Shikimachi, N. Hirano and S. Nagaya, "Two different mechanisms of fatigue damage due to cyclic stress loading at 77 K for MOCVD-YBCO-coated conductors", *Supercond. Sci. Technol.*, **21** 054006 2008.

[41] I. I. Rabi, J. R. Zacharias, S. Millman and P. Kusch, "A New Method of Measuring Nuclear Magnetic Moment," *Phys. Rev.*, **53** 318 1938

[42] For example, Paul T. Callaghan, "Principles of Nuclear Magnetic Resonance Microscopy," Oxford University Press Inc., New York 1993.

[43] *Superconductivity communications*, Vol. 16, No. 1, February 2007.

[44] Kenjiro Hashi, Tadashi Shimizu, Atsushi Goto, Tsukasa Kiyoshi, Shinji Matsumoto, Hitoshi Wada, Teruaki Fujito, Ken-ichi Hasegawa, Masatoshi Yoshikawa, Takahshi Maki, Satoshi Ito, Mamoru Hamada and Seiji Hayashi, "Achievement of a 920-MHz High Resolution NMR," *J. Mag. Reson.*, **156** 318-321 2002.

[45] Tsukasa Kiyoshi, Shinji Matsumoto, Akio Sato, Masatoshi Yoshikawa, Satoshi Ito, Osamu Ozaki, Takayoshi Miyazaki, Takashi Miki, Takashi Hase, Mamoru Hamada, Takashi Noguchi, Shigeo Fukui and Hitoshi Wada, "Operation of a 930-MHz High-Resolution NMR Magnet at TML," *IEEE Trans. Applied Superconductivity*, **15** 1330-1333 2005.

[46] Tsukasa Kiyoshi, Masatoshi Yoshikawa, Akio Sato, Kikuo Itoh, Shinji Matsumoto, Hitoshi Wada, Satoshi Ito, Takashi Miki, Takayohi Miyazaki, Takeshi Kamikado, Osamu Ozaki, Takashi Hase, Mamoru Hamada, Seiji Hayashi, Yoshio Kawate and Ryoichi Hirose, "Operation of a 920-MHz High-Resolution NMR Magnet at TML," *IEEE Trans. Applied Superconductivity*, **13** 1391-1395 2003.

[47] T. Miyazaki, H. Kato, T. Hase, M. Hamada, Y. Murakami, K. Itoh, T. Kiyoshi and H. Wada, "Development of High Sn Content Bronze Processed Nb3Sn Superconducting Wire for High Field Magnets," *IEEE Trans. Applied Superconductivity*, **14** 975-978 2004.

[48] online, http://www.bruker-biospin.com/pr090601.html

[49] M. Tsuchiya, T. Wakuda, K. Maki, T. Shiino, H. Tanaka, N. Saho, H. Tsukamoto, S. Kido, K. Takeuchi, M. Okada and H. Kitaguchi, "Development of Superconducting Split Magnets for NMR Spectrometer," *IEEE Trans. Applied Superconductivity*, **18** 840-843 2008.

[50] W. D. Markiewicz, I. R. Dixon, C. A. Swenton, W. S. Marshall, T. A. Painter, S. T. Bole, T. Cosmus, M. Parizh, M. King and G. Ciancetta, "900 MHz Wide Bore NMR Spectrometer Magnet at NHMFL," *IEEE Trans. Applied Superconductivity*, **10** 728-731 2000.

[51] Iain R. Dixon, W. Denis Markiewicz, William W. Brey and Kiran K. Shetty, "Performance of the Ultra Wide Bore 900 MHz NMR Magnet at the National High Magnetic Field Laboratory," *IEEE Trans. Applied Superconductivity*, **15** 1334-1337 2005.

[52] W. Denis Markiewicz, John R. Miller, Justin Schawartz, Ulf P. Trociewitz and Huub W. Weijers, "Perspective on a Superconducting 30 T/1.3 GHz NMR Spectrometer Magnet," *IEEE Trans. Applied Superconductivity*, **16** 1523-1526 2006.

[53] Juan Bascuñán, Seungyong Hahn, Dong Keun Park and Yukikazu Iwasa, "A 1.3 GHz LTS/HTS Magnet- A Progress Report," *IEEE Trans. Applied Superconductivity*, **21** 2092-2095 2011.

[54] T. Kiyoshi, A. Otsuka, S. Choi, S. Matsumoto, K. Zaitsu, T. Hase, M. Hamada, M. Hosono, M. Takahashi, T. Yamazaki and H. Maeda, "NMR upgrading project towards 1.05 GHz," *IEEE Trans. Applied Superconductivity*, **18** 860-863 2008.

[55] T. Kiyoshi, Seyong Choi, Shinji Matsumoto, Kyoji Zaitsu, Takashi Hase, Takayoshi Miyazaki, Mamoru Hamada, Masami Hosono and Hideaki Maeda, "Bi-2223 Innnermost Coil for 1.03 GHz NMR Magnet," *IEEE Trans. Applied Superconductivity*, **21** 2110-2113 2011.

[56] Martin N. Wilson, "Superconducting Magnets," OXFORD University Press 1983.

[57] Yukikazu Iwasa, "Case Studies in Superconducting Magnets Design," Plenum Press 1994.

[58] Jun Lu, Ke Han, William R. Sheppard, Youri L. Viouchkov, Kenneth W. Pickard and William Denis Markiewicz, " Lap Joint Resistance of YBCO Coated Conductors," *IEEE Trans. Applied Superconductivity*, **21** 3009-3012 2011

[59] J. Y. Kato, N. Sakai, S. Tajima, S. Miyata, M. Konishi, Y. Yamada, N. Chikumoto, K. Nakao, T. Izumi, Y. Shiohara, "Diffusion joint of YBCO coated conductors using stabilizing silver layers," *PhysicaC*, **445-448** 686-688 2006.

[60] Yi-Yuan Xie, Maxim Marchevsky, Xun Zhang, Kenneth Lenseth, Yimin Chen, Xuming Xiong, Yunfei Qiao, Andrei Rar, Balvinder Gogia, Robert Schmidt, Allan Knoll, Venkat Selvamanickam,Gopal Ganesan Pethuraja and Partha Dutta, "Second-Generation HTS Conductor Design Engineering for Electrical Power Applications," *IEEE Trans. Applied Superconductivity*, **19** 3009-3013 2009.

[61] Shinji Matsumoto, Tsuksa Kiyoshi, Akihiro Otsuka, Mamoru Hamada, Hideaki Maeda, Yoshinori Yanagisawa, Hideki Nakagome and Hiroto Suematsu, "Development of the next-generation NMR technology using HTS materials; For achievement of HTS coil with high operating current density (3) – Experimental results of REBCO coil including a joint between conductors under electro-magnetic forces -," *Abstracts of CSJ conference*, **84** 181 2011.

[62] Tomoyuki Naito, Hiroyuki Fujishiro, Hiroshi Okamoto, Hidemi Hayashi, Noboru Fujiwara, Yoshihiro Gosho and Yuh Shiohara, "Thermal conductivity of YBCO coated conductors fabricated by IBAD-PLD method," *Supercond. Sci. Technol.*, **23** 105013 2010.

[63] Taketsune Nakamura, Yuichi Koyama, Hitoshi Yamakawa, Ikkoh Funaki and Naoyuki Amemiya, "Study on thickness-direction thermal diffusivity of Bi- and Y-system HTS conductors," *Abstracts of CSJ conference*, **84** 183 2011.

[64] W. D. Markiewica and C. A. Swenson, "Winding strain analysis for YBCO coated conductors", *Supercond. Sci. Technol.* **23** 045017 2010.

[65] T. Takematsu, R. Hu, T. Takao, Y. Yanagisawa, H. Nakagome, D. Uglietti, T. Kiyoshi, M. Takahashi, H. Maeda, "Degradation of the performance of a YBCO-coated conductor double pancake coil due to epoxy impregnation," *PhysicaC*, **470** 674-677 2010.

[66] Hiroshi Miyazaki, Sadanori Iwai, Taizo Tosaka, Kenji Tasaki, Satoshi Hanai, Masami Urata, Shigeru Ioka and Yusuke Ishi, "Thermal runaway of conduction-cooled impregnated YBCO coil," *Abstracts of CSJ conference*, **82** 197 2010.

[67] Seungyong Hahn, Juan Bascuñán, Haigun Lee, Emanuel S. Bobrov, Wooseok Kim, Min Cheol Ahn and Yukikazu Iwasa, "Operation and performance analyses of 350 and 700 MHz low-/high-temperature superconductor nuclear magnetic resonance magnets: A march toward operating frequencies above 1 GHz," *J. Appl. Phys.*, **105** 024501 2009.

[68] N. Amemiya and K. Akachi, "Magnetic field generated by shielding current in high $T_c$ superconducting coils for NMR magnets," *Supercond. Sci. Technol*., **21** 095001 2008.

[69] Y. Yanagisawa, H. Nakagome, Y. Koyama, R. Hu, T. Takao, M. Hamada, T. Kiyoshi, M. Takahashi, and H. Maeda, "Effect of current sweep reversal on the magnetic field stability for a Bi-2223 superconducting solenoid," *Physica C*, **469** 1996-1999 2009.

[70] D. Uglietti, Y. Yanagisawa, H. Maeda and T. Kiyoshi: "Measurements of magnetic field induced by screening currents in YBCO solenoid coils," *Supercond. Sci. Technol*., **23** 115002 2010.

[71] Y. Yanagisawa, H. Nakagome, D. Uglietti, T. Kiyoshi, R. Hu, T. Takematsu, T. Takao, M. Takahashi and H. Maeda, "Effect of YBCO-coil shape on the screening current-induced magnetic field intensity," *IEEE Trans. Applied Superconductivity*, **20** 744-747 2010.

[72] T. Matsushita and E. S. Otabe, "Flux Creep in a Sinusoidal Washboard Potential in Superconductors," *Jpn. J. Appl. Phys.*, **31**, L33-L35 1992.

[73] W. Xing, B. Heinrich, Hu Zhou, A. AA. Fife and A. R. Cragg, "Magnetic flux mapping, magnetization, and current distributions of $YBa_2Cu_3O_7$ thin films by scanning Hall probe measurements," *J. Appl. Phys.*, **76** 4244-4255 1994.

[74] I. Iguchi, T. Takeda, A. Sugimoto, T. Imaizumi, H. Haibara and T. Kawai, "Meissner state of high-$T_c$ oxide thin films observed by scanning superconducting quantum interference device microscopy," *Appl. Phys. Lett.*, **83** 2193-2195 2003.

[75] Ch Jooss, J. Albrecht, H. Kuhn, S. Leonhardt and H. Kronmüller, "Magneto-optical studies of current distributions in high-$T_c$ superconductors," *Rep. Prog. Phys.*, **65** 651-788 2002.

[76] B. ten Haken, H. J. van Eck and H. H. J. ten Kate, "A new experimental method to determine the local critical density in high-temperature superconducting tapes," *PhysicaC*, **334** 163-167 2000.

[77] Naoyuki Amemiya, Yoshichika Shinkai, Yasuhiro Iijima, Kazuomi Kakimoto and Kaoru Takeda, "Experimental determination of two-dimensional critical current density distribution in YBCO coated conductors," *Supercond. Sci. Technol.*, **14** 611-617 2001.

[78] M. Hangyo, S. Tomozawa, Y. Murakami, M. Tonouchi, M. Tani, Z Wang, K. Sakai and S. Nakashima, "Terahertz radiation from superconductive $YBa_2Cu_3O_{7-\delta}$ thin films excited by femtosecond optical pulses," *Appl. Phys. Lett.*, **69** 1948-1950 1996

[79] E. H. Hall, "On a New Action of the Magnet on Electric Currents," *American Journal of Mathematics*, 2 287-292 1879

[80] S. Furtner, R. Semerad, G. Sigl and W. Prusseit, "Reel-to-reel critical current measurement of coated conductors," *Supercond. Sci. Technol.*, **17** S281-S284 2004.

[81] Kouhei Higashikawa, Kazutaka Imamura, Kei Shiohara, Masayoshi Inoue, Takanobu Kiss, Yashiro Iijima, Takashi Saito, Masasteru Yoshizumi and Teruo Izumi, "Speed-up of Scanning Hall-probe Microscopy System for Nondestructive Characterization of In-plane Distribution of Critical Current Density for Long RE-123 Coated Conductors," *Abstracts of CSJ conference*, **84** 36 2011.

[82] B. D. Josephson, "The discovery of tunneling supercurrents," *Reviews of Modern Phys.*, 46 251-254 1974.

[83] K. Koyanagi, T. Kiss, M. Inoue, T. Nakamura, K. Iwakuma, M. Takeo and Y. Shiohara, "Measurement of local current flow around transverse defects in YBCO film by use of scanning SQUID microscope," *PhysicaC*, **445-448** 677-681 2006

[84] C. P. Bean, "MAGNETIZATION OF HARD SUPERCONDUCTORS," **8** 250-253 1962

[85] E. H. Brandt and M. Indenbom, "Type-II-superconductor strip with current in a perpendicular magnetic field", *Phys. Rev. B*, **48** 12893 1993.

[86] T. H. Johansen, M. Baziljevich, H. Bratsberg, Y. Galperin, P.E. Lindelof, Y. Shen and P. Vase, "Direct observation of the current distribution in thin superconducting strips using magneto-optic imaging", *Phys. Rev. B*, **54** 16264 1996.

[87] A. V. Bobyl, D. V. Shantsev, Y. M. Galperin, T. H. Johansen, M. Baziljevich and S. F. Karmanenko, "Relaxation of transport current distribution in a YBaCuO strip studied by maneto-optical imaging", *Supercond. Sci. Technol.*, **15** 82-89 2002.

[88] J. Yoo, J. Lee, S-M Lee, Y-H Jung, D. Youm and S. S. Oh, "Current redistribution of a current carrying superconducting tape in a perpendicular magnetic field", *Supercond. Sci. Technol.*, **22** 125019 2009.

[89] P. Ušák, "The measurement of current distribution in superconducting tape. Comparison of destructive and no-destructive method", *Physica C*, **384** 93-101 2003.

[90] Bradley J. Roth, Nestor G. Sepulveda and John P. Wikswo, Jr., "Using a magnetometer to image a two-dimensional current distribution," *J. Appl. Phys.*, **65** 361-372 1988.

[91] T. Kiss. M. Inoue, T. Shoyama, S. Koyanagi, D. Mitsui, T. Nakamura, K. Imamura, A. Ibi, Y. Yamada, T. Kato, T. Hirayama and Y. Shiohara, "Visualizing transport properties in IBAD based YBCO coated conductors by multiple analysis techiniques," *IEEE Trans. Applied Superconductivity*, **17** 3211-3214 2007.

[92] Masayoshi Inoue, Kenji Abiru, Yohishiro Honda, Yasuhito Iijima, Kazuomi Kakimoto, Takashi Saitoh, Koichi Nakao and Yuh Shiohara, "Observation of Current Distribution in High-$T_c$ Superconducting Tape Using Scanning Hall-Probe Microscope," *IEEE Trans. Applied Superconductivity*, 19 2847-2850 2009.

[93] P. W. Anderson and Y. B. Kim, "Hard Superconductivity: Theory of the Motion of Abrikosov Flux Lines," *Reviews of Modern Physics*, **36** 39-43 1964.

[94] Yu V Bugoslavsky, "Magnetic measurements of critical current density, pinning and flux creep," Handbook of superconducting materials, edited by David A. Cardwell and David S. Ginley, Institute of Physics, 1323-1370 2003.

[95] K. Yamafuji, T. Fujiyoshi, K. Toko and T. Matsushita, "A theory of thermally activated flux creep in nonideal type II superconductors," *PhysicaC*, **159** 743-759 1989.

[96] L. G. Rubin, D. R. Nelson and H. H. Sample, "Characterization of two commercially available Hall effect sensors for high magnetic fields and low temperatures," *Rev. Sci. Instrum.*, **46** 1624-1631 1975.

[97] M. Inoue, T. Kiss, T. Kuga, M. Ishimaru, M. Takeo, T. Matsushita, Y. Iijima, K. Kakimoto, T. Saitoh, S. Awaji, K. Watanabe and Y. Shiohara, "Estimation of *E-J* characteristics in a YBCO coated conductor at low temperature and very high magnetic field," *PhysicaC*, **392-396** 1078-1082 2003.

[98] Tychonoff, A. N., V. Y. Arsenin, "Solution of Ill-posed Problems," Washington: Winston & Sons 1977

[99] Pavol Usak, "Errors in measurement of current distribution in a superconducting tape," *Supercond. Sci. Technol.*, **24** 045007 2011.

[100] John R. Clem, J. H. Claassen, and Yasunori Mawatari, "AC losses in a finite *Z* stack using an anisotropic homogeneous-medium approximation", *Supercond. Sci. Technol.*, **20** 1130-1130 2007.

[101] Michinaka Sugano, Shutaro Machiya, Masugu Sato, Tomoyuki Koganezawa, Koji Shikimachi, Naoki Hirano, and Shigeo Nagaya, " Bending strain analysis considering a shift of the neutral axis for YBCO coated conductors with and without a Cu stabilizing layer", *Supercond. Sci. Technol.*, **24** 075019 2011.

# Records of AM

**1. List of publication**

**Journal Papers**

Articles related to this thesis are 1.3 and 1.4.

1.1 A. Miyazoe, H. Abe, T. Ando, N. Hirota, M. Sekino and H. Wada,
"A New Approach to $MgB_2$ Superconducting Magnet Fabrication",
*J. Phys. Conference series*, Vol. 97, 012272, pp1-6, (200

1.2 M. Sugano, S. Choi, A. Miyazoe, T. Ando, K. Itoh, T. Kiyoshi, H. Wada and V. Selvamanickam,
"Strain analysis of $I_c$ ($\varepsilon$) characteristic of YBCO coated conductor measured by an Walters spring",
*IEEE Trans. Appl. Supercond.*, Vol. 18, No. 2, pp1143-1146, June (200

1.3 A. Miyazoe, M. Sekino, T. Kiyoshi, H. Ohsaki,
"Magnetic field induced by screening current in short and straight coated conductors",
*IEEE Trans. Appl. Supercond.*, Vol. 20, Issue 3, pp. 1557-1560, 2010

1.4 T. Ando, A. Miyazoe, N. Hirota, K. Tatamidani, H. Wada, S. Tsukamoto, O. Ozaki and T. Kiyoshi,
"Direct production of $Nb_3Al$ superconducting coil by electron beam irradiation on a cold-sprayed cylinder",
*Surf. Coat. Technol.*, Vol. 205, Issue 7, pp. 1990-1994, December 2010

1.5 A. Miyazoe, M. Sekino, T. Kiyohsi and H. Ohsaki,
"Current Distribution in Coated Conductor Under External Magnetic field up to 5 T",
*IEEE Trans. Appl. Supercond.*, Vol. 21, No. 3, pp. 1600-1603, 2011.

1.6 M. Sekino, H. Yasuda, A. Miyazoe and H. Ohsaki,
"Concentric Slitting of a Ring-Shaped Bulk Superconductor for a Reduction in Circumferential Inhomogeneity of the Trapped Magnetic Field",
*IEEE Trans. Appl. Supercond.*, in Press

1.7 M. Sekino, A. Miyazoe, H. Ohsaki, T. Hisatsune, O. Ozaki, T. Kiyoshi, H. Wada,
"MRI Using a Superconducting Magnet with an Off-Centered Homogeneous Field Zone",
*Journal of Applied Physics*, in press.

**2. Conference Presentations**

**International conference**

Presentation related to this thesis are 2.5, 2.5, 2.8, and 2.9.

2.1 A. Miyazoe, H. Abe, T. Ando, N. Hirota, M. Sekino and H. Wada,
"A New Approach to $MgB_2$ Superconducting Magnet Fabrication",
8th European Conference on Applied Superconductivity, Brussels, Belgium, September 2007

2.2 T. Ando, K. Tatamidani, A. Miyazoe, N. Hirota, H. Wada, S. Tsukamoto, O. Ozaki,
"A novel approach to $Nb_3Al$ superconducting magnet fabrication",
International Conference on Magneto-Science 2007, Hiroshima, Japan, Nov. 11-15, 2007, Proceedings of ICMS 2007, p.76.

2.3 A. Miyazoe, H. Abe, T. Ando, N. Hirota, M. Sekino and H. Wada,
"A New Approach to $MgB_2$ Superconducting Magnet Fabrication",
3rd International Workshop on Materials Analysis and Processing in Magnetic Fields, Tokyo, Japan, May 2008.

2.4 A. Miyazoe, H. Abe, K. Kurashima, K. Aoyagi, T. Kimura, Y. Sugimoto, K. Nakajima, T. Ando, N. Hirota, H. Ohsaki and H. Wada,
"Electrochemical synthesis of highly crystalline $MgB_2$ nanowires",
Material research society spring meeting, San Francisco, United Sates of America, April 2009.

2.5 A. Miyazoe, M. Sekino, T. Kiyoshi and H. Ohsaki,
"Magnetic field induced by screening current in short and straight coated conductors",
21st International Conference on Magnet Technology, Hefei, China, October 2009.

2.6 A. Miyazoe, M. Sekino, T. Kiyoshi and H. Ohsaki,
"Magnetic fields generated by screening currents on coated conductors in external field and/or self field",
Asian conference 2009 on Applied Superconductivity and Cryogenics, Matsue, Japan, December 2009.

2.7 H. Ohsaki, Z. Lv, A. Miyazoe and M. Sekino,
"Design study of High-Temperature Superconducting Coils for Maglev Vehicles",
Asia Pacific Symposium of Applied Electromagnetics and Mechanics, Kuala Lumpur, Malaysia, July 2010.

2.8 A. Miyazoe, M. Sekino, T. Kiyoshi and H. Ohsaki,
"Distributions of Transport and Screening currents flowing in coated conductor",
Applied Superconductivity Conference 2010, 3LP3C: 255, Washington D.C., USA, August 2010.

2.9 A. Miyazoe, M. Sekino, T. Kiyoshi and H. Ohsaki,
"Magnetic field distribution generated by screening current flowing in coated conductor", 22nd International Conference on Magnet Technology, Marseille, France, September 2011.

**International symposium**

A presentation related to this thesis is 2.12.

2.10 A. Miyazoe, H. Abe, K. Kurashima, K. Aoyagi, T. Kimura, Y. Sugimoto, K. Nakajima, T. Ando, N. Hirota, H. Ohsaki and H. Wada,
"A New Approach to $MgB_2$ Superconducting Magnet Fabrication",
The 9th Seoul National University – University of Tokyo Joint seminar on Electrical engineering, Tokyo, Japan, January 2009.

2.11 A. Miyazoe, M. Sekino, H. Ohsaki, T. Ando, H. Abe, K. Kurashima, T. Aoyagi, T. Kimura, Y. Sugimoto, K. Nakajima, N. Hirota, T. Kiyoshi and H. Wada, "Construction of superconducting coils consisting of superconducting films", European summer school on superconductivity, Lans en Vercors, France, June 2009.

2.12 A. Miyazoe, M. Sekino, T. Kiyoshi and H. Ohsaki, "Magnetic fields induced by screening currents flowing on superconducting coated conductors", The 10th University of Tokyo – Seoul National University Joint Seminar on Electrical Engineering, Seoul, Korea, March 2010.

**Domestic conference**

Presentations related to this thesis are 2.17, 2.28, 2.20, 2.21, 2.22, 2.23, and 2.25.

2.13 宮副　照久, 阿部　英樹, 安藤　努, 廣田　憲之, 木吉　司, 和田　仁,
"新しい超伝導マグネット作製技術の開発 －$MgB_2$ へ適用－",
第 77 回　2007 年度秋季　低温工学・超電導学会, 仙台, 2007 年 11 月

2.14 安藤 努, 畳谷　和晃, 宮副照久, 廣田憲之, 和田 仁, 塚本 進, 尾崎 修, 木吉 司,
"新しい超伝導マグネット作製技術の開発 －$Nb_3Al$ への適用－",
第 77 回　2007 年度秋季　低温工学・超電導学会, 仙台, 2007 年 11 月

2.15 安藤 努, 畳谷和晃, 宮副照久, 廣田憲之, 和田 仁, 塚本 進, 尾崎 修, 木吉 司,
"新しい超伝導マグネット作製技術の開発 －$Nb_3Al$ への適用－",
2008 年 3 月 27 日-30 日, 日本大学理工学部 船橋キャンパス, 第 55 回応用物理学関係連合講演会講演予稿集 No. 1, p.305.

2.16 和田　仁, 宮副　照久, 安藤　努, 宮松　和浩, 黒田　恒生, 伊藤　喜久男, 菅野　未知央,
"超伝導特性に及ぼす応力・歪効果ー曲げ試験による評価—",
2008 年度春季　低温工学・超電導学会, 明星大学, 2008 年 5 月 26 日-28 日

2.17 宮副　照久, 関野　正樹, 大崎　博之, 木吉　司,
"バックグラウンド磁場を変動させたときの短尺 Y 系テープ線材における捕捉磁界と遮蔽効果",
第 80 回 2009 年度春季　低温工学・超電導学会, 2009 年 5 月, 早稲田大学

2.18 宮副 照久, 関野 正樹, 大崎 博之, 木吉 司,
"イットリウム系超電導テープ線材の磁化電流がもたらす磁界の評価",
2009 年 9 月 8 日-11 日, 富山大学　五福キャンパス, 第 70 回応用物理学会学術講演会

2.19 宮副 照久, 阿部 英樹, 倉嶋 敬次, 青柳 岳史, 木村 隆, 杉本 喜正, 中島 清美, 安藤 努, 廣田 憲之, 大崎 博之, 和田 仁,
"高結晶性 $MgB_2$ ナノワイヤの電気化学的合成",
2009 年 9 月 8 日-11 日, 富山大学　五福キャンパス, 第 70 回応用物理学会学術講演会

2.20 宮副 照久, 関野 正樹, 大崎 博之, 木吉 司,
“配列されたイットリウム系線材の遮蔽特性評価”,
2010 年 3 月 17 日-20 日, 東海大学　湘南キャンパス, 第 57 回応用物理学関係連合講演会
2.21 宮副　照久, 関野　正樹, 大崎　博之, 木吉　司,
“イットリウム系線材の遮蔽磁界分布”,
第 82 回　2010 年度春季　低温工学・超電導学会, 川崎市産業振興会館, 2010 年 5 月 12-14 日
2.22 宮副　照久, 関野　正樹, 大崎　博之, 木吉　司,
“短尺イットリウム系超電導線材における磁場中での電流分布の評価”,
電気学会研究会　金属・セラミックス研究会　MC-10-12, 2010 年 10 月 31 日
2.23 宮副　照久, 関野　正樹, 大崎　博之, 木吉　司,
“イットリウム系超電導線材中の通電時電流分布の外部磁場印加による変化”,
第 83 回　2010 年度秋季　低温工学・超電導学会, かごしま県民交流センター, 2010 年 12 月 1-3 日
2.24 13. 呂　臻, 宮副　照久, 関野　正樹, 大崎　博之,
“磁気浮上鉄道用高温超電導コイルの基本設計”,
第 83 回　2010 年度秋季　低温工学・超電導学会, かごしま県民交流センター, 2010 年 12 月 1-3 日
2.25 宮副　照久, 中西　泰章, 関野　正樹, 大崎　博之, 木吉　司,
“複数のイットリウム系超電導線材内に発生する遮蔽電流が生み出す磁場分布とその時間変化”,
第 84 回 2011 年度春季　低温工学・超電導学会, 物質・材料研究機構, 2011 年 5 月 18-20 日

**3. Patent**

宮副　照久、阿部　英樹、安藤　努、廣田　憲之、和田　仁
発明等の名称：超電導素子
特許番号：特開 2010-245430
発明の技術分野：導電性材用と超電導材料と絶縁材料とによって構成される導電素子に関する。
発明内容の概要：絶縁材料の中にホウ化マグネシウム($MgB_2$ ナノ細線が埋め込まれており、$MgB_2$ ナノ細線が導電性金属と電気的に接合している超電導素子の開発。

**4. Award**

4.1　平成 22 年度 GCOE 優秀論文発表賞
4.2　平成 22 年電気学会　優秀論文発表賞（基礎・材料・共通部門表彰）論文
「短尺イットリウム系超電導線材における磁場中での電流分布の評価」

**5. Grants**

2009/04-2010/03: 財団法人　双葉電子記念財団奨学生